# Evolution, nucleosynthesis and yields of low mass AGB stars at different metallicities (II): the FRUITY database.

S. Cristallo[1,2]
1 - Departamento de Física Teórica y del Cosmos, Universidad de Granada, 18071 Granada, Spain
2 - INAF-Osservatorio Astronomico di Collurania, 64100 Teramo, Italy

and

L. Piersanti[2]
2 - INAF-Osservatorio Astronomico di Collurania, 64100 Teramo, Italy

and

O. Straniero[2]
2 - INAF-Osservatorio Astronomico di Collurania, 64100 Teramo, Italy

and

R. Gallino[3,2]
3 - Dipartimento di Fisica Generale, Università di Torino, 10125 Torino, Italy
2 - INAF-Osservatorio Astronomico di Collurania, 64100 Teramo, Italy

and

I. Domínguez[1]
1 - Departamento de Física Teórica y del Cosmos, Universidad de Granada, 18071 Granada, Spain

and

C. Abia[1]
1 - Departamento de Física Teórica y del Cosmos, Universidad de Granada, 18071 Granada, Spain

and

G. Di Rico[2]
2 - INAF-Osservatorio Astronomico di Collurania, 64100 Teramo, Italy

and

M. Quintini[2]
2 - INAF-Osservatorio Astronomico di Collurania, 64100 Teramo, Italy

and

S. Bisterzo[3]
3 - Dipartimento di Fisica Generale, Università di Torino, 10125 Torino, Italy

Received / Accepted

Received _____; accepted _____

## ABSTRACT

By using updated stellar low mass stars models, we can systematically investigate the nucleosynthesis processes occurring in AGB stars, when these objects experience recurrent thermal pulses and third dredge-up episodes. In this paper we present the database dedicated to the nucleosynthesis of AGB stars: the FRUITY (FRANEC Repository of Updated Isotopic Tables & Yields) database. An interactive web-based interface allows users to freely download the full (from H to Bi) isotopic composition, as it changes after each third dredge-up episode and the stellar yields the models produce. A first set of AGB models, having masses in the range $1.5 \leq M/M_{\odot} \leq 3.0$ and metallicities $1 \times 10^{-3} \leq Z \leq 2 \times 10^{-2}$, is discussed here. For each model, a detailed description of the physical and the chemical evolution is provided. In particular, we illustrate the details of the *s*-process and we evaluate the theoretical uncertainties due to the parametrization adopted to model convection and mass loss. The resulting nucleosynthesis scenario is checked by comparing the theoretical [hs/ls] and [Pb/hs] ratios to those obtained from the available abundance analysis of *s*-enhanced stars. On the average, the variation with the metallicity of these spectroscopic indexes is well reproduced by theoretical models, although the predicted spread at a given metallicity is substantially smaller than the observed one. Possible explanations for such a difference are briefly discussed. An independent check of the third dredge-up efficiency is provided by the C-stars luminosity function. Consequently, theoretical C-stars luminosity functions for the Galactic disk and the Magellanic Clouds have been derived. We generally find a good agreement with observations.

*Subject headings:* stars: AGB and post-AGB — physical data and processes: nuclear

reactions, nucleosynthesis, abundances

## 1. Introduction

Asymptotic Giant Branch (AGB) stars are among the most efficient polluters of the Interstellar Medium (ISM). Due to the simultaneous action of internal nucleosynthesis (p, $\alpha$ and n captures), convective mixing and a strong stellar wind, these stars provide a substantial contribution to the chemical evolution of the Universe. Light (e.g. He, Li, F, C, N, Ne, Na, Mg) and heavy (from Sr to Pb) elements can be produced. In particular, the activation of neutron sources in their He-rich zone makes AGB stars a special site for the stellar nucleosynthesis. The main neutron source is the $^{13}$C($\alpha$,n)$^{16}$O, which is particularly important in low mass AGB stars ($M < 3M_{\odot}$) (Straniero et al. 1995; Gallino et al. 1998; for a review, see Herwig 2005 and Straniero et al. 2006). During the Thermally Pulsing AGB phase (TP-AGB), a recurrent penetration of the convective envelope in the H-exhausted core (Third Dredge-Up, hereinafter TDU), brings a few protons in a region where the chemical pattern is dominated by helium (80%) and carbon (20%). Then, when the temperature rises in this region, a $^{13}$C pocket forms where the $^{13}$C($\alpha$,n)$^{16}$O reaction takes place. Such a $^{13}$C burning gives rise to the so-called main component of the *s*-process nucleosynthesis. It occurs in radiative conditions on a relatively large timescale (some $10^4$ yr), and produces a rather low neutron density ($10^6$–$10^7$ neutrons/cm$^3$). A second neutron source may be activated within the convective zone generated by a Thermal Pulse (TP), the $^{22}$Ne($\alpha$,n)$^{25}$Mg (Cameron 1960; Truran & Iben 1977; Cosner et al. 1980; Iben & Renzini 1983). In this case, the timescale of the neutron capture nucleosynthesis is definitely shorter (some yr) and the average neutron density is higher ($10^9$–$10^{11}$ neutrons/cm$^3$). This second neutron burst is only marginally activated in low mass stars of solar-like metallicity, while it is expected to be more efficient in more massive AGB stars and at the low metallicities typically found in the Galactic halo or in dwarf spheroidal galaxies (Straniero et al. 2000; Karakas & Lattanzio 2006; Cristallo et al. 2009).

From Lambert et al. (1995), the theoretical scenario here recalled has been largely confirmed by the abundance analysis of AGB stars undergoing TDUs. Theoretical stellar models are essential to interpret the continuously growing number of spectroscopic data collected with the latest generation of modern telescopes, from very metal-poor C-rich stars (see Bisterzo et al. 2010 and references therein) to the Galactic and extragalactic C (N-type) stars (Abia et al. 2001, 2002, 2008, 2010; de Laverny et al. 2006; Zamora et al. 2009), Ba-stars (Allen & Barbuy 2006; Smiljanic et al. 2007; Liu et al. 2009), post-AGB stars (van Winckel & Reyniers 2000; Reddy et al. 2002; Reyniers et al. 2004), planetary nebulae (Sharpee et al. 2007; Sterling & Dinerstein 2008) and born-again AGB stars (PG 1159 stars) (Werner & Herwig 2006; Werner et al. 2009). Similarly, the growing number of measured isotopic ratios in pre-solar SiC grains (Hoppe et al. 1997; Lugaro et al. 1999; Zinner et al. 2006; Barzyk et al. 2007; Davis et al. 2009) require specific calculations to interpret them. Nucleosynthesis predictions are also needed to built up chemical evolution models (see e.g. Travaglio et al. 1999; Romano et al. 2010; Kobayashi et al. 2010). All these studies require updated theoretical predictions of the nucleosynthesis occurring in AGB stars belonging to very different stellar populations, with different masses and initial compositions. For these reasons, we decided to create a complete and homogeneous database of AGB nucleosynthesis predictions and yields.

During the last 20 years, our working group has produced several improvements in the physical description of AGB stellar interiors and has developed the numerical algorithms needed to follow the complex interplay between nuclear burning, convection and mass loss. All these efforts converged in a recent paper (Cristallo et al. 2009, hereafter Paper I), where stellar models calculations of 2 $M_{\odot}$ AGB stars of various metallicities were presented. These calculations were based on a full nuclear network, from H to Bi, including 700 isotopes and about 1000 nuclear processes among strong and weak interactions. In this paper, we present the FRUITY database (FRANEC Repository of Updated Isotopic

Tables & Yields), which is available on the web pages of the Teramo Observatory (INAF)[1]. This database has been organized under a relational model through the MySQL Database Management System. This software links input data to logical indexes, optimizing their arrangement and speeding up the response time to the user query. Its web interface has been developed through a set of Perl[2] scripts, which allow to submit the query strings resulting from filling out appropriate fields to the managing system. It contains our predictions for the surface composition of AGB stars undergoing TDU episodes and the stellar yields they produce. Tables for AGB models having initial masses $1.5 \leq M/M_{\odot} \leq 3.0$ and $1 \times 10^{-3} \leq Z \leq 2 \times 10^{-2}$ are available. FRUITY will be expanded soon by including AGB models with larger initial mass and/or lower $Z$.

In Sections 2 and 3 of the present paper we describe the stellar models and the related nucleosynthesis results. In Section 4 we address the main uncertainties affecting our models while comparisons with available photometric and spectroscopic data are discussed in Section 6. Conclusions are drawn in Section 7.

## 2. The FRANEC code

The stellar models of the FRUITY database have been obtained by means of the FRANEC code (Frascati RAphson-Newton Evolutionary Code - Chieffi et al. 1998). The most important upgrades needed to follow the AGB evolution and nucleosynthesis have been extensively illustrated in Straniero et al. (2006), Cristallo et al. (2007) and in Paper I.

We have computed 28 evolutionary models, for different combination of masses (1.5,

[1]http://www.oa-teramo.inaf.it/fruity

[2]Perl is a general-purpose, object-oriented programming language.

2.0, 2.5 and 3.0 $M_{\odot}$) and metallicities ($Z = 1.0 \times 10^{-3}$ with $Y$=0.245; $Z = 3.0 \times 10^{-3}$ and $Z = 6.0 \times 10^{-3}$ with $Y$=0.260; $Z = 8.0 \times 10^{-3}$ and $Z = 1.0 \times 10^{-2}$ with $Y$=0.265; $Z = 1.4 \times 10^{-2} \equiv Z_{\odot}$ and $Z = 2.0 \times 10^{-2}$ with $Y$=0.269). In the present paper only scaled solar compositions are considered, whose relative distribution has been derived according to the solar compilation by Lodders (2003).

In addition to the commonly adopted opacity tables calculated for a scaled solar composition, we use C-enhanced opacity tables, as described in Cristallo et al. (2007), to take into account the effects of TDU episodes. The most relevant atomic and molecular species have been considered. This improved radiative opacity substantially affects the stellar radius and the mass loss rate. This in turn, shortens the AGB lifetime hence reducing the amount of material returned to the ISM (see also Marigo 2002; Weiss & Ferguson 2009; Ventura & Marigo 2009). Our code interpolates between opacity tables whose C-enhancements ($f_i$) depend on the metallicity (Cristallo et al. 2007; Lederer & Aringer 2009). The $f_i$ parameter is defined as the ratio between the $^{12}$C mass fraction and the corresponding solar value scaled to the initial $Z$ [3]. Higher values of $f_i$ are needed to follow the evolution of low $Z$ models up to the AGB tip, due to the lower initial carbon mass fraction and the more efficient third dredge-up.

Our computations start from a proto-star, namely a model in hydrostatic equilibrium, chemically homogeneous, fully convective and cooler than the threshold for any nuclear burning. We follow the evolution from the pre-main sequence up to the end of the AGB phase, passing through the core He-flash. No core overshoot has been adopted during core H-burning. Semi-convection was applied during core He-burning (see also Section 5). We stop the computations when, as a consequence of the mass loss, the H-rich envelope has

[3]Note that $f_i = 1.8$ corresponds to C/O$\sim$1

been reduced to the minimum mass for the occurrence of the TDU[4] (see Straniero et al. 2003a). In Table 2 we summarize the main properties of the evolutionary sequences prior to the thermally pulsing AGB phase. For each metallicity and initial He content we report from left to right: the initial mass (solar units), the core H-burning lifetime (in Myr), the maximum size of the convective core developed during the main sequence (in solar units), the He surface mass fraction after the occurrence of the First Dredge-Up (FDU), the luminosity at the RGB tip (logarithm of $L$ in solar unit), the mass of the H-exhausted core at the beginning of core-He burning ($M^1_{\rm He}$, in solar units), the core He-burning lifetime (in Myr), the mass of the H-exhausted core at the end of core He-burning ($M^2_{\rm He}$, in solar units) and at the first TP ($M^3_{\rm He}$, in solar units)[5]. When comparing these models with those already published in Domínguez et al. (1999) (which where obtained with an older release of the FRANEC code) variations typically lower than 10% are found. These variations are due to the many upgrades of the input physics and to the differences in the initial composition (mainly the He content). For a more complete description of the pre-AGB evolution and the relevant theoretical uncertainties, the reader may refer to Domínguez et al. (1999).

### 2.1. The Thermally Pulsing AGB phase

In Tables 3, 4, 5 we report quantities characterizing the evolutionary sequences during TP-AGB phase for three key metallicities: $Z$=0.02, $Z$=0.006 and $Z$=0.001 [6]. For each

[4]The minimum envelope mass for TDU occurrence is $M_{\rm ENV} \sim (0.4 \div 0.5) M_\odot$ at large metallicities and $M_{\rm ENV} \sim (0.3 \div 0.4) M_\odot$ at low metallicities.

[5]We define the first TP when the luminosity generated by $3\alpha$ reactions exceeds $10^6 L_\odot$ for the first time.

[6]A pdf file with Tables corresponding to all the computed metallicities is available on the web page of the database. Note that some of the models with $M = 2M_\odot$ have already been

model, we report (left to right): the progressive TP number ($n_{\rm TP}$)[7], the total mass ($M_{\rm Tot}$), the mass of the H-exhausted core ($M_{\rm H}$)[8], the mass of the H-depleted material dredged-up by the TDU episode which follows a TP($\Delta M_{\rm TDU}$), the maximum mass of the convective zone generated by the TP ($\Delta M_{\rm CZ}$), the growth of the H-exhausted core during the interpulse period preceding the current TP($\Delta M_{\rm H}$), the overlap factor $r$[9], the $\lambda$ factor[10], the duration of the interpulse period preceding the current TP ($\Delta t_{ip}$), the maximum temperature attained at the bottom of the convective zone generated by the TP ($T_{\rm MAX}$), the surface metallicity attained after the TDU ($Z_{surf}$), the corresponding C/O ratio and the average number of neutrons captured per initial iron seed nucleus during the radiative $^{13}$C pocket burning ($n_c$). Lastly, we report the total mass of the material cumulatively dredged-up ($M^{\rm tot}_{\rm TDU}$) and the duration of the C-rich phase of the model ($\tau_C$)[11] for each model.

The main properties of the TP-AGB phase of 2 $M_\odot$ stars as a function of the metallicity have been extensively presented in Paper I. In this paper we explore in greater detail the evolution of low mass stars by discussing how the physical conditions favoring the AGB nucleosynthesis scenario change as a function of the initial mass. One of the most important quantities driving the nucleosynthesis in low mass AGB stars is the amount of $^{13}$C available in the pockets, which form in the transition layer between the H-rich envelope and the H-depleted core after each TDU. In our models, the formation of the $^{13}$C-pocket is a

---

presented in Paper I but, for a better understanding, have also been reported in this paper.

[7]Negative numbers correspond to TPs not followed by TDU.

[8]At the onset of the thermal pulse.

[9]Namely, the overlap, in mass, between the convective zones generated by the present and the previous TP.

[10]Namely, the ratio between $\Delta M_{\rm TDU}$ and $\Delta M_{\rm H}$.

[11]That is the time spent of the AGB with a surface C/O>1.

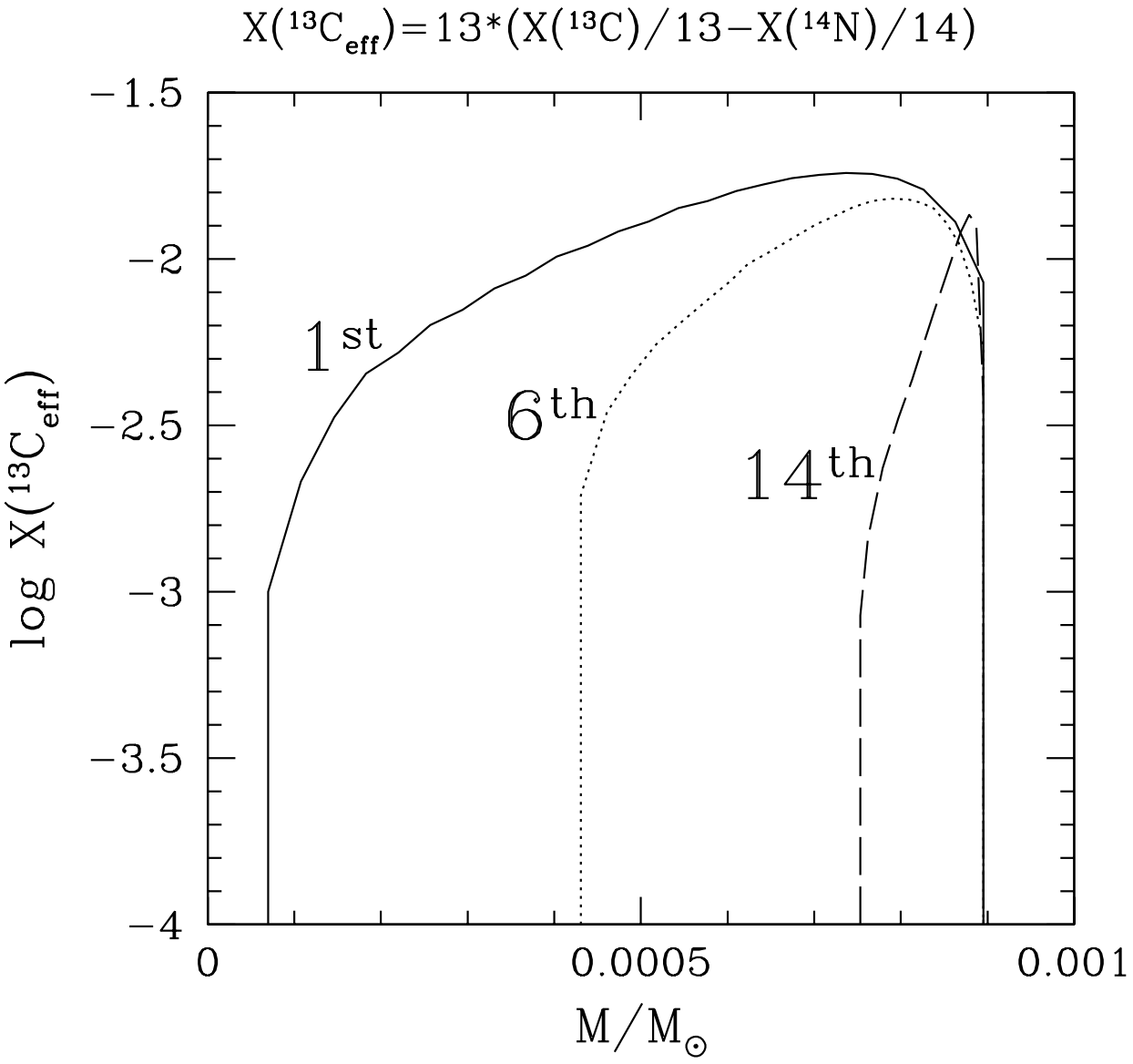


Fig. 1.— Mass extension of the *effective* $^{13}$C in the $1^{st}$, $6^{th}$ and $14^{th}$ (last) pocket of the 2 $M_{\odot}$ model with $Z = 6 \times 10^{-3}$. The pockets have been shifted in mass in order to superimpose their external borders. The 0 point of the abscissa is arbitrary.

by-product of the introduction of an exponentially decaying profile of convective velocities at the base of the envelope (see Formula 1 in Paper I). This has been done in order to stabilize this convective boundary during TDU episodes (see Paper I). Such a discontinuity originates from the opacity difference between the H-rich envelope and the He-rich intershell (i.e. the region between the He-shell and the H-shell, hereafter He-intershell). Even if this additional mixing always works during the TP-AGB phase, the deriving opacity-induced extra-mixed zone is appreciable only during TDU episodes (and thus negligible during the interpulse phases). At the beginning of the interpulse, the few protons in this transition layer are captured by $^{12}$C nuclei, producing $^{13}$C (via the $^{12}$C(p,$\gamma$)$^{13}$N($\beta^+\nu$)$^{13}$C nuclear chain). A further proton capture may eventually lead to the production of $^{14}$N. Consequently, after each TDU episode, a $^{13}$C pocket forms, partially overlapped to a $^{14}$N pocket. Note that where the abundance of $^{22}$Ne is comparable to the $^{12}$C abundance, a third small $^{23}$Na pocket forms (see Figure 13 of Paper I). Due to the resonant $^{14}$N(n,p)$^{14}$C neutron capture cross section, $^{14}$N is a very efficient neutron poison. However, the released protons give rise to a partial neutrons recycling through the following chain: $^{12}$C(p,$\gamma$)$^{13}$N($\beta^+$)$^{13}$C($\alpha$,n)$^{16}$O. Since our models are calculated with a full nuclear network, the combined effect of poisons and neutron recycling on the on-going *s*-process nucleosynthesis is properly taken into account. To illustrate the properties of our $^{13}$C pockets that follow, in the following we use the *effective* $^{13}$C fraction (*i.e.* the difference between the number fractions of $^{13}$C and $^{14}$N in the pocket), rather than the bare $^{13}$C amount (see the Formula in Fig. 1). Note that such a quantity is related to the total number of neutrons available for the subsequent *s*-process nucleosynthesis, which takes place when the temperature in the pocket becomes high enough for the activation of the $^{13}$C($\alpha$,n)$^{16}$O reaction. As already outlined in Paper I, the pockets shrink in mass ascending the AGB, following the compression of the whole He-intershell region. As a typical example, in Fig. 1 we plot the *effective* $^{13}$C characterizing the $1^{st}$, $6^{th}$ and $14^{th}$ (last) pocket of the 2 $M_\odot$ model with $Z = 6 \times 10^{-3}$. The pockets

have been shifted in mass in order to superimpose their external borders; the 0 point of the abscissa is arbitrary. The extension of the pockets decreases with the TDU number, the first being the largest one ($\Delta M \sim 9\times10^{-4}$ $M_{\odot}$, about 6 times greater than the last one).

In Fig. 2 we illustrate the variation of the total mass of *effective* $^{13}$C in each pocket[12] as a function of the core mass along the evolutionary sequences corresponding to the various initial masses. We concentrate on the selected metallicities of Table 2, 3 and 4 ($Z = 2 \times 10^{-2}$, $Z = 6 \times 10^{-3}$ and $Z = 1 \times 10^{-3}$, respectively). Each point corresponds to a single $^{13}$C pocket and, in turn, to a single *s*-process nucleosynthesis episode. In this context, the relative contribution of a single *s*-process episode to the overall *s*-process nucleosynthesis is proportional to the quantity reported on the *y*-axis of this plot. As extensively discussed in Paper I, the first few pockets dominate (qualitatively and quantitatively) the overall nucleosynthesis of the elements during an AGB evolutionary sequence. In practice, the composition in the He-intershell is freezed after just 4 or 5 thermal pulses followed by TDU episodes, being only marginally modified by the late $^{13}$C burnings. In Paper I we outlined that, in the 2 $M_{\odot}$ models, the first $^{13}$C pocket is only marginally consumed before the onset of the following TP and thus some $^{13}$C is engulfed in the convective shell. We confirm this finding also for the other masses. This phenomenon is particularly strong at large metallicities ($Z \geq 1 \times 10^{-2}$), where up to 80% of $^{13}$C in the first pocket burns convectively. Moreover, for the more massive and metal-rich models, a non negligible $^{13}$C percentage (<30%) in the pocket formed after the 2$^{\rm nd}$ TDU is also ingested in the TP. Lowering the metallicity, the amount of ingested $^{13}$C progressively decreases, being completely burnt in radiative conditions at $Z = 1 \times 10^{-3}$. The convective $^{13}$C burning has only minor consequences on the chemical evolution of the models (see Section 3). Note that even for the first two pockets a non negligible amount of $^{13}$C (at least 20%) burns radiatively during the

[12]That is the $^{13}$C mass integrated over the pocket region.

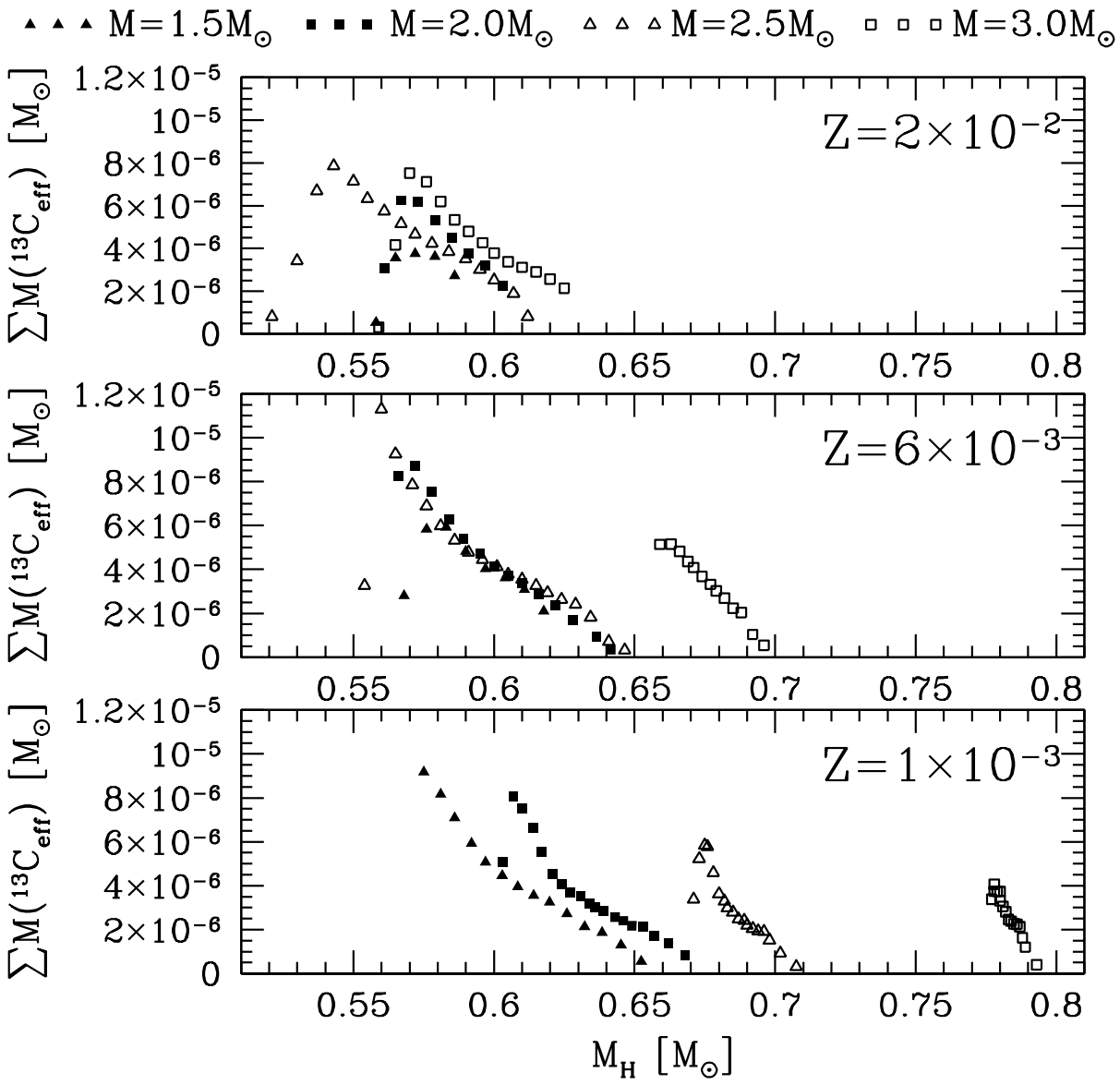


Fig. 2.— The mass of *effective* $^{13}$C in the pockets formed after each TDU episode, $\Sigma M(^{13}\mathrm{C_{eff}})$, versus the core mass. Symbols correspond to different initial stellar masses, as labelled in the figure. The top panel refers to models with $Z = 0.02$, the middle panel with $Z = 0.006$ and the lower panel with $Z = 0.001$.

interpulse phase (the exact value depending on the mass and the metallicity). Since the first two pockets are the largest ones, they provide an important contribution to the *s*-process nucleosynthesis even if the amount of $^{13}$C burnt in radiative conditions is reduced with respect to the following pockets. In Fig. 2 we take into account the partial ingestion of the first pockets by subtracting the engulfed $^{13}$C in the derivation of the *effective* $^{13}$C. Changing the mass and the metallicity of the model, a certain spread in the mass of the *effective* $^{13}$C is found. Nonetheless, this occurrence does not necessarily imply an equivalent spread in the final surface s-process distributions, which basically depend on the neutrons per iron seed in the pocket (see Section 3). In this connection, an interesting quantity is the average number of neutrons per seeds in each pocket, as reported in the last column of Tables 3, 4, 5. Recalling that the first few pockets dominate the overall *s*-process nucleosynthesis, we see that the neutrons captured per iron seed substantially increases by reducing the metallicity, while, for a fixed $Z$, it is almost insensitive to a change in the initial mass.

Due to the partial overlap of the convective zones generated by the recurrent TPs, the *s*-processed material accumulates within the He-intershell. This occurs for the first convective shells, in which the production of the *s*-process elements within the $^{13}$C pockets compensate the dilution over the ashes of the H-shell, which are basically *s*-process free (see Fig. 16 of Paper I)[13]. Afterwards, the dilution effect dominates and in the following TPs the heavy elements abundances in the He-intershell decrease. Fig. 3 illustrates the ratios between the amount of dredged-up material per TDU and the residual envelope mass as a function of the core mass, for the different stellar initial masses. Each point corresponds to a single TDU episode. Since the variation of the mass fraction of any isotope in the envelope as a consequence of a certain TDU episode is proportional to $\Delta M_{\rm TDU}/M_{\rm ENV}$, such

[13]Actually, this material also presents an *s*-process enrichment, due to previous TDU, but it is definitely lower than the one characterizing the He-intershell.

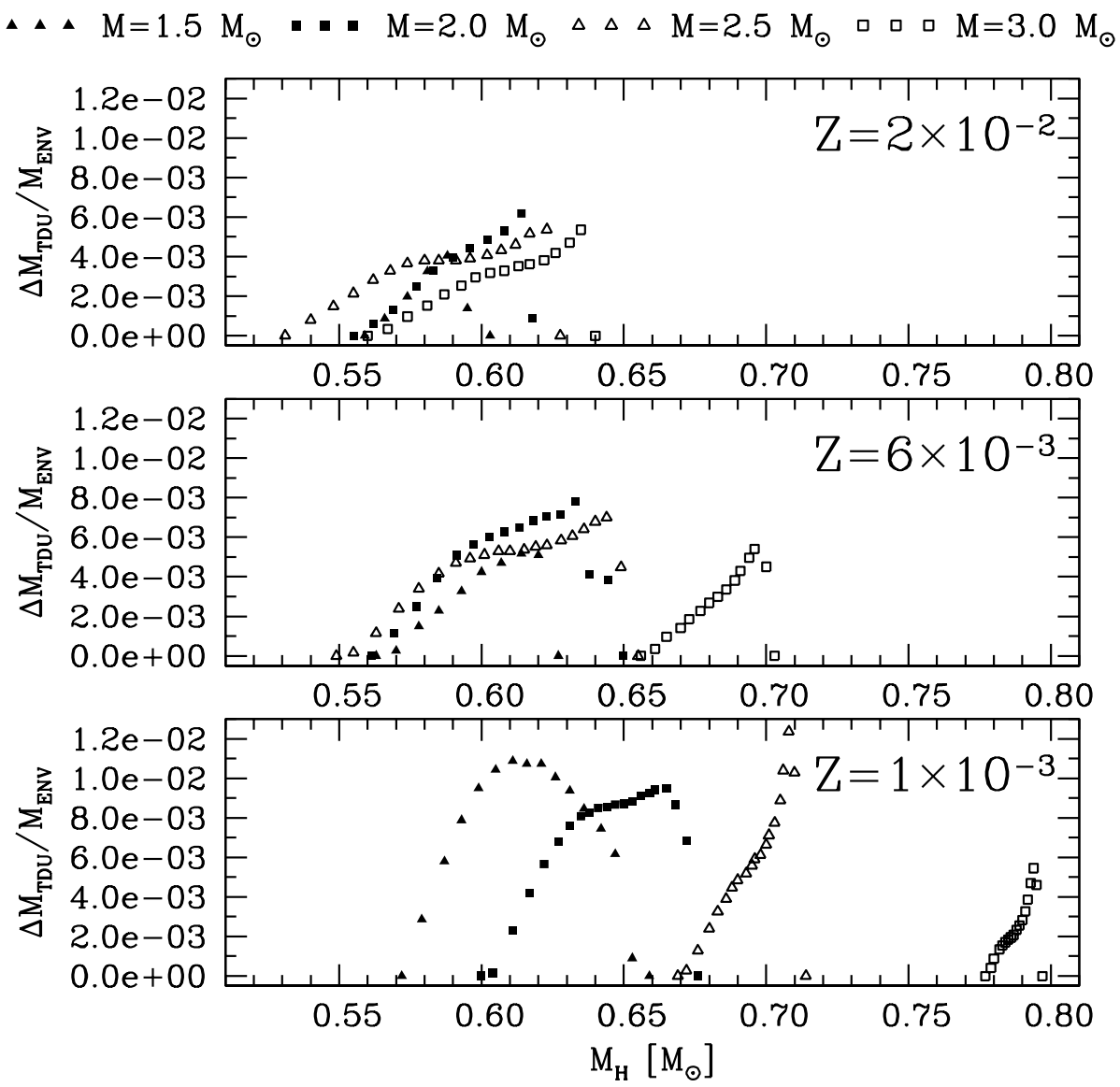


Fig. 3.— As in Fig. 2, but for the ratio between the mass of H-depleted dredged-up material and the envelope mass.

a ratio well represents the efficiency of the various TDU episodes. It generally increases during the AGB evolution, with a sharp drop to 0 when the TDU ceases. This ratio is also generally larger at low $Z$ because the TDU is deeper. Note that the 3 $M_{\odot}$ model with $Z = 0.001$ shows a substantially smaller $\Delta M_{\rm TDU}/M_{\rm ENV}$ than other masses with the same metallicity. This model develops a larger core mass and has a lower $\Delta M_{\rm TDU}$, due to the shrinking of the He-intershell. Moreover, it has a larger envelope mass. Its structure is very similar to the one characterizing Intermediate Mass Stars (IMS) with higher metallicities. The modelling of IMS is made difficult from the lack of well constrained (and direct) observational counterparts, even if new interesting data have been recently presented by Roederer et al. (2011). Moreover, the computed surface compositions of IMS strongly vary from author to author, depending on the adopted mass-loss rate, convection efficiency and opacity set (see, e.g., Ventura & Marigo 2009). Unfortunately, these quantities cannot be fixed one to the time, since they are highly degenerate.

As already mentioned in the Introduction, the activation of a second neutron burst, due to the $^{22}$Ne($\alpha$,n)$^{25}$Mg reaction, depends on the temperature attained at the base of the convective zone generated by a TP. This is illustrated in Fig. 4. For each initial mass a general trend can be seen. The maximum temperature within the convective zone generated by a TP progressively grows, reaches a maximum and then slightly decreases (during the last TPs). As discussed in Straniero et al. (2003a), this temperature trend depends on the core mass, the envelope mass and the metallicity. The maximum temperature is higher for larger core masses and larger envelope masses, while it is lower for higher $Z$. As a results, at $Z$=0.02, all stars with $M \leq 3M_{\odot}$ barely attain the threshold of the $^{22}$Ne($\alpha$,n)$^{25}$Mg reaction. On the contrary, at $Z$=0.001, in all stars with $M > 2M_{\odot}$ the second neutron burst plays a relevant role in the resulting $s$-process nucleosynthesis. As we will show in the next section, in these models there is a substantial activation of some $s$-process branchings and the corresponding increased production of branching-dependent isotopes (such as $^{60}$Fe,

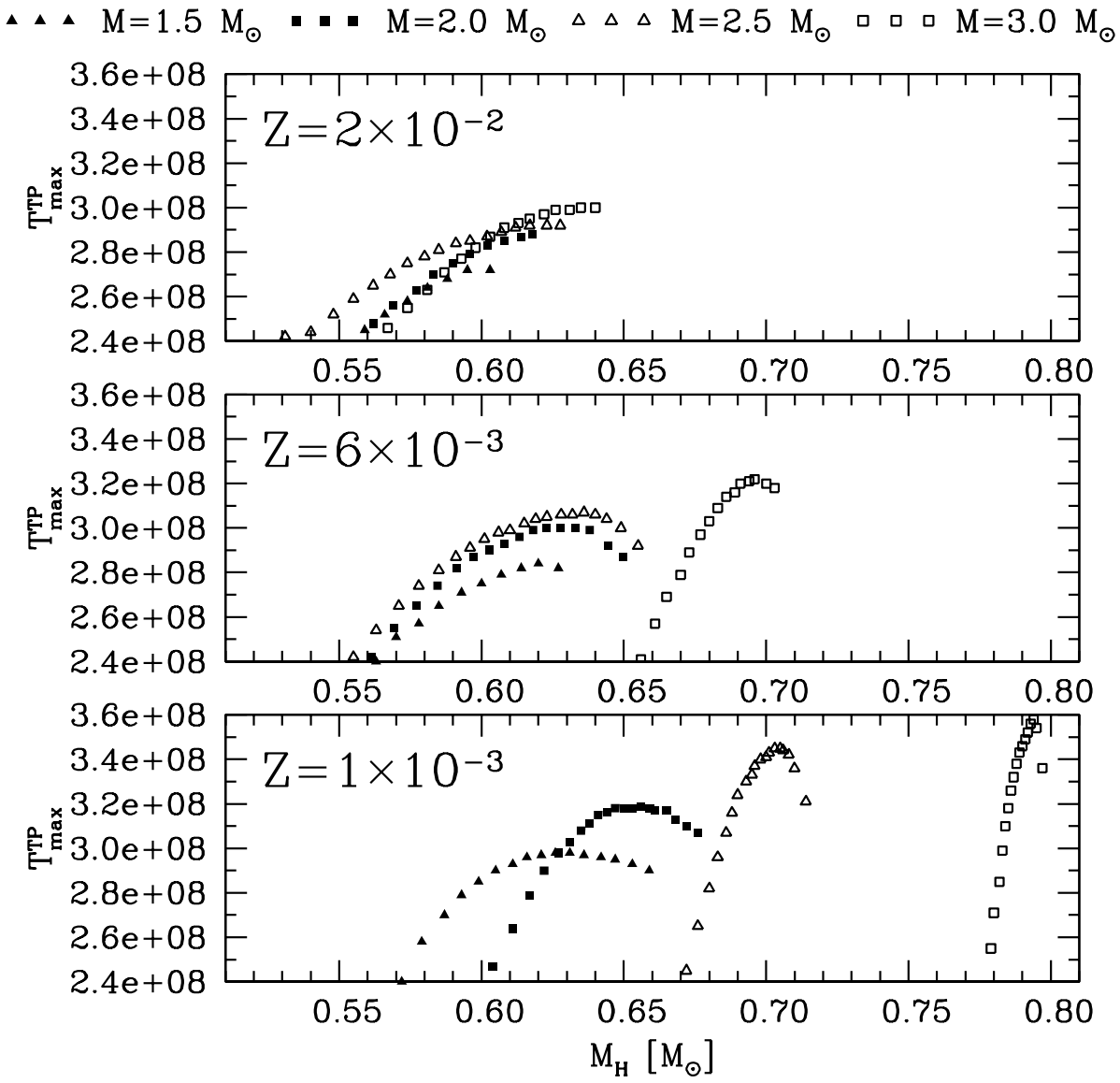


Fig. 4.— As in Fig. 2, but for the maximum temperature attained at the bottom of the convective zone generated by a TP.

$^{86}$Kr, $^{87}$Rb and $^{96}$Zr). In addition, light-*s* (ls) elements[14] are efficiently produced as a consequence of the rapid mixing taking place in the convective shell. On one hand, this mixing continuously provides fresh Fe seeds in the innermost (and hotter layers) of the convective zone. On the other hand, it prevents the pile up of the synthesized material, which is required to build up the heaviest species (as it occurs during the radiative $^{13}$C burning within the pockets).

## 3. Nucleosynthesis

Three main peaks are expected in the *s*-process distribution. They correspond to nuclei with a magic number of neutrons (50, 82 and 126), whose binding energy is particularly high and, in turn, the neutron capture cross-section is particularly low. The average abundances of *s*-process elements around N=50 and N=82 represent respectively the so-called ls (light *s*) and hs (heavy *s*) indexes. As in Paper I, we define:

- [ls/Fe]=([Sr/Fe]+[Y/Fe]+[Zr/Fe])/3;
- [hs/Fe]=([Ba/Fe]+[La/Fe]+[Nd/Fe]+[Sm/Fe])/4.

The third peak (at N=126) is represented by lead ([Pb/Fe]). Combining these quantities, the spectroscopic indexes [hs/ls] , [Pb/ls] and [Pb/hs] can be derived[15]. Basing on simple arguments, Cameron (1957) demonstrated that these spectroscopic indexes basically depend on the number of neutrons available per iron seed for the first time. In stellar interiors, however, the physical and chemical conditions may be more complex. In the case of

[14]Those belonging to the first peak of the *s*-process (ls, light elements: Sr-Y-Zr). See next Section.

[15]We adopt the usual spectroscopic notation: [a/b]=log(a/b)-log(a/b)$_\odot$

the radiative $^{13}$C burning taking place during the interpulse period in low mass AGB stars, the number of neutrons corresponds to the number of $^{13}$C nuclei in the pocket. However, most of these neutrons are captured by light elements (poisons) and do not contribute to the *s*-process. As already specified in Section 2.1, $^{14}$N (the most abundant poison in our models) partially recycles neutrons. Nevertheless, as a first order approximation, we may assume that the number of neutrons per seed available for the *s*-process is given by:

$$\frac{n(neutrons) - n(poisons)}{n(seeds)} \sim \frac{n(^{13}\mathrm{C}) - \mathrm{n}(^{14}\mathrm{N})}{n(^{56}\mathrm{Fe})} \quad (1)$$

The numerator of this equation coincides with the *effective* $^{13}$C introduced in Section 2.1. Within the $^{13}$C pocket it varies according to the protons profile left by the TDU. Note that both the $^{13}$C and the $^{14}$N in the pocket share the same (primary) origin, since both are built from the primary $^{12}$C[16]. On the contrary, the iron abundance within the pocket depends on the initial stellar metallicity.

The behavior of the three *s*-process peaks at the last TDU as a function of the metallicity and for different masses is illustrated in Fig. 5. For selected masses and metallicities, the corresponding values are reported in Table 6. More complete Tables can be downloaded from the FRUITY web-based platform. We find that [ls/Fe] is barely flat for all the metallicities, the only 1.5 $M_{\odot}$ exhibiting a mild increase when decreasing the metal content. As to [hs/Fe], all masses show a steep increase with the metallicity. This behavior is even more evident for [Pb/Fe], which peaks at the lowest computed metallicity. Given the steep increase of the neutrons per iron seed with decreasing metallicity (see column 13 in Tables 3, 4 and 5), the heaviest species are easier synthesized at low $Z$. In Fig. 6 we report the *s*-process spectroscopic indexes [hs/ls] (upper panel) and [Pb/hs] (lower panel). The first quantity continuously grows with decreasing metallicity, reaching

[16]Primary elements are direct by-products of H or He burning.

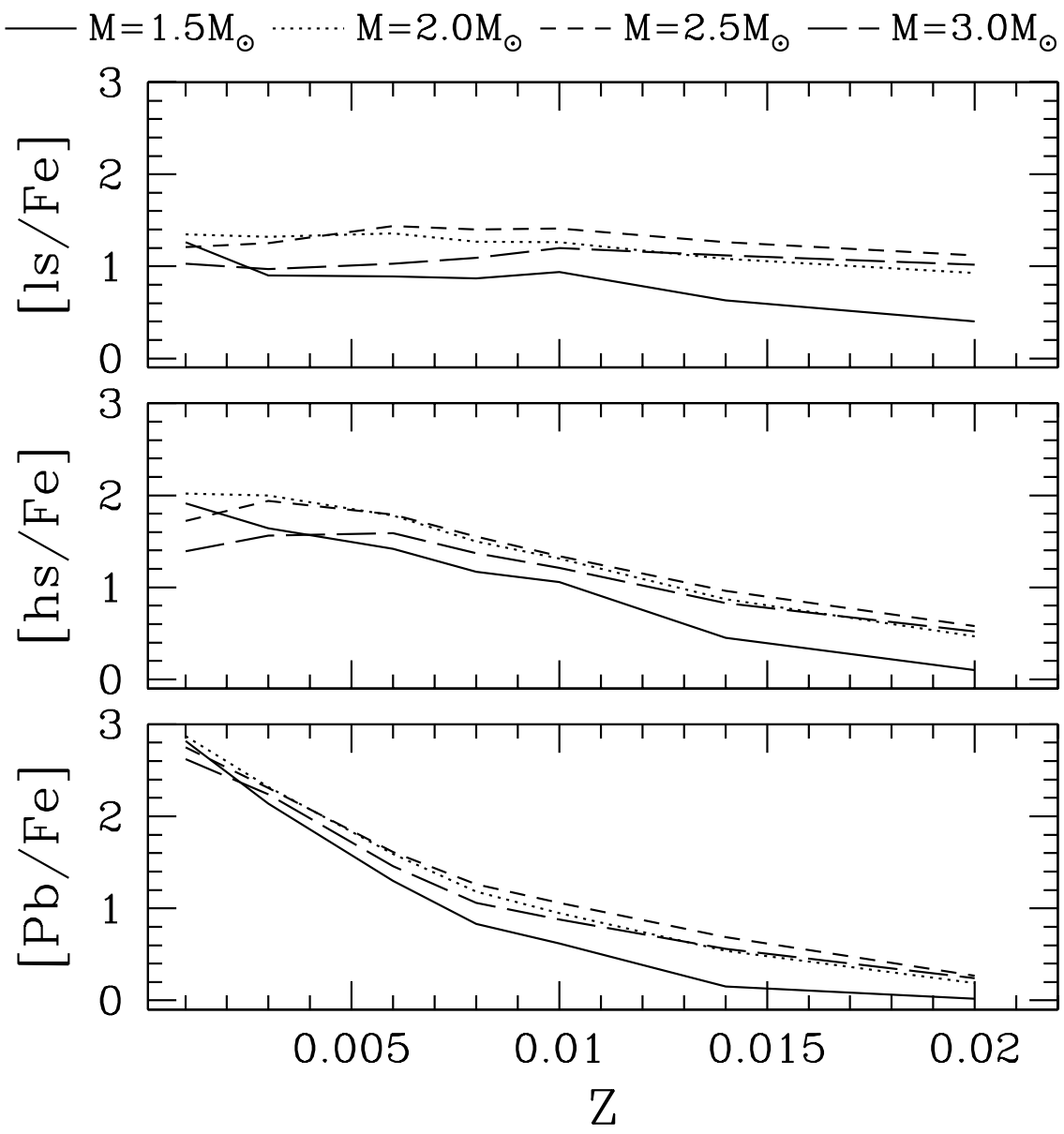


Fig. 5.— Behaviors of the three *s*-process peaks ([ls/Fe], top panel; [hs/Fe], middle panel; [Pb/Fe], lower panel) as a function of the metallicity predicted by our models for different initial masses.

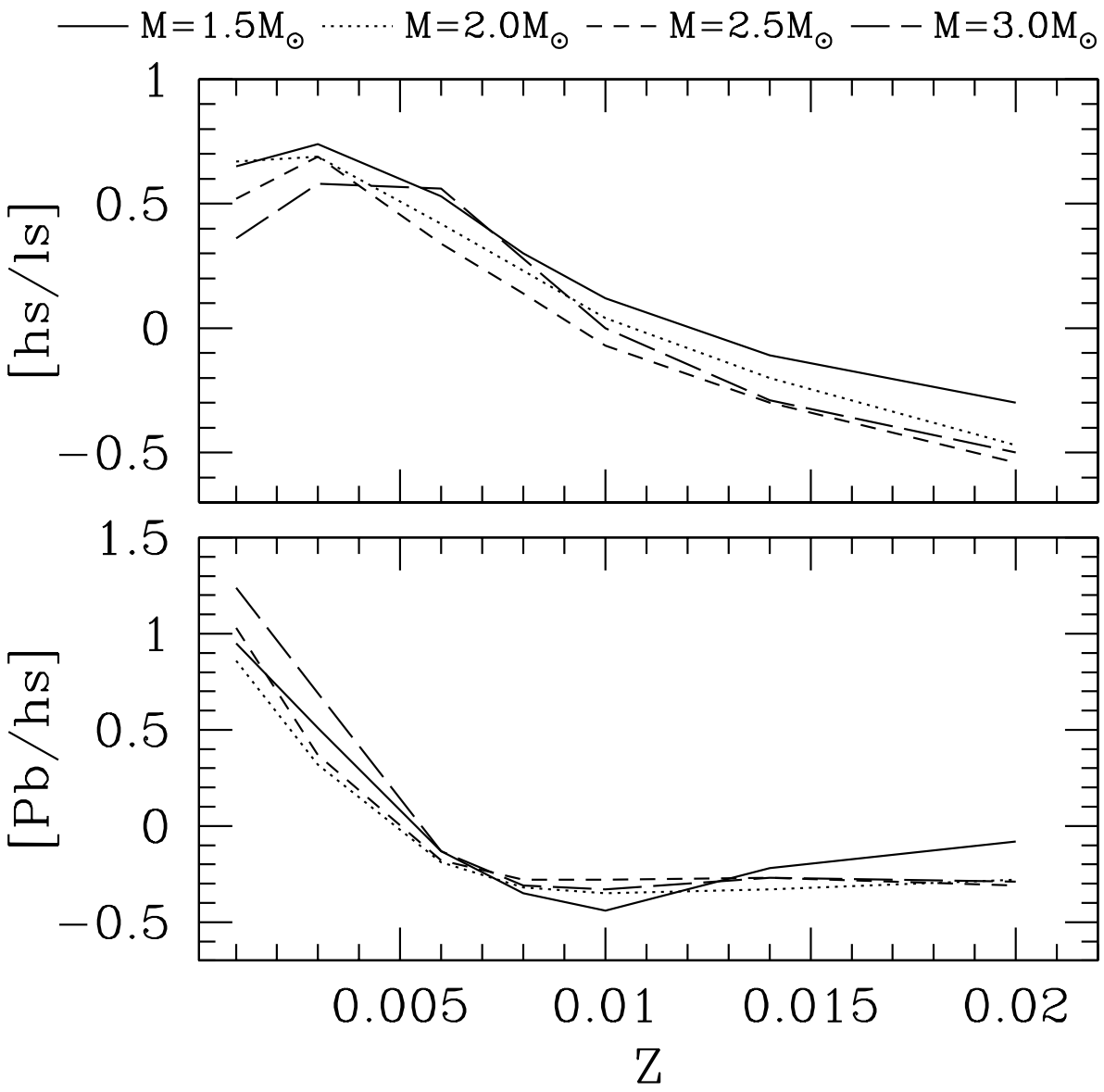


Fig. 6.— As in Fig. 5, but for the *s*-process indexes [hs/ls] (upper panel) and [Pb/hs] (lower panel).

a maximum at $Z \sim 3 \times 10^{-3}$ (eventually decreasing at lower metallicities), while [Pb/hs] shows a flat profile from $Z \sim 2 \times 10^{-2}$ down to $Z \sim 6 \times 10^{-3}$ and then grows at the lowest metallicities. A full discussion on the behavior of these quantities as a function of the metal content can be found in Bisterzo et al. (2010). As already outlined, these quantities mainly depend on the neutrons per iron seed and on the abundances of neutron poisons. In our models, the amount of $^{13}$C in the pockets basically depends on the core mass (see Fig. 1). At fixed metallicity the core masses for different models do not vary much (apart from the $Z = 1 \times 10^{-3}$ models, but see below) and, therefore, there is no particular trend with the initial mass. Our spread at fixed metallicity reflects the slight variation of the total number of neutrons per iron seed in each pocket for different initial masses. This limited spread derives from the fact that, in our models, only convection is considered as a mixing mechanism: the introduction of additional mixing phenomena (such as rotation; see e.g. Langer et al. 1999 and Herwig et al. 2003), able to dilute the available $^{13}$C on a larger mass region, could lead to a lower neutron to seed ratio (see Section 6.2).

Other interesting nucleosynthetic features emerge from the analysis of light elements (see Table 6, in which the final C/O, C/N and $^{12}$C/$^{13}$C ratios are also given). Among them, carbon and fluorine show a clear anti-correlation with the initial metallicity. Carbon is of primary origin, because it is produced during TPs via the $3\alpha$ reaction. The production of fluorine basically depends on the availability of $^{13}$C in the He-intershell (see Paper I for a detailed description of the nuclear chain leading to $^{19}$F nucleosynthesis; see also Jorissen et al. 1992; Forestini et al. 1992; Mowlavi et al. 1996; Lugaro et al. 2004; Abia et al. 2010, 2011). A non negligible amount of $^{13}$C is available within the $^{13}$C-pocket and in the ashes of the H-burning shell. As already discussed in Paper I, the former is weakly dependent on metallicity. The latter directly scales with the CNO abundances in the envelope, which, in turn, depend on the (primary) $^{12}$C dredged-up during all previous TDU episodes. The resulting fluorine can be roughly considered a primary element.

The nitrogen surface enrichment is mainly a consequence of the FDU and, at the lowest metallicities, of the H-shell erosion by the envelope during TDU episodes. This latter contribution is not appreciable at higher metallicities because of the already large $^{14}$N surface abundance.

The neon surface enrichment derives by the dredge-up of $^{22}$Ne, which is synthesized during TPs via the nuclear chain $^{14}$N($\alpha$,$\gamma$)$^{18}$F($\beta^+\nu$)$^{18}$O($\alpha$,$\gamma$)$^{22}$Ne. Direct evidence of neon production has recently been detected in Galactic planetary nebulae (Milingo et al. 2010). Since the nitrogen abundance in the He-intershell depends on the quantity of carbon previously dredged-up (due to the conversion of $^{12}$C to $^{14}$N via the CNO cycle), $^{22}$Ne is a primary element (thus its surface overabundance is expected to increase at low metallicities).

In our models, sodium can be synthesized via proton or neutron captures (see also Mowlavi 1999). A sodium pocket forms via the $^{22}$Ne(p,$\gamma$)$^{23}$Na reaction in the upper part of the He-intershell, where protons are left by the receding convective envelope after TDU episodes (see Paper I). Moreover, $^{23}$Na is synthesized via the $^{22}$Ne(n,$\gamma$)$^{23}$Ne($\beta^-\nu$)$^{23}$Na nuclear chain, during both the radiative burning of the $^{13}$C-pocket and the convective $^{22}$Ne burning in the TPs.

Magnesium isotopes follow different nucleosynthetic paths. $^{24}$Mg, which is the most abundant magnesium isotope in the Sun, is marginally produced via neutron captures on $^{23}$Na during the radiative burning of the $^{13}$C pocket and it is weakly destroyed during TPs. On the contrary, $^{25}$Mg and $^{26}$Mg are mainly created during TPs via neutron captures processes and via the $^{22}$Ne($\alpha$,n)$^{25}$Mg and the $^{22}$Ne($\alpha$,$\gamma$)$^{26}$Mg reactions (which contribute to the $^{25}$Mg and $^{26}$Mg nucleosynthesis, respectively). In our models we generally find a low final surface magnesium enrichment, with an increasing trend toward low metallicities. This derives from the larger relative contribution of $^{25}$Mg and $^{26}$Mg, due to the increased efficiency in the activation of the $^{22}$Ne($\alpha$,n)$^{25}$Mg and $^{22}$Ne($\alpha$,$\gamma$)$^{26}$Mg reactions (see Section

2.1).

All our models become C-rich (*i.e.* their final C/O>1), but the 1.5 $M_{\odot}$ model at $Z = 2 \times 10^{-2}$. As already mentioned, non convective mixing episodes (the so-called extra-mixing) for both the RGB and the AGB phases are not considered in these models. The origin of this extra-mixing is far from being established on theoretical grounds. The precise estimate of its efficiency during both the giant branches can be obtained only by comparing parameterized models with observational constraints (Charbonnel & Zahn 2007; Eggleton et al. 2008; Nordhaus et al. 2008; Denissenkov et al. 2009; Busso et al. 2010; Denissenkov 2010; Palmerini et al. 2011; Denissenkov et al. 2011). The extra-mixing is expected to affect the CNO abundances, with a substantial reduction of the $^{12}C/^{13}C$ isotopic ratio (see also Lebzelter et al. 2008; Lederer et al. 2009) and, eventually, a lowering of the C/O and C/N ratios. For this reason, special attention has to be paid when comparing the surface abundances of these elements (or isotopes) with their observed counterparts.

A selection of net stellar yields for different masses and metallicities is reported in Tables 7, 8 and 9 (full Tables are available on line at FRUITY web pages). These data represent the first homogeneous set of light and heavy elements theoretical yields for AGB stars. The completeness of our database could help to reduce the uncertainties affecting Galactic chemical evolutionary models, as underlined by Romano et al. (2010). At high metallicities ($Z \sim 2 \times 10^{-2}$), the largest absolute yields (for both light and heavy elements) come from the 2.5 $M_{\odot}$ and the 3.0 $M_{\odot}$. At lower metallicities ($Z \sim 6 \times 10^{-3}$) the principal contribution derives, for all chemical species, from the 2.5 $M_{\odot}$ model. At $Z \sim 10^{-3}$, the initial mass of the principal polluter further decreases, presenting the largest yields in the 2.0 $M_{\odot}$ mass. Weighing the yields with an Initial Mass Function (IMF), for example the one proposed by Salpeter (1955), the contribution from the 2.0 $M_{\odot}$ stars dominates at all metallicities.

The amount of processed material from various masses at different metallicities results from a combination of many factors, as the core mass, the efficiency of TDU, the envelope mass, the number of TPs, the thickness of $^{13}$C pockets and the surface temperature (which drives the mass-loss rate). As a rule of thumb, a progressive decrease of the metallicity leads to a reduction of the yields from stars with $M \sim (2.5 \div 3.0) M_{\odot}$, making stars with $M \sim (1.5 \div 2.0) M_{\odot}$ the principal polluters of the ISM. Note that, as already pointed out, the explicit treatment of physical phenomena currently not accounted for (such as rotation) could significantly modify these quantities and, in particular, the surface distributions of the heavy elements.

In order to better interpret the nucleosynthetic paths described above, we highlight some general rules characterizing our models:

- the main neutron source is represented by the radiative burning of $^{13}$C within the pockets;
- the nucleosynthesis occurring in the first 4−5 pockets mainly determines the final surface distributions;
- the contribution of the additional $^{22}$Ne($\alpha$,n)$^{25}$Mg neutron burst is generally negligible;
- the efficiency of the TDU increases with decreasing the metallicity;
- at fixed metallicity, the surface chemical enrichment basically depends on the total amount of dredged-up material and on the mass extension of the convective envelope[17].

However, there are a few exceptions. As already described in Paper I, the first $^{13}$C-pocket of the 2 $M_{\odot}$ models does not completely burn during the radiative interpulse period and some

[17]See Section 4 for a discussion about the effects induced by different mass-loss rates on the final elemental surface abundances.

$^{13}$C is ingested and burnt convectively in the following TP. We confirm this finding for the other masses. This episode has no effects on the physical evolution of the TP, while it has interesting effects from an isotopic point of view. In particular, the large neutron densities attained (see Paper I) allow the nucleosynthesis of some neutron-rich isotopes, such as the short lived $^{60}$Fe.

A characteristic feature of our 3 $M_{\odot}$ model at $Z = 10^{-3}$ is represented by the occurrence of the so-called Hot-TDU (Goriely & Siess 2004; Herwig 2004; Campbell & Lattanzio 2008; Lau et al. 2009). In fact, for this model proton captures occur at the base of the convective envelope during the TDU phase. In Paper I, we already found the Hot-TDU to occur in the M=2 $M_{\odot}$ model with $Z = 10^{-4}$. As a first consequence, the model shows a definitely lower $^{12}$C/$^{13}$C isotopic ratio with respect to other masses (see Table 6). Note that the occurrence of the Hot-TDU depends on the mixing algorithm we applied at the inner border of the convective envelope (see Section 2). The calibration of its $\beta$ parameter has been done in order to maximize the *effective* $^{13}$C in the pockets and, consequently, the resulting *s*-process nucleosynthesis. Actually, it is not clear if the same calibration can be also applied to AGB stars developing a larger core mass, as our 3 $M_{\odot}$ model at $Z = 10^{-3}$. With respect to the other calculated masses, this model also reaches higher temperatures during TPs, which imply a more efficient activation of the $^{22}$Ne($\alpha$,n)$^{25}$Mg neutron source. This leads to a non negligible contribution to [ls/Fe]. Consequently, the [hs/ls] index decreases, leading to a larger spread of this quantity when compared to the other metallicities.

It is worth to mention that the nucleosynthesis of some isotopes (the ones whose production requires a high neutron density) is favored by the activation of the $^{22}$Ne neutron source. In Table 10 we list some isotopic ratios involved in branchings along the *s*-process path. The dependence on the metallicity has already been discussed in Paper I, demonstrating that these ratios increase with decreasing metallicity, due to the increased contribution to the *s*-process nucleosynthesis of the $^{22}$Ne($\alpha$,n)$^{25}$Mg. The dependence of the corresponding

isotopic ratios on the initial mass is clearly shown in Table 10. With the exception of the most metal-rich models, the 3 $M_{\odot}$ models show the largest ratios, confirming again that the $^{22}$Ne($\alpha$,n)$^{25}$Mg neutron source is particularly important for the more massive AGB stars.

## 4. Theoretical uncertainties

When dealing with observations, it is mandatory to perform a detailed discussion of the errors introduced by the instruments and the techniques adopted to analyze data. A similar procedure should be followed when computing theoretical stellar models. In this case, error-bars cannot be derived (due to the high degree of degeneracy among the input parameters), but the sensitivity of the model with respect to changes in the input physical parameters can be evaluated. A similar analysis was already performed in Paper I for a 2 $M_{\odot}$ AGB model with $Z = 10^{-4}$. Considering the larger metallicities of the models presented in this work, we focus on a $M = 2M_{\odot}$ with $Z = 6 \times 10^{-3}$ (hereafter FRANEC Standard Model, FSM). We assume as our FSM the model computed with the following set of parameters:

- the free parameter of the mixing length theory is set to $\alpha_{\rm FSM}$=2.15 (see Paper I);
- the AGB mass-loss rate ($\dot{M}^{\rm AGB}_{\rm FSM}$) is empirically calibrated on the observed period-luminosity relation (see Straniero et al. 2006 for details);
- the free parameter that determines the decreasing profile of the convective velocities at the base of the envelope is set to $\beta_{\rm FSM}$=0.1 (see Paper I).

In order to estimate the sensitivity of our models to the afore-listed inputs we calculate six test models. We vary the mixing length parameter $\alpha$, the mass loss law and the $\beta$ parameter which governs the efficiency of the velocity profile at the border of the convective envelope:

1. $\alpha_1 = \alpha_{\rm FSM} + 0.35 = 2.5$;

2. $\alpha_2 = \alpha_{\rm FSM} - 0.35 = 1.8$;

3. $\dot{M}_1^{\rm AGB} = \dot{M}_{\rm FSM}^{\rm AGB} * 2$;

4. $\dot{M}_2^{\rm AGB} = \dot{M}_{\rm FSM}^{\rm AGB} * 0.5$;

5. $\beta_1 = \beta_{\rm FSM} + 0.02 = 0.12$;

6. $\beta_2 = \beta_{\rm FSM} - 0.04 = 0.06$.

A variation of the mixing length parameter $\alpha$ affects not only the temperature run in the more external layers of the star, where the local temperature gradients largely deviate from the adiabatic value, but also the velocity profile of the convective bubble in the whole convective envelope (see Piersanti et al. 2007).

We evaluate the effects of a variation of the AGB mass-loss rate by multiplying or dividing its efficiency by a factor 2. At fixed pulsational period, the resulting theoretical mass loss laws reproduce the minimum and the maximum mass-loss rates observed in Galactic AGB stars (see Figure 3 of Straniero et al. 2006).

Finally, we present two models with a different $\beta$ parameter in order to estimate the effects induced by a change in the slope of the exponentially decreasing profile of convective velocities at the base of the envelope. We choose values leading to a reduction of the *effective* $^{13}$C within the pockets by roughly a factor 4 with respect to our FSM (see Figure 7 of Paper I).

In Table 11 we report, for our FSM, the final core mass ($M_{\rm H}$), the mean bolometric magnitude of the AGB C-rich phase ($\overline{\rm M}_{\rm bol}^{C}$)[18], the duration of the AGB C-rich phase ($\tau_C$),

[18]Calculated as the average luminosity weighted over the time spent by the star on the AGB when C/O>1.

the $^{12}$C yield (as representative of primary-like light isotopes), the $^{89}$Y, $^{139}$La and $^{208}$Pb yields (as representative of the three *s*-process peaks) and the final [hs/ls] ratio. For the test cases, we list normalized percentage differences with respect to the FSM.

The physical quantities listed in Table 11 (final core mass, mean bolometric magnitude of the C-rich phase and duration of the C-rich phase) mildly depend on the choice of the input parameters. Maximum variations are below 30%. This makes our theoretical models quite robust when comparing with the observed counterparts (see Section 6.1).

The test with an enhanced $\alpha$ parameter and the test with a reduced mass loss rate present similar trends: the mean bolometric magnitude of the C-rich phase decreases (and, thus, the mean luminosity increases), while the C-rich phase duration and the chemical yields increase. The reason is twofold. In fact, a higher $\alpha$ parameter implies more efficient TDUs and a slightly higher surface temperature, which translates into a milder mass loss rate. An opposite trend is found for the test with a reduced $\alpha$ parameter which, thus, resembles the test with an increased mass loss rate. Note that, for the aforementioned test models, the heavy elements yields roughly scale as the light ones and the final chemical patterns show minor changes with respect to the FSM (see their [hs/ls] ratios).

A different prescription for the mass loss law leads to negligible differences in the *s*-process abundances because the first $^{13}$C pockets largely determine the final heavy elements enrichment in the envelope. For the same reason, minor changes in the relative abundances of *s*-process elements are found in the $\alpha$-varied tests, even if a variation of this parameter leads to different TDU efficiencies. However, a further aspect has to be analyzed. Within the framework of the mixing length theory, the value of the convective velocities directly scales with $\alpha$. Thus, a variation of such a parameter should also modify the efficiency of the mixing algorithm we adopt at the base of the convective envelope. However, we verified that this has minor effects on the formation of the $^{13}$C pockets, with variations lower than 15% in the *effective* $^{13}$C. This is not the case for the two tests with a different $\beta$ parameter.

In fact, these models present complete different heavy elements distributions with respect to the FSM. In both cases there is a sensible decrease of the absolute surface abundances (as proved by the yields) and a change in the final shape of the *s*-process distribution (as showed by the [hs/ls] ratios). This is due to the fact that the amount of neutrons available for the nucleosynthesis of heavy species within the $^{13}$C pockets decreases in both cases. The reasons are, however, different. In the $\beta$=0.06 case, the total amount of $^{13}$C within the pockets strongly decreases due to the steeper decreasing profile of convective velocities. Instead, in the $\beta$=0.12 case the $^{13}$C pocket is completely overlapped with the $^{14}$N pocket. This acts as a neutron poison via the resonant $^{14}$N(n,p)$^{14}$C reaction, thus penalizing the heavy elements nucleosynthesis (see Section 3).

## 5. Comparison with other stellar models

In previous Sections we discussed in detail our theoretical models, by analyzing their physical and chemical properties as a function of the initial mass and metal content. Moreover, we evaluated the uncertainties deriving from different choices of the input parameters. In this Section we present a comparison between our results and other evolutionary stellar models available in the literature. A similar comparison is in general not straightforward, since the various codes significantly differ in many of the adopted input physics (treatment of convection, definition of convective borders, mass-loss law, initial chemical abundances, opacities, equation of state and nuclear network). As already discussed in Section 2, during the pre-AGB phase our models are very similar to those presented in Domínguez et al. (1999). We refer to that paper for a comparison between different codes. As discussed in Straniero et al. (2003a), a key physical quantity to understand AGB evolution is the core mass at the beginning of the TP-AGB phase (we identify it as the core mass at the first TP in which the helium luminosity exceeds $10^4 L_{\odot}$,

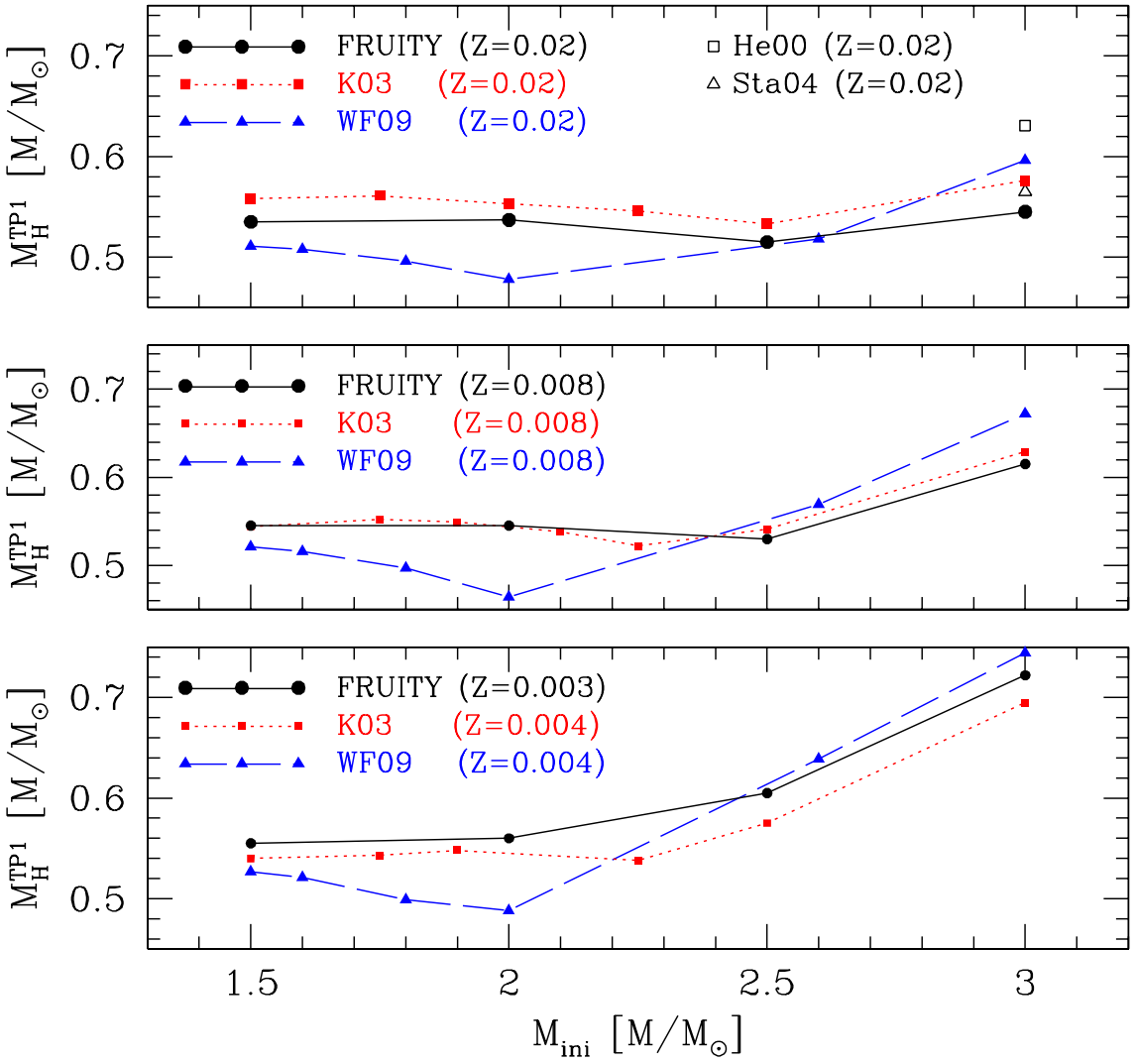


Fig. 7.— Core mass at the first TP as a function of the initial stellar mass at various metallicities and for different authors (FRUITY: this paper; K03: Karakas 2003; WF09: Weiss & Ferguson 2009; He00: Herwig 2000; Sta04: Stancliffe et al. 2004).

$M_{\rm H}^{\rm TP1}$). In Fig. 7 we plot our $M_{\rm H}^{\rm TP1}$ for three selected metallicities ($Z = 0.02$, $Z = 0.008$ and $Z = 0.003$) and compare them to models from Karakas (2003) (hereafter K03) and Weiss & Ferguson (2009) (hereafter WF09). For the $M = 3M_{\odot}$ model with $Z = 0.02$ we also report data from Herwig (2000) (hereafter He00) and Stancliffe et al. (2004) (hereafter Sta04).

The value of $M_{\rm H}^{\rm TP1}$ basically depends on the core mass attained at helium ignition ($M_{\rm He}^{1}$ in Table 2) and on the duration of core He-burning. $M_{\rm He}^{1}$ is built during the RGB phase for an initial mass lower than 2 $M_{\odot}$. $M_{\rm He}^{1}$ depends on several input physics, like the neutrino cooling rate, the $^{14}$N(p,$\gamma$)$^{15}$O reaction rate and the equation of state for the degenerate matter of the RGB core (including the Coulomb correction). For higher initial masses, which develop a sizeable convective core during central H-burning, the treatment of convection (overshoot or not) may also affect $M_{\rm He}^{1}$. On the other hand, the duration of the core He-burning phase depends on the treatment of convection (semi-convection or mechanical overshoot) and on the adopted values for the key reaction rates 3$\alpha$ and $^{12}$C($\alpha$,$\gamma$)$^{16}$O. In addition, we stress that the difference in the initial H and He abundance has a significative influence on the whole stellar model evolution.

Our models are in fair agreement with those presented by K03, who operated similar choices (no core overshoot during core H-burning and semi-convection during core He-burning). A similar $M_{\rm H}^{\rm TP1}$ is also attained by Sta04, who also did not apply convective overshoot. Note that Sta04 simultaneously solve the equations of the chemical evolution (including the convective mixing) and those of the physical evolution. Such numerical algorithm could mimic a treatment of semi-convection similar to the one we adopt. The reason of the notable difference between our models and the WF09 ones for the $M = 2M_{\odot}$ masses is not clear. We note that, for these masses, the duration of their core He-burning phase is larger than ours. Such an occurrence suggests that their $M_{\rm He}^{1}$ should be lower than ours (lower He core masses imply lower luminosities and then larger He-burning lifetimes). Unfortunately,

WF09 did not report $M^1_{\rm He}$. On the contrary, their $M = 3M_\odot$ models have larger $M^{\rm TP1}_{\rm H}$ than us and K03. This could derive from the application of convective overshoot during central H-burning. Note that an even larger $M^{\rm TP1}_{\rm H}$ is attained by He00, who also applied overshoot during both core hydrogen and helium burnings.

In order to compare the TDU efficiency among different codes, in Fig. 8 we report the variation of the $\lambda$ factor as a function of the core mass for our AGB model with $M = 3M_\odot$ and $Z$=0.02. We plot the same quantity for a model computed with an older version of the FRANEC code (Straniero et al. 1997) (hereafter Stra97) and for calculations by other authors (He00; Sta04; Karakas & Lattanzio 2007, hereafter K07). The TP-AGB phase of the Stra97 model was computed without the exponentially decaying profile of convective velocities at the base of the convective envelope (see Section 2). As a by-product, the TDU efficiency increases (in fact the maximum $\lambda$ grows from their 0.4 to the current 0.6) and, in addition, the TDU occurs earlier (see also the K07 model). Further differences can be ascribed to the adopted mass-loss law. In fact, as shown by Straniero et al. (2003a), the TDU efficiency, and then $\lambda$, substantially depends on the residual envelope mass. The K07 model is calculated with a milder mass-loss rate than the one adopted by Stra97 (Reimers' formula with $\eta$=3 during the AGB phase). Thus, for the same core mass, their model has a larger envelope mass and, in turn, larger $\lambda$ values. For the same reason, the Sta04 model, which is calculated without mass-loss, attains larger $\lambda$ values than ours. Note that the most efficient TDU is obtained by He00, even if he included a moderate mass-loss (Reimers' formula with $\eta$=1 during the AGB phase). However, in his model the convective overshoot is also applied at the base of the convective shells, this fact causing stronger TPs and, consequently, more efficient TDUs (see Lugaro et al. 2003). Finally, further differences could be ascribed to the choice of the $^{14}$N(p,$\gamma$)$^{15}$O reaction rate (Straniero et al. 2000; Herwig & Austin 2004).

The Forestini & Charbonnel (1997) and the Karakas (2010) (hereafter K10) are the

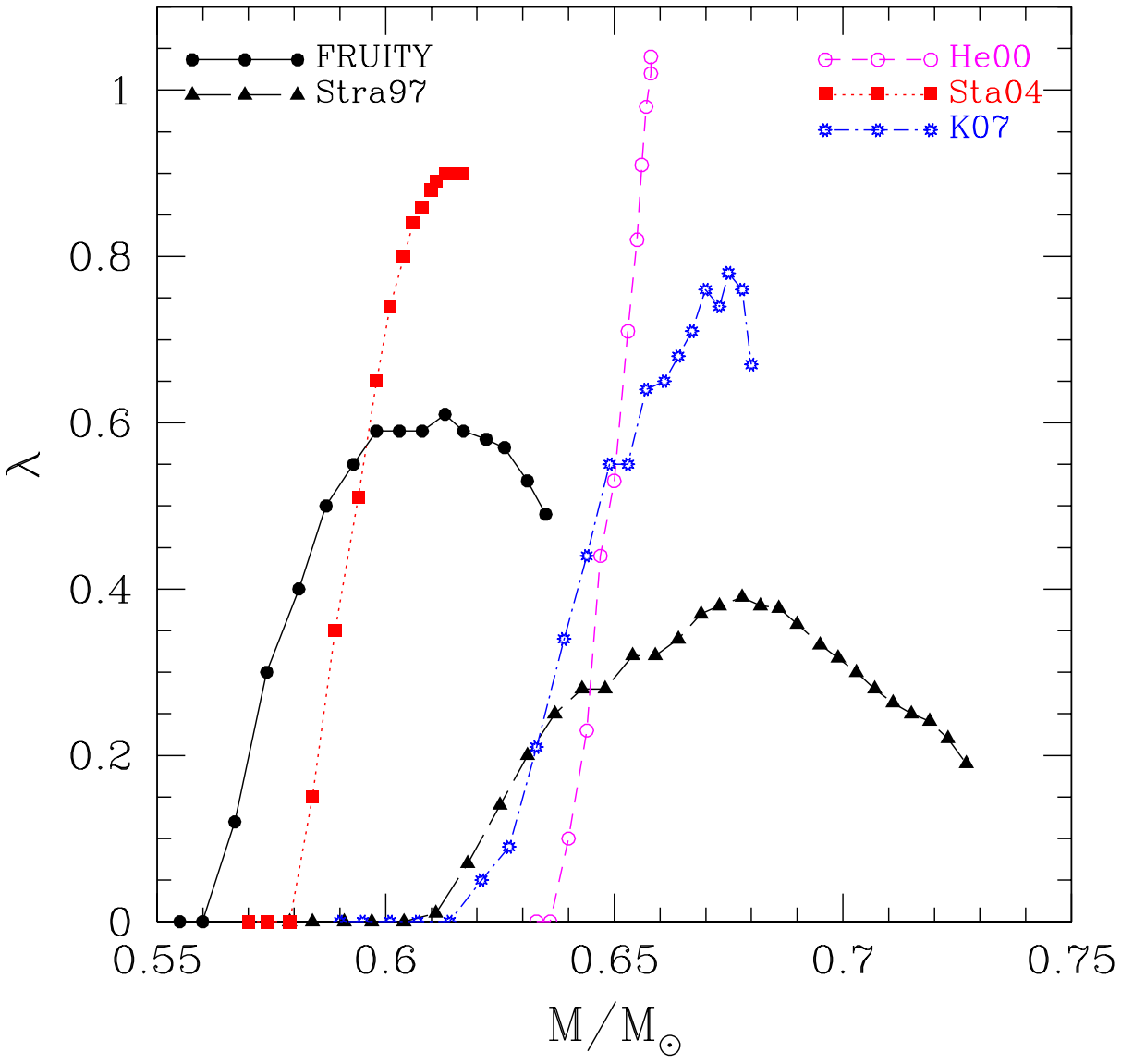


Fig. 8.— $\lambda$ factor as a function of the core mass for an AGB model with $M = 3M_{\odot}$ and $Z$=0.02 as reported by different authors (FRUITY: this paper; Stra97: Straniero et al. 1997; He00: Herwig 2000; Sta04: Stancliffe et al. 2004; K07: Karakas & Lattanzio 2007).

only papers we found in the literature in which yields from full stellar evolutionary AGB models have been discussed (we exclude synthetic yields from our analysis; see e.g. Groenewegen & De Jong 1994 and Marigo 2001). We compare the yields of our $M = 3M_{\odot}$ and $Z$=0.02 model with the one presented by K10, by considering her model including a partial mixing zone of $2 \times 10^{-3} M_{\odot}$ after any TDU episode. For its physical characteristics, it is the most similar model to ours; as a matter of fact, the cumulatively dredged-up masses are nearly the same ($M_{\rm TDU}^{\rm K10} = 7.93 \times 10^{-2} M_{\odot}$; $M_{\rm TDU}^{\rm FRUITY} = 7.54 \times 10^{-2} M_{\odot}$, see Table 3). Note that while we have computed a full network stellar model calculations, the yields presented by K10 are obtained by means of a post-process calculation. In Table 12 we report a selection of net stellar yields. The analysis is limited to light isotopes since heavy elements are not included in K10 calculations. For each isotope we report our net yield (labelled as FRUITY), the corresponding value tabulated in K10 and the percentage difference. In spite of the many physical differences, the resulting yields show a reasonable agreement. The differences concerning $^{20}$Ne, $^{24}$Mg and $^{28}$Si basically derive from the small AGB net production (or destruction) as compared to their initial abundances.

## 6. Comparison with observations

In the previous Section, we presented a comparison among our models and other models available in the literature. As we have shown, the different results can be ascribed to the different adopted input physics. This comparison, however, does not indicate the most reliable input physics or numerical scheme to be preferred. In order to do that, we have to be guided by observations. This is the purpose of the present Section, where we compare our theoretical models to observational counterparts. Here we concentrate on the Luminosity Function of Carbon Stars and the *s*-process spectroscopic indexes at different metallicities.

### 6.1. Luminosity Function of Carbon Stars

As already outlined in previous Sections, the majority of our TP-AGB models present final C/O ratios larger than 1; thus, their observational counterparts are C-rich stars. The Luminosity Function of Carbon Stars (hereafter LFCS) represents a good test indicator for our theoretical prescriptions, given that it links a physical quantity (the luminosity) with the chemistry of the model (its surface carbon abundance). By comparing our theoretical LFCS with observational data, we can simultaneously check if the final structure (basically the core mass) and the surface chemical abundances of our models (which depend on the TDU efficiency and the mass loss law) are reliable or not.

Iben (1981) firstly highlighted the incapability of theoretical AGB models to reproduce the LFCS of Magellanic Clouds. In his models, TDU was found to occur for core masses larger than 0.6 $M_{\odot}$ (thus corresponding to AGB stars of Intermediate Mass: $4 < M/M_{\odot} < 7$). However, in these objects the temperature at the base of the convective envelope is high enough to activate an efficient hydrogen burning. This phenomenon, known as Hot Bottom Burning (Sugimoto 1971; Iben 1973; Karakas 2003; Ventura & D'Antona 2005), basically prevents these stars from becoming C-rich, due to the conversion of the dredged-up carbon into nitrogen[19]. Therefore, a discrepancy between theory and observations arose, called "carbon stars mystery" (Iben 1981). Later, Lattanzio (1989) and Straniero et al. (1997) found TDU to occur in stars with masses as low as 1.5 $M_{\odot}$, thus allowing the possibility to form C stars at lower luminosities. Notwithstanding, Izzard et al. (2004) concluded that full stellar evolutionary models cannot reproduce the Magellanic Clouds LFCS, being the evolutionary models too luminous with respect to the observed distributions. These authors concluded that TDU must operate earlier on the AGB or at lower core masses. More recently, two groups (Stancliffe et al. 2005; Marigo & Girardi 2007) stated to have

[19]Note that none of the models presented in this paper suffers for Hot Bottom Burning.

reproduced the LFCS of Magellanic Clouds. Stancliffe et al. (2005) achieved a good agreement for the Large Magellanic Cloud and suggested a shift toward lower masses for stars experiencing TDU in order to reproduce the LFCS of the Small Magellanic Cloud. A full match for both the Magellanic Clouds LFCS has been found by Marigo & Girardi (2007). However, these authors used synthetic stellar models and their agreement derives from the ad-hoc calibration of stellar properties during the TP-AGB phase (in particular the onset and efficiency of the TDU process).

A different approach has been followed by Guandalini et al. (2006), who performed an analysis of Galactic carbon stars at infrared (IR) wavelengths. They suggested that the inconsistency between theory and observations is due to the underestimation of the IR contribution of these objects. In fact, since these stars are very cool, they emit a large part of their radiation at IR wavelengths. Actually, these authors found a distribution peaked at $M_{bol} = -5$, thus in better agreement with model predictions, with a non negligible luminous tail up to $M_{bol} = -6$. It has to be stressed that their sample contains a large fraction of stars (about 45%, see their Table 3) whose distance is poorly known and should be better determined. The use of recently improved observational data (in particular distances) could lead to significant changes in their observed LFCS.

In Fig. 9 we report our theoretical LFCS (solid histogram) and a revised version of the observed Galactic LFCS presented by Guandalini et al. 2006 (dotted histogram; *courtesy of R. Guandalini*). The $y$-axis (fractional numbers) is defined as the fraction of carbon stars in the bin of luminosity with respect to the total number of carbon stars. The observed LFCS consists of 111 objects, whose estimate of absolute luminosity can be obtained in two ways. Firstly, thanks to the use of Hipparcos parallaxes recently revised (van Leeuwen et al. 2007) and of IR data from the ISO and MSX missions or, secondly, from the period-Luminosity relation for Mira C-rich sources published in Whitelock et al. (2006) (see Guandalini et al. 2006 and Guandalini & Busso 2008 for the technical

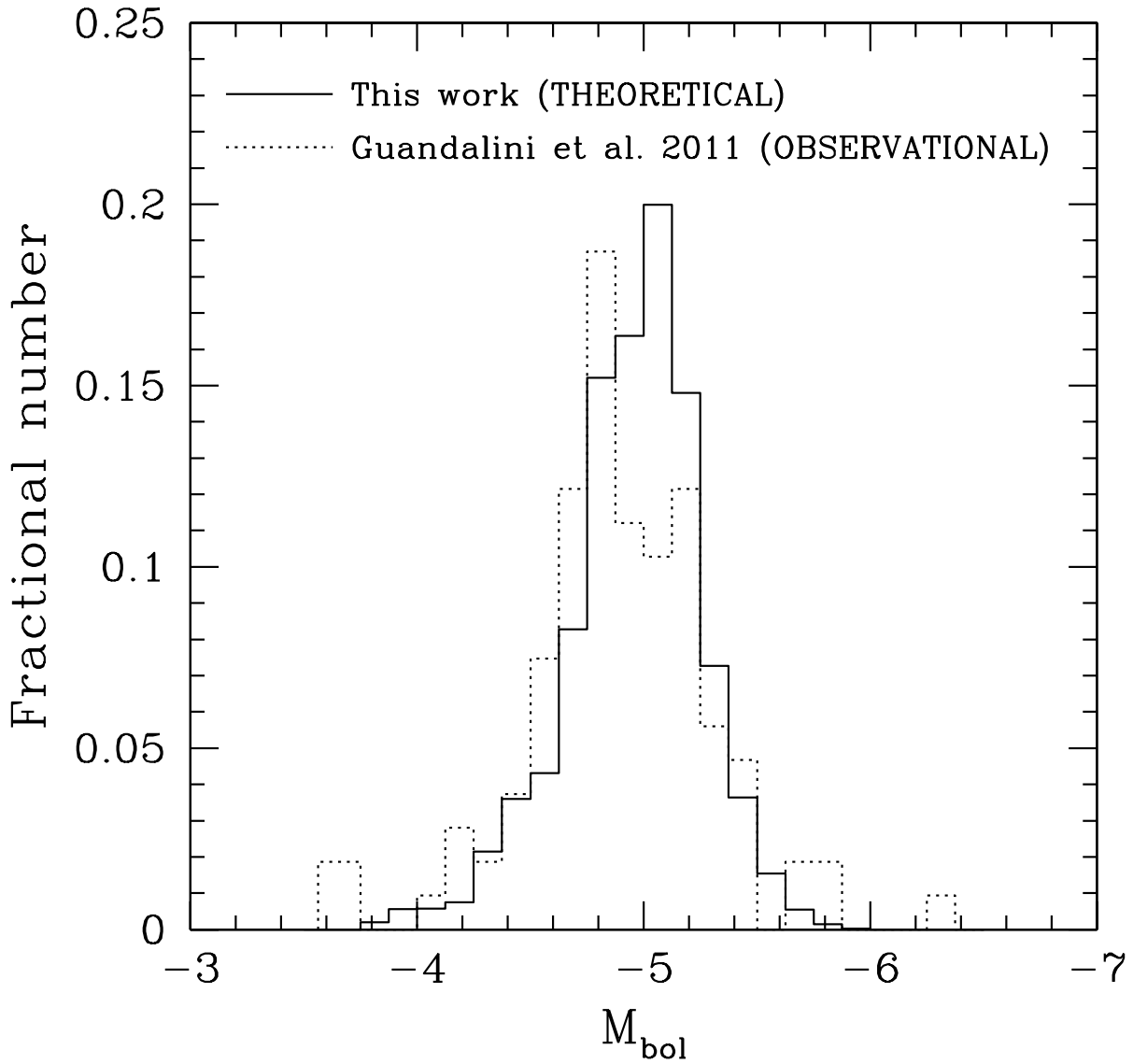


Fig. 9.— Theoretical (solid histogram) Luminosity Function of Galactic Carbon Stars compared with an upgrade of the observed one presented in Guandalini et al. 2006 (dotted histogram; *courtesy of R. Guandalini*).

procedure followed to construct the LFCS). The theoretical LFCS has been obtained by assuming that the current AGB population of the Galactic disk consists of stars born at different ages (and thus with different masses) and with different metallicities. We hypothesize that the disk formed 10 Gyr ago and, increasing the age with time steps of $10^5$ yr, we evaluate the number of AGB stars currently laying on their TP-AGB during each time step. We calculate the lower and upper mass on the AGB by interpolating the physical inputs (such as the main sequence lifetime, the AGB lifetime and the bolometric magnitudes along the AGB) on the grid of computed models. The upper mass has been fixed to 3.0 $M_\odot$, while the minimum mass depends on the metallicity. In order to cover the low mass tail of the LFCS, we calculate additional models with a restricted nuclear network. At high metallicity ($Z = 2 \times 10^{-2}$ and $Z = Z_\odot$) the minimum initial mass for a star to become carbon rich is 1.5 $M_\odot$, then decreases to 1.4 $M_\odot$ at $Z = 10^{-2}$, to 1.3 $M_\odot$ at $Z = 6 \times 10^{-3}$, to 1.2 $M_\odot$ at $Z = 3 \times 10^{-3}$ and, finally, to 1.1 $M_\odot$ at $Z = 10^{-3}$. We adopt a linear decreasing Star Formation Rate (SFR)[20] and the IMF proposed by Salpeter (1955). Moreover, we assume a theoretical flat metallicity distribution (see below).

Our curve matches the observed one, showing, within observational errors, the same peak around $M_{\rm bol} \sim -5.0$. Note that, unlike Stancliffe et al. (2005), we do not apply any normalization coefficient to match the peak of the corresponding observations. Moreover, we highlight that the choice of a different IMF, SFR or metallicity distribution, does lead to very similar results. In the upper panel of Fig.10 we report our standard luminosity function (solid curve), a test case with a Salpeter's IMF law with $\alpha$=1.35, a test case computed with a constant SFR over the whole Galaxy evolution (dotted curve) and a test with a metallicity distribution as derived from observations of local G-dwarfs (Dual Metallicity Distribution,

[20]We assume an initial amount of gas converted to stars of 8 $M_\odot$ per yr and then we apply a linear decrease down to a current value of 3 $M_\odot$ per yr.

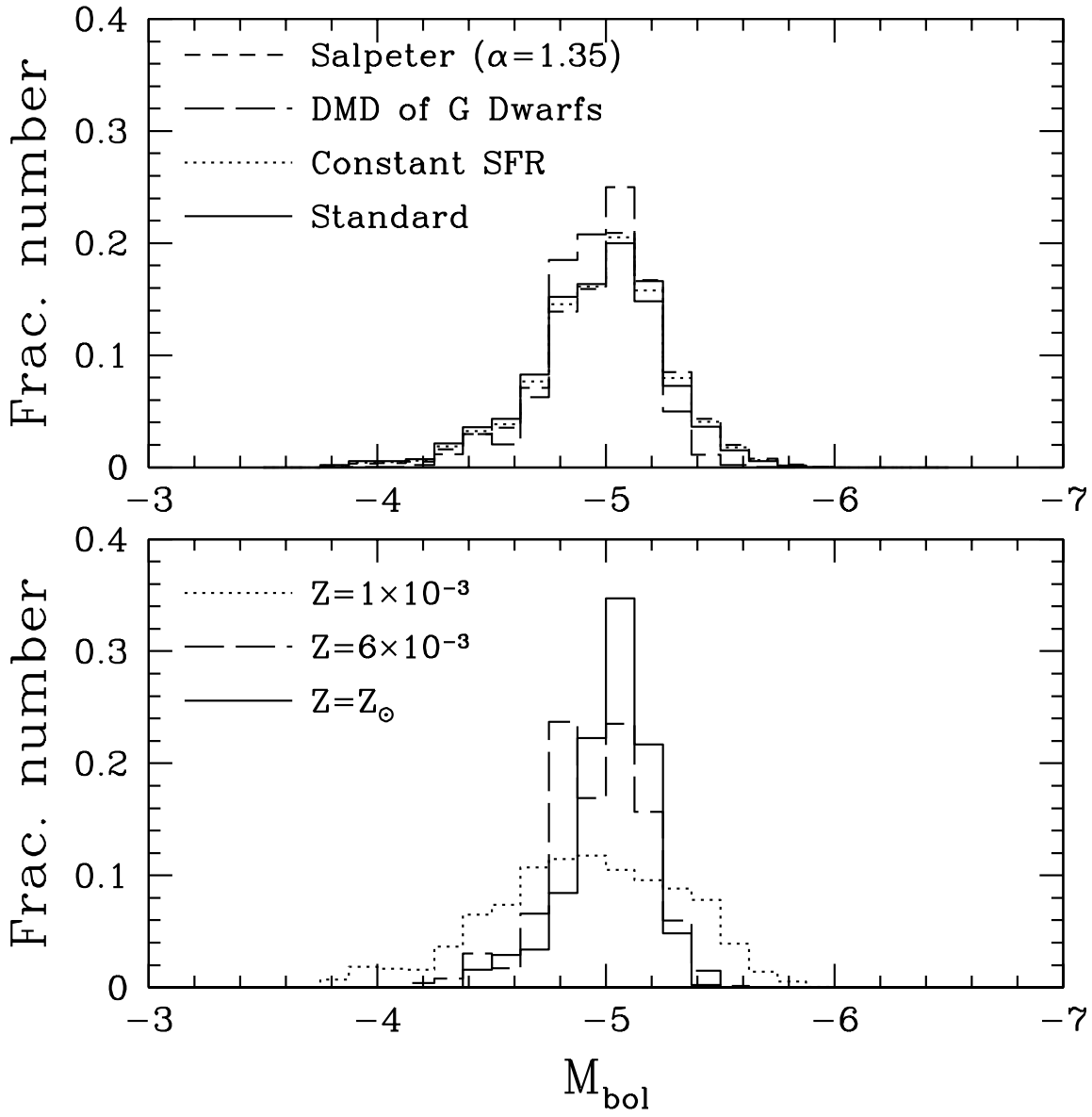


Fig. 10.— Upper Panel: theoretical Galactic LFCS calculated with different input parameters: Standard Case (solid curve), modified Salpeter's IMF (short-dashed curve), constant SFR (dotted curve) and metallicity distribution as observed in local G-Dwarfs (long-dashed curve). Lower Panel: LFCS for selected key metallicities: $Z = 1 \times 10^{-3}$ (dotted curve), $Z = 6 \times 10^{-3}$ (dashed curve) and $Z = Z_{\odot}$ (solid curve).

DMD; Rocha-Pinto & Maciel 1996). As already stated, the differences between different cases are negligible. Moreover, we evaluate the weight that each metallicity has on the final luminosity function. In the lower panel of Fig. 10 we plot some LFCS corresponding to selected key metallicities: $Z = 1 \times 10^{-3}$ (dotted curve), $Z = 6 \times 10^{-3}$ (dashed curve) and $Z = Z_{\odot}$ (solid curve). It emerges that larger is the metallicity, thinner is the LFCS, being the $M_{\rm bol}$ peak always around $-5.0$ . The flattest LFCS is obtained at $Z = 1 \times 10^{-3}$, due to the decrease of the stellar mass for the occurrence of TDU (which accounts for the faintest stars) and to the large increase of the final core masses for stars with initial masses $M \geq 2.5 M_{\odot}$ (which accounts for the brightest stars).

More stringent constraints would come from the comparison of theoretical LFCS with the ones derived in the Magellanic Clouds (MCs). This basically derives from a more precise determination of MCs distances with respect to Galactic carbon stars. Notwithstanding, we must remind that the photometric measurements of C-rich stars belonging to MCs are often incomplete, since they lack of the contribution from the thermal IR band ($\lambda > 2\mu m$). As a matter of fact, these objects emit the majority of their flux ($\sim$90%) at these wavelengths, while the most widely adopted data used to built up the LFCS were based on optical (visible or near-IR data) by Westerlund et al. (1986) and Rebeirot et al. (1993) for SMC, or Costa & Frogel (1996) for LMC. Recently, Zijlstra et al. (2006), Sloan et al. (2006), Groenewegen et al. (2007) and Lagadec et al. (2007) report the luminosities of a sample of about 60 C-stars belonging to MCs, as derived by combining ground-based observations in the near-IR (J,H,K and L) with *Spitzer Space Telescope* spectroscopic observations. In the upper panel of Fig. 11 we compare the LMC LFCS as reported by Groenewegen et al. (2007) (dotted curve) and Zijlstra et al. (2006) (dashed curve). Although the two observational works share the same data set, the resulting Luminosity Functions appear rather different. Nevertheless, they both peak at $\rm M_{bol} = -5$, thus in good agreement with our theoretical LFCS. This latter curve have been constructed by assuming a constant SFR

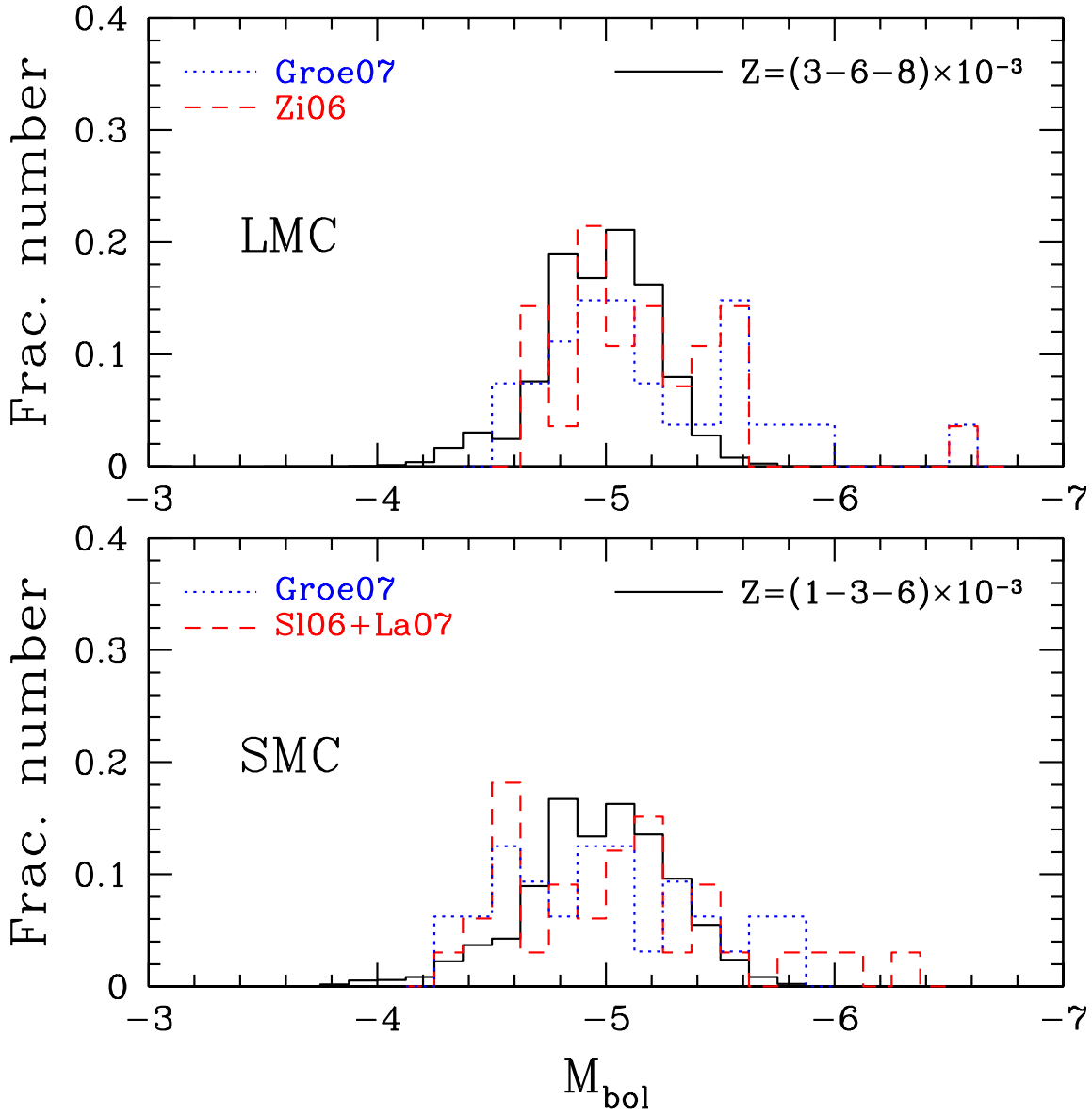


Fig. 11.— Upper Panel: theoretical and observational LFCS for the LMC system (Groe07: Groenewegen et al. 2007; Zi06: Zijlstra et al. 2006); Lower Panel: theoretical and observational LFCS for the SMC system (Sl06: Sloan et al. 2006; La07: Lagadec et al. 2007). See text for details.

and 3 equally weighted metallicities ($Z = 3 \times 10^{-3}$, $Z = 6 \times 10^{-3}$ and $Z = 8 \times 10^{-3}$). Similar conclusions can be drawn for SMC (see the lower panel of Fig. 11). In that case the observed distributions are from Groenewegen et al. (2007) (dotted curve) and a combined sample from Sloan et al. (2006) and Lagadec et al. (2007) (dashed curve). For SMC, the observational LFCS shows a larger spread, but the average $M_{bol}$ is similar to the LMC one. The lower SMC mean metallicity forces us to use models with different $Z$ to construct our theoretical LFCS ($Z = 1 \times 10^{-3}$, $Z = 3 \times 10^{-3}$ and $Z = 6 \times 10^{-3}$). As already explained, this makes our distribution flatter and, thus, in quite good agreement with observations. The statistical samples used for the observed CSLFs reported in Fig. 11 are quite poor, but we are confident that future developments of ground and space-based IR-facilities would greatly improve the observational constraints to AGB theoretical models.

### 6.2. *s*-process indexes

In this section we compare the predicted spectroscopic indexes [hs/ls] and [Pb/hs] to the observed composition of various *s*-enhanced stars. Among these stars, we should distinguish between AGB stars (*i.e.* those presently undergoing thermal pulses and TDU episodes), post-AGB stars and less-evolved stars (dwarfs or giants) belonging to binary systems. In the latter case, the *s*-enhancement is likely due to the pollution caused by the intense wind of an AGB companion (hereinafter extrinsic *s*-enhanced stars).
In principle, such a comparison requires the knowledge of the evolutionary status of the star, the initial mass and the metallicity. In the case of extrinsic *s*-enhanced stars, in addition to the initial masses and the metallicity of both the binary components, we should know the evolutionary status of the presently observed secondary star, its age at the epoch of the pollution and the total mass of chemically enriched material deposited on its surface (*Bisterzo et al., submitted*). Nevertheless, according to our low-mass-AGB models, the two

spectroscopic indexes [hs/ls] and [Pb/hs] should roughly attain the final value after a few third dredge-up episodes. In other words, if the *s*-process enhancement is sufficiently large, the knowledge of the precise evolutionary status is no longer a necessary condition. In practice, if the *s*-enhancement has been caused by the radiative $^{13}$C burning, as we have shown to occur in a low mass AGB stars, the [hs/ls] and the [Pb/hs] should only depend on the stellar metallicity and, eventually, on its mass.

In the following analysis we consider *s*-enhanced stars spectroscopically classified as: S stars (O-rich AGB stars), N type C stars (C-rich AGB stars) post-AGB (either O- and C-rich), Ba and/or CH stars (C-rich extrinsic *s*-enhanced stars). We also consider a few SC stars, even though their evolutionary status and origin are unknown. Then, in Fig. 12 we compare, as a function of the metallicity, our final surface [hs/ls] with the corresponding measured values, for a rather large sample of stars. In the caption we report the references corresponding to observational data. Although a similar trend with the metallicity may be recognized, the rather large spread of the observed [hs/ls] at any metallicity cannot be explained through a change of the stellar mass.

The comprehension of the origin of this spread is a hard task. Note that the typical error associated to the derivation of the heavy elements abundances for these *s*-enhanced stars is of the order of $\pm$0.1 dex, even if a more conservative evaluation might suggest up to $\pm$0.3 dex. Such an error, however, only takes into account the uncertainty introduced in the abundance analysis by the unknown stellar parameters (effective temperature, gravity, metallicity). The systematic uncertainty associated to the particular physical prescriptions used to model the stellar atmosphere, such as the deviations from the local thermodynamics equilibrium (LTE) or from the spherical symmetry (1D versus 3D models), is often neglected. As a matter of fact, the use of different procedures for the abundance analysis and/or model atmospheres might lead to different stellar parameters and, hence, to

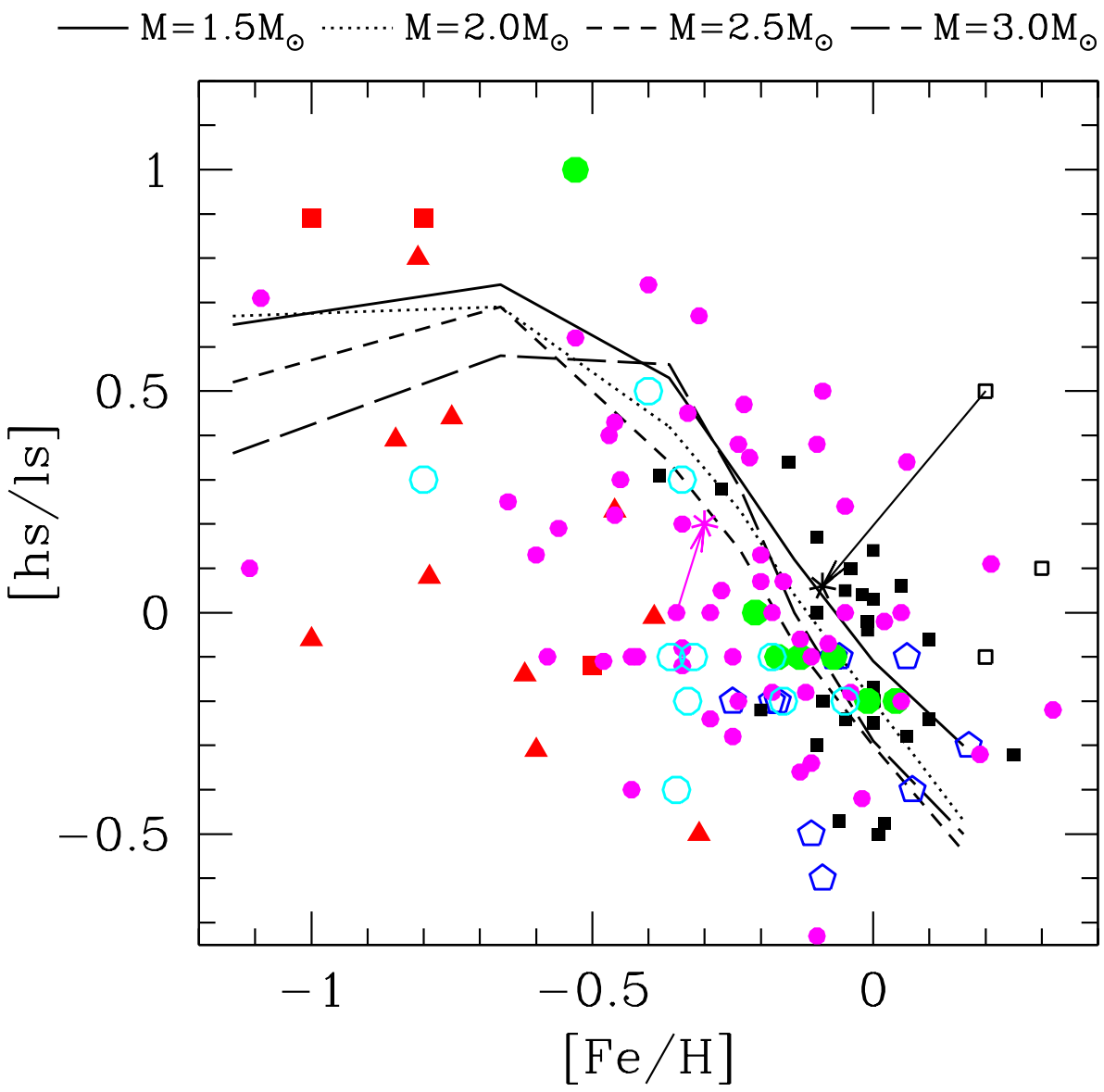


Fig. 12.— Our theoretical [hs/ls] curves compared with observational data. We report: intrinsic O-stars (open blue pentagon: Smith & Lambert 1985, 1986, 1990); intrinsic SC-stars (little open dark squares: Abia & Wallerstein 1998); intrinsic C-stars (little filled dark squares: Abia et al. 2002; Zamora et al. 2009); post-AGB stars (filled red triangles: van Winckel & Reyniers 2000; Reddy et al. 2002; Reyniers et al. 2004); extrinsic O-rich stars (large filled green circles: Smith & Lambert 1985, 1986, 1990), Ba-stars (little filled magenta circles: Smith 1984; Smith & Lambert 1984; Kovács 1995; Tomkin & Lambert 1986; Smith & Suntzeff 1987; Smith & Lambert 1990; Pereira et al. 1998; Allen & Barbuy 2006; Smiljanic et al. 2007; Liu et al. 2009); CH-stars (large open

different results. A couple of examples may illustrate this problem. We found at least two stars in our sample for which a revision of the abundance analysis is possible. The SC-type star RR Her was analyzed by Abia & Wallerstein (1998) by using atmosphere models from Alexander et al. (unpublished). For this star, they obtained [Fe/H]=0.2 and an [hs/ls]=0.5. Recently, Zamora (2009) reanalyzed this star by using the state-of-the-art of atmosphere models for C-stars (Gustafsson et al. 2008), together with updated molecular and atomic line lists. The new derived [Fe/H] is -0.09 and the [hs/ls] ratio is 0.06. As a result, the revised [hs/ls] nicely fits the theoretical prediction (see Fig. 12). Moreover, we were also able to re-analyze the Ba-star HR 107, previously studied by Allen & Barbuy (2006). We take advantage of a very high-resolution (R$\sim$ 200000) HARPS visual spectrum available in the ESO archive. Then, by adopting the same atmosphere parameters as in Allen & Barbuy (2006), we derive a [hs/ls]=0.2 to be compared with the [hs/ls]=0 obtained by the authors. A more detailed description of the tools used for the revised analysis may be found in Abia et al. (2002), de Laverny et al. (2006) and Zamora et al. (2009).

Lead measurements are also available for a sub-sample of the observed stars (Allen & Barbuy 2006). The comparison with the theoretical [Pb/hs] index is shown in Fig. 13. As for the [hs/ls] ratio, the general trend of the observed data appears in reasonable agreement with the theoretical expectations. Also in this case, however, the observed spread cannot be ascribed to a variation of the stellar mass within the range $1.5 - 3.0 M_{\odot}$. We have also revised the lead abundance of the Ba stars HR 107. From the HARPS high-resolution spectrum we have obtained an upper limit [Pb/hs]=0.05, which is definitely smaller than the 0.34 quoted by Allen & Barbuy (2006). This confirms the need of more accurate evaluation of the systematic uncertainties affecting the abundance analysis.

Although it is possible that the observed spread may be (totally or in part) ascribed

to a large observational uncertainty, we mention possible alternative theoretical scenarios, which may result in a certain spread of the spectroscopic indexes [hs/ls] and [Pb/hs]. As discussed in Section 3, these indexes basically depend on 3 quantities, namely: neutrons, poisons and seeds. A change of the amount of neutrons would imply a change of the (*effective*) $^{13}$C in the pocket. In the post-process calculations performed by Gallino et al. 1998 (see also Busso et al. 2001; Pignatari et al. 2004; Husti et al. 2008; Bisterzo et al. 2011), the amount of $^{13}$C within the pocket (and accordingly the amount of $^{14}$N) has been varied parametrically in order to match the observed chemical pattern. In this way, since the extension of the pocket and, in turn, the amount of Fe seeds are unchanged, the neutrons-to-seed ratio can be freely varied, in order to reproduce the observed spread of the spectroscopic indexes. Such a procedure is justified by the uncertain theoretical description of the hydrodynamical process which determines the proton profile in the transition zone between the fully-convective envelope and the radiative H-exhausted core during a TDU episode. As a matter of fact, in our model such a profile is the result of the assumed exponential decay of the average mixing velocity at the inner border of the convective envelope. A spread of such an average description may eventually imply a spread in the resulting profile. Note, however, that even a small variation (positive or negative) of the $\beta$ parameter determining the shape of the convective velocities within the convective-radiative transition region strongly depletes the resulting *s*-process nucleosynthesis, as demonstrated in Section 4 (see also Paper I). This would lead to definitely lower final surface heavy elements abundances, thus in contrast with observations. Moreover, the C-star luminosity function would be altered (see Section 6.1). Such an occurrence provides an independent check of the adopted parametrization. As we have already shown, the predicted and the observed LF of the Galactic C-stars are in good agreement.

Alternative scenarios may eventually account for the observed spread of the spectroscopic indexes, leaving the LFCS unchanged. Mixing induced by rotation has been

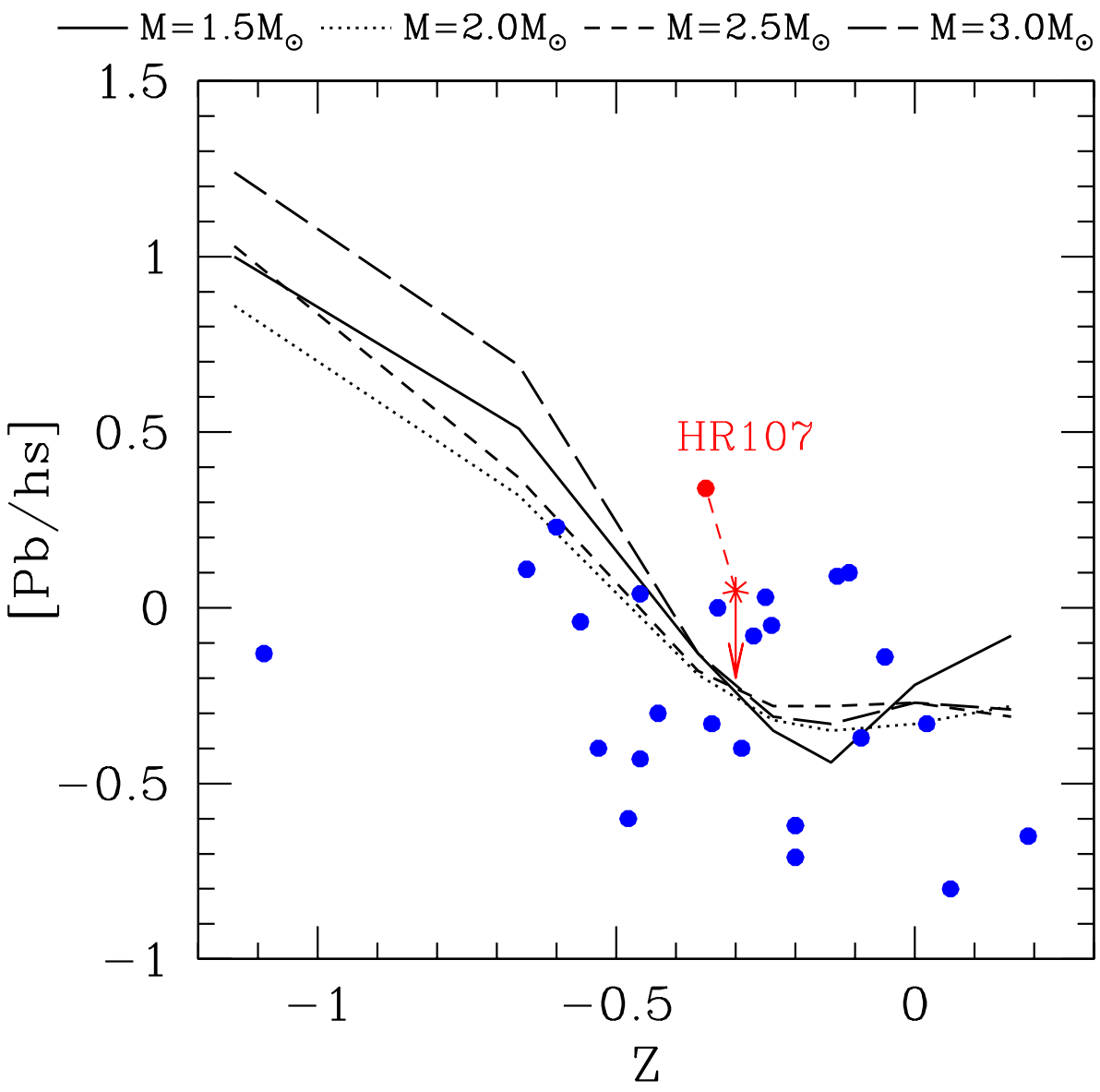


Fig. 13.— Theoretical [Pb/hs] curves compared with the same ratios as observed in a sample of Galactic barium stars (Allen & Barbuy 2006). The new upper limit derived for HR107 (this work) is also reported.

invoked to explain the formation of the $^{13}$C pocket (Langer et al. 1999). The common conclusion of all these attempts is that the resulting $^{13}$C pocket is too small for a sizeable *s*-process nucleosynthesis. This likely occurs because, during TDU episodes, the timescale for the formation of a proton profile (and the subsequent $^{13}$C pocket) in the upper layers of the He-intershell is too short compared to the timescale characterizing rotational-induced instabilities. Nevertheless, these instabilities might act during the longer time elapsed between the formation of the proton profile (maximum depth of the TDU) and the beginning of the *s*-process nucleosynthesis (Herwig et al. 2003; Siess et al. 2004). In low-mass AGB stars of nearly solar composition, such a period may be as long as a few $10^4$ yr. If enough total angular momentum is conserved at the beginning of the TP-AGB phase, the Eddington-Sweet instability, in particular, may have enough time to smear the $^{13}$C (and the $^{14}$N) pocket, thus reducing the local neutrons-to-seeds ratio. A quantitative analysis of this hypothesis is beyond the purpose of the present work and will be addressed in a forthcoming paper.

Finally, let us note that when the *s*-process nucleosynthesis takes place at the base of a quite extended convective zone, the seeds consumption is counterbalanced by the rapid mixing of fresh material from outside. On the contrary, due to the rapid destruction compared to the production, the amount of neutrons is maintained at a local equilibrium value, which depends on the temperature. As a result, a relatively low neutrons-to-seed ratio is maintained compared to the case of radiative burning, thus favoring the accumulation of light-*s* elements. In massive AGB stars, where the main neutron source is the $^{22}$Ne$(\alpha, n)^{25}$Mg reaction, which is active at the base of the convective shell, we expect an overproduction of ls. The case of the 3 $M_\odot$ model with $Z = 0.001$, where a substantial activation of the $^{22}$Ne convective burning is found, shows in fact a particularly low [hs/ls] compared to lower mass models with the same metallicity.

## 7. Conclusions

We presented FRUITY, an on-line database entirely dedicated to the nucleosynthesis occurring in AGB stars. Its interface is hosted on the web-pages of the Teramo Observatory (INAF-OACTe) and is accessible at the internet address http://www.oa-teramo.inaf.it/fruity. In this paper we discussed and analyzed the physical and chemical evolution of the first set of models included in the database, currently focused on low mass AGB stars ($1.5 \leq M/M_{\odot} \leq 3.0$) with metallicities in the range $1 \times 10^{-3} \leq Z \leq 2 \times 10^{-2}$. In the future, we intend to extend the grid of models by increasing the mass ($1.0 < M/M_{\odot} < 7.0$) and metallicity ($-3.2 <$ [Fe/H]$< -1.2$) ranges. Our calculations include a full nuclear network, from H to Bi, with 700 isotopes linked by more than 1000 nuclear processes. Thus, we followed in detail the nucleosynthesis of both light and heavy (*s*-process) elements. On the web interface, models selection can be operated choosing the desired mass ($M$) and metallicity ($Z$) values, while properties of nuclides (elements, isotopes, *s*-process spectroscopic indexes and yields) can be retrieved for all masses and atomic numbers or only for a sub-sample (selecting an appropriate pair of A/Z values). Moreover, the surface distributions after each TDU or just the final one can be selected for each model. Elemental abundances are given in the usual spectroscopic notation, while mass fractions are returned for the isotopes. Finally, net yields are given in solar mass units.

We analyzed the effects deriving from the activation of both the neutron sources in our low mass AGB models, the $^{13}$C($\alpha$,n)$^{16}$O and the $^{22}$Ne($\alpha$,n)$^{25}$Mg reactions, highlighting their contribution at different metallicities and for different initial masses. We evaluated the sensitivity of our model predictions to the adopted input parameters, with particular emphasis on the treatment of convection (the $\alpha$ parameter of the mixing length and the $\beta$ parameter determining the shape of the exponentially decreasing velocity profile at the

inner border of the convective envelope) and the mass loss law. We compared our model with the observational counterparts, from both a physical (luminosity function of carbon stars) and chemical (*s*-process spectroscopic indexes at different metallicities) point of view. Our theoretical luminosity function of carbon stars well fits the observational one, recently derived with the state-of-the-art set of distances (HIPPARCOS) and spectra (ISO). If recent SPITZER data are taken into account, a good agreement was also found for the Magellanic Clouds. In the future this comparison could be improved for the C-star population of nearby galaxies, as soon as a larger number of IR data is available. A comparison between our theoretical curves and spectroscopic data showed that, at fixed metallicity, our models cannot account for the *s*-process indexes spread identified by observations (in particular the [hs/ls] ratio). In the framework of our current modelling, we excluded that such a spread could be ascribed to the different initial masses of AGB models. We speculated on possible solutions from both an observational and theoretical point of view. In this latter case, we suggested that rotation may (at least partially) solve the current disagreement.

Part of this work was supported by the Spanish grants AYA2008-04211-C02-02 and FPA2008-03908 from the MEC and the Italian Grant FIRB 2008 "FUTURO IN RICERCA" C81J10000020001. We deeply thank R. Guandalini for providing unpublished data. We thank the anonymous referee for a detailed reading of this paper and for helpful comments and suggestions.

## REFERENCES

Abia, C., & Wallerstein, G., 1998, MNRAS, 293, 89

Abia, C., Busso, M., Gallino, R., Domínguez, I., Straniero, O., & Isern, J., 2001, ApJ, 559, 1117

Abia, C., et al., 2002, ApJ, 579, 817

Abia, C., de Laverny, P., & Wahlin, R., 2008, A&A, 481, 161

Abia, C., et al., 2010, ApJ, 715, 94

Abia, C., et al., 2011, ApJ, accepted (arXiv1107.1625A)

Allen, D., & Barbuy, B., 2006, A&A, 454, 917

Arlandini, C., Käppeler, F., Wisshak, K., Gallino, R., Lugaro, M., Busso, M., & Straniero, O., 1999, ApJ, 525, 886

Barzyk, J.G., et al., 2007, Meteoritics & Planetary Science, 42, 1103

Bisterzo, S., Gallino, R., Straniero, O., Cristallo, S., & Käppeler, F., 2010, MNRAS, 404, 1529

Bisterzo, S., Gallino, R., Straniero, O., Cristallo, S., & Käppeler, F., 2011, MNRAS, accepted

Busso, M., Gallino, R., Lambert, D.L., Travaglio, C., Smith, V.V., ApJ, 557, 802

Busso, M., et al., 2010, ApJ, 717, 47

Cameron, A.G.W., 1957, PASP, 69, 201

Cameron, A.G.W., 1960, AJ, 65, 485

Campbell, S.W., & Lattanzio, J.C., 2008, A&A, 490, 769

Charbonnel, C., Zahn, J.-P., 2007, A&A, 467, L15

Chieffi, A., Limongi, M., & Straniero, O., 1998, ApJ, 502, 737

Costa, E., & Frogel, J.A., 1996, AJ, 112, 2607

Cosner, K., Iben, I.,Jr., & Truran, J.W., 1980, ApJ, 283, L91

Cristallo, S., Straniero, O., Lederer, M.T., & Aringer, B., 2007, ApJ, 667, 489

Cristallo, S., Straniero, O., Gallino, R., Piersanti, L., Domínguez, I., & Lederer, M.T., 2009, ApJ, 696, 797 (Paper I)

Davis, A.M., Gallino, R., Cristallo, S., Straniero, O., 2009, M&PSA, 72, 5402

de Laverny, P., et al., 2006, A&A, 446, 1107

Denissenkov, P.A., Pinsonneault, M., & MacGregor, K.B., 2009, ApJ, 696, 1823

Denissenkov, P., 2010, ApJ, 723, 563

Denissenkov, P., Pavel, A., Merryfield, W.J., 2011, ApJ, 727, 8L

Domínguez, I., Chieffi., A., Limongi, M., & Straniero, O., 1999, ApJ, 524, 226

Eggleton, P.P, Dearborn, D.S.P., & Lattanzio, J.C., 2008, ApJ, 677, 581

Forestini, M., Goriely, S., Jorissen, A., & Arnould, M., 1992, A&A, 261, 157

Forestini, M., & Charbonnel, C., 1997, A&AS, 123, 241

Gallino, R., et al., 1998, ApJ, 497, 388

Goriely, S. & Siess, L., 2004, 421, L25

Groenewegen, M.A.T., & De Jong, T., 1994, A&A, 283, 463

Groenewegen, M.A.T., 1998, Ap&SS, 255, 379

Groenewegen, M.A.T., et al., 2007, MNRAS, 376, 313

Guandalini, R., Busso, M., Ciprini, S., Silvestro, G., & Persi, P., 2006, A&A, 445, 1069

Guandalini, R., & Busso, M., 2008, A&A, 488, 675

Gustafsson, B., Edvardsson, B., Eriksson, K., Jørgensen, U. G., Nordlund, Å., Plez, B., 2008, A&A, 486, 951

Herwig, F. , 2000, A&A, 360, 952

Herwig, F., Langer, N., & Lugaro, M., 2003, ApJ, 593, 1056

Herwig, F., 2004, ApJS, 155, 651

Herwig, F., & Austin, S.M., 2004, ApJ, 613, L73

Herwig, F., 2005, ARA&A, 43, 435

Hoppe, P., et al., 1997, ApJ, 487, 101

Husti, L., Gallino, R., Straniero, O., & Cristallo, S., 2009, PASA, 26, 176

Iben, I.Jr., 1973, ApJ, 185, 209

Iben, I.Jr., 1981, ApJ, 246, 278

Iben, I.Jr., & Renzini, A., 1983, ARA&A, 21, 271

Izzard, G.I., Tout, C.A., Karakas, A.I., & Pols, O.R., 2006, MNRAS, 350, 407

Jorissen, A., Smith, V.V., & Lambert, D.L., 1992, A&A, 261, 164

Karakas, A.I., 2003, Ph.D. Thesis, Monash University, Australia

Karakas, A.I., Lugaro, M.A., Wiescher, M., Görres, J., Ugalde, C., ApJ, 643, 471

Karakas, A., & Lattanzio, J.C., 2007, PASA, 24, 103

Karakas, A.I., 2010, MNRAS, 403, 1413

Kobayashi, C., Karakas, A.I., & Umeda, H., 2011, MNRAS, 414, 3231

Kovács, R.L., 1985, A&A, 150, 232

Lagadec, E., et al., 2007, MNRAS, 376, 1270

Lambert, D.L., Smith, V.V., Busso, M., Gallino, R., & Straniero, O., 1995, ApJ, 450, 302

Langer, N., Heger, A., Wellstein, S., & Herwig, F., 1999, A&A, 346, 37L

Lattanzio, J.C., 1989, ApJ, 344, 25L

Lau, H.H.B., Stancliffe, R.J., & Tout, C.A., 2009, MNRAS, 396, 1046

Lebzelter, T., Lederer, M. T., Cristallo, S., Hinkle, K. H., Straniero, O., & Aringer, B., 2008, A&A, 486, 511

Lederer, M.T., & Aringer, B., 2009, A&A, 494, 403

Lederer, M.T., Lebzelter, T., Cristallo, S., Straniero, O., Hinkle, K.H., & Aringer, B., 2009, A&A, 502, 913

Liu, G., Liang, Y., & Deng, L., 2009, Res. Astronom. Astrophys., 9, 431

Lodders, K., 2003, ApJ, 591, 1220

Lugaro, M., Zinner, E., Gallino, R., & Amari, S., 1999, ApJ, 527, 369L

Lugaro, M., Herwig, F., Lattanzio, J.C., Gallino, R., Straniero, O., 2003, ApJ, 586, 1305

Lugaro, M., Ugalde, C., Karakas, A., Görres, J., Wiescher, M., Lattanzio, J.C., & Cannon, R.C., 2004, ApJ, 615, 934

Marigo, P., 2001, A&A, 370, 194

Marigo, P., 2002, A&A, 387, 507

Marigo, P., & Girardi, L., 2007, A&A, 469, 239

Milingo, J.B., Kwitter, K.B., Henry, R.B.C., Souza, S.P., 2009, ApJ, 711, 619

Mowlavi, N., Jorissen, A., & Arnould, M., 1996, A&A, 311, 803

Mowlavi, N., 1999, A&A, 350, 73

Nordhaus, J., Busso, M., Wasserburg, G.J., Blackman, E.G., Palmerini, S., 2008, ApJ, 684, 29L

Palmerini, S., La Cognata, M., Cristallo, S., Busso, M., 2011, ApJ, 729, 3

Pereira, C.B., Smith, V.V., & Kunha, K., 1998, AJ, 116, 1977

Pereira, C.B., & Drake, N.A., 2011, AJ, 141, 79

Piersanti, L., Straniero, O., & Cristallo, S., 2007, A&A, 462, 1051

Pignatari, M., Gallino, R., Cristallo, S., & Straniero, O., 2008, AIP Conf. Proceedings, 1001, 154

Rebeirot, E., Azzopardi, M., & Westerlund, B.E., 1993, A&AS, 97, 603

Reddy, B., Lambert, D., Gonzalez, G., & Yong, D., 2002, ApJ, 564, 482

Reyniers, M., van Winckel, H., Gallino, R., & Straniero, O., 2004, A&A, 417, 269

Rocha-Pinto, H.J., & Maciel, W.J., 1996, MNRAS, 279, 447

Roederer, I.U., Marino, A.F., & Sneden, C., 2011, ApJ, in press (2011arXiv1108.3868R)

Romano, D., Karakas, A., Tosi, M., & Matteucci, F., 2010, A&A, 522, 32

Salpeter, E., 1955, ApJ, 121, 161

Sharpee, B., et al., 2007, ApJ, 659, 1265

Siess, L., Goriely, S., & Langer, N., 2004, A&A, 415, 1089

Sloan, G.C., Kraemer, K.E., Matsuura, M., Wood, P.R., Price, S.D., Egan, M.P., 2006, ApJ, 645, 1118

Smiljanic, R., Porto de Mello, G., & da Silva, L., 2007, A&A, 468, 679

Smith, V.V., 1984, A&A, 132, 326

Smith, V.V., & Lambert, D.L., 1984, PASP, 96, 226

Smith, V.V., & Lambert, D.L., 1985, ApJ, 294, 326

Smith, V.V., & Lambert, D.L., 1986, ApJ, 311, 843

Smith, V.V., & Suntzeff, 1987, AJ, 93, 359

Smith, V.V., & Lambert, D.L., 1990, ApJS, 72, 387

Smith, V.V., Coleman, H., & Lambert, D.L., 1993, ApJ, 417, 287

Stancliffe, R.J., Tout, C.A., & Pols, R.O., 2004, MNRAS, 352, 984

Stancliffe, R.J., Izzard, R.G., & Tout, C.A., 2005, MNRAS, 356, L1

Sterling, N.C., Dinerstein, H.L., 2008, ApJS, 174, 158

Straniero, O., Gallino, R., Busso, M., Chieffi, A., Limongi, M., & Salaris, M., 1995, ApJ, 440, L85

Straniero, O., Chieffi, A., Limongi, M., Gallino, R., Busso, M., & Arlandini, C., 1997, ApJ, 478, 332

Straniero, O., Limongi, M., Chieffi, A., Domínguez, I., Busso, M., & Gallino, R., 2000, Mem. Soc. Astron. Italiana, 71, 719

Straniero, O., Domínguez, I., Cristallo, S., & Gallino, R., 2003, PASA, 20, 389

Straniero, O., Domínguez, I., Imbriani, G., & Piersanti, L., 2003, ApJ, 583, 878

Straniero, O., Gallino, R., & Cristallo, S., 2006, Nucl. Phys. A, 777, 311

Sugimoto, D., 1971, Prog. Theor. Phys., 45, 761

Tomkin, J. & Lambert, D.L., ApJ, 311, 819

Travaglio, C., Galli, D., Gallino, R., Busso, M., Ferrini, F., & Straniero, O., 1999, ApJ, 521, 691

Truran, J.W. & Iben, I.,Jr., 1977, ApJ, 216, 797

van Leeuwen, F., Feast, M.W., Whitelock, P.A., Laney, C.D., 2007, MNRAS, 379, 723

Vanture, A.D., 1992, AJ, 107, 1997

van Winckel, H., & Reyniers, M., 2000, A&A, 354, 135

Ventura, P., & D'Antona, F., 2005, A&A, 431, 279

Ventura, P., & Marigo, P., 2009, MNRAS, 339, 54

Weiss, A., & Ferguson, J.W., 2009, A&A, 508, 1343

Werner, K., & Herwig, F., 2006, PASP, 118, 183

Werner, K., Rauch, T., Reiff, E., & Kruk, J.W., 2009, Ap&SS, 320, 159

Westerlund, B.E., Azzopardi, M., & Breysacher, J., 1986, A&AS, 97, 603

Whitelock, P.A., Feast, M.W., Marang, F., & Groenewegen, M.A.T., 2006, MNRAS, 369, 751

Začs, L., Schmidt, M.R., & Schuster, W.J., 2000, A&A, 358, 1022

Zamora, O., 2009, PASP, 121, 558

Zamora, O., Abia, C., Plez, B., Domínguez, I., & Cristallo, S., 2009, A&A, 508, 909

Zijlstra, A.A., et al., 2006, MNRAS, 370, 1961

Zinner, E., Nittler, L.R., Gallino, R., Karakas, A.I., Lugaro, M., Straniero, O., & Lattanzio, J.C., 2006, ApJ, 650, 350

Table 1. The C-enhancement factors for the H-rich opacity tables at various metallicities, defined as the ratio between the $^{12}$C abundance used to calculate the opacity table and the initial $^{12}$C.

| $Z$ | [Fe/H] | enhancement factor ($f_i$) | | | | |
|---|---|---|---|---|---|---|
| | | $f_1$ | $f_2$ | $f_3$ | $f_4$ | $f_5$ |
| 0.020 | 0.16 | 1 | 1.5 | 1.8 | 2.2 | 5 |
| 0.014 | 0 | 1 | 1.5 | 1.8 | 2.2 | 4 |
| 0.010 | -0.14 | 1 | 1.8 | 2.2 | 5 | 10 |
| 0.008 | -0.24 | 1 | 1.8 | 2.2 | 5 | 10 |
| 0.006 | -0.36 | 1 | 2 | 5 | 10 | 50 |
| 0.003 | -0.66 | 1 | 2 | 5 | 10 | 50 |
| 0.001 | -1.14 | 1 | 5 | 10 | 50 | 200 |

Table 2. Fundamental properties of the pre-AGB phase.

| $M$ ($M_\odot$) | $\Delta t_{\rm H}$ (Myr) | $M_{\rm H}^{cc}$ ($M_\odot$) | $\rm He_{\it surf}^{\it FDU}$ | log $L_{tip}^{RGB}$ | $M_{\rm He}^{1}$ ($M_\odot$) | $\Delta t_{\rm He}$ (Myr) | $M_{\rm He}^{2}$ ($M_\odot$) | $M_{\rm He}^{3}$ ($M_\odot$) |
|---|---|---|---|---|---|---|---|---|
| | | | | | | | | |
| | | | | $Z$=**0.02** $Y$=**0.269** | | | | |
| 1.5 | 2839 | 0.122 | 0.289 | 3.428 | 0.480 | 116 | 0.525 | 0.547 |
| 2.0 | 1159 | 0.270 | 0.280 | 3.376 | 0.471 | 122 | 0.527 | 0.549 |
| 2.5 | 592 | 0.444 | 0.282 | 2.421 | 0.314 | 302 | 0.489 | 0.523 |
| 3.0 | 346 | 0.594 | 0.285 | 2.497 | 0.369 | 168 | 0.536 | 0.555 |
| | | | | $Z$=**0.014** $Y$=**0.269** | | | | |
| 1.5 | 2310 | 0.131 | 0.286 | 3.421 | 0.481 | 109 | 0.531 | 0.550 |
| 2.0 | 970 | 0.293 | 0.280 | 3.333 | 0.465 | 119 | 0.531 | 0.548 |
| 2.5 | 503 | 0.469 | 0.282 | 2.448 | 0.315 | 259 | 0.506 | 0.530 |
| 3.0 | 299 | 0.628 | 0.285 | 2.523 | 0.375 | 138 | 0.562 | 0.581 |

Table 2—Continued

| $M$ ($M_\odot$) | $\Delta t_{\rm H}$ (Myr) | $M_{\rm H}^{cc}$ ($M_\odot$) | $\rm He_{\it surf}^{\it FDU}$ | log $L_{tip}^{RGB}$ | $M_{\rm He}^{1}$ ($M_\odot$) | $\Delta t_{\rm He}$ (Myr) | $M_{\rm He}^{2}$ ($M_\odot$) | $M_{\rm He}^{3}$ ($M_\odot$) |
|---|---|---|---|---|---|---|---|---|
| | | | $Z$=**0.01** $Y$=**0.265** | | | | | |
| 1.5 | 2162 | 0.136 | 0.284 | 3.412 | 0.483 | 105 | 0.532 | 0.549 |
| 2.0 | 913 | 0.301 | 0.277 | 3.322 | 0.466 | 117 | 0.531 | 0.551 |
| 2.5 | 479 | 0.496 | 0.279 | 2.443 | 0.317 | 242 | 0.506 | 0.530 |
| 3.0 | 288 | 0.646 | 0.281 | 2.523 | 0.378 | 125 | 0.577 | 0.597 |
| | | | $Z$=**0.008** $Y$=**0.265** | | | | | |
| 1.5 | 1983 | 0.141 | 0.284 | 3.403 | 0.483 | 103 | 0.535 | 0.552 |
| 2.0 | 845 | 0.310 | 0.277 | 3.291 | 0.463 | 116 | 0.533 | 0.551 |
| 2.5 | 447 | 0.483 | 0.279 | 2.431 | 0.319 | 218 | 0.517 | 0.538 |
| 3.0 | 271 | 0.663 | 0.280 | 2.527 | 0.382 | 110 | 0.607 | 0.622 |
| | | | $Z$=**0.006** $Y$=**0.260** | | | | | |

Table 2—Continued

| $M$ ($M_\odot$) | $\Delta t_{\rm H}$ (Myr) | $M_{\rm H}^{cc}$ ($M_\odot$) | $\rm He_{\it surf}^{\it FDU}$ | log $L_{tip}^{RGB}$ | $M_{\rm He}^{1}$ ($M_\odot$) | $\Delta t_{\rm He}$ (Myr) | $M_{\rm He}^{2}$ ($M_\odot$) | $M_{\rm He}^{3}$ ($M_\odot$) |
|---|---|---|---|---|---|---|---|---|
| | | | | | | | | |
| 1.5 | 1851 | 0.147 | 0.280 | 3.392 | 0.484 | 100 | 0.537 | 0.556 |
| 2.0 | 810 | 0.327 | 0.273 | 3.268 | 0.462 | 114 | 0.539 | 0.555 |
| 2.5 | 430 | 0.496 | 0.274 | 2.419 | 0.317 | 199 | 0.531 | 0.549 |
| 3.0 | 264 | 0.664 | 0.273 | 2.524 | 0.383 | 97.5 | 0.642 | 0.656 |
| | | | | $Z$=**0.003** $Y$=**0.260** | | | | |
| 1.5 | 1607 | 0.169 | 0.280 | 3.358 | 0.484 | 95.7 | 0.545 | 0.562 |
| 2.0 | 712 | 0.336 | 0.274 | 3.176 | 0.451 | 114 | 0.550 | 0.569 |
| 2.5 | 382 | 0.509 | 0.273 | 2.392 | 0.324 | 151 | 0.595 | 0.613 |
| 3.0 | 238 | 0.702 | 0.266 | 2.515 | 0.383 | 79.6 | 0.717 | 0.724 |
| | | | | $Z$=**0.001** $Y$=**0.245** | | | | |

Table 2—Continued

| $M$ ($M_\odot$) | $\Delta t_{\rm H}$ (Myr) | $M_{\rm H}^{cc}$ ($M_\odot$) | $\rm He_{\it surf}^{\it FDU}$ | log $L_{tip}^{RGB}$ | $M_{\rm He}^{1}$ ($M_\odot$) | $\Delta t_{\rm He}$ (Myr) | $M_{\rm He}^{2}$ ($M_\odot$) | $M_{\rm He}^{3}$ ($M_\odot$) |
|---|---|---|---|---|---|---|---|---|
| 1.5 | 1551 | 0.189 | 0.268 | 3.292 | 0.484 | 91.0 | 0.553 | 0.574 |
| 2.0 | 679 | 0.365 | 0.263 | 3.108 | 0.452 | 102 | 0.588 | 0.598 |
| 2.5 | 373 | 0.538 | 0.255 | 2.315 | 0.329 | 124 | 0.660 | 0.669 |
| 3.0 | 236 | 0.741 | 0.247 | 2.464 | 0.397 | 70.1 | 0.775 | 0.779 |

Table 3. Evolution of selected physical parameters of the models at $Z = 2 \times 10^{-2}$.

| $n^a_{\rm TP}$ | $M^b_{\rm Tot}$ | $M^b_{\rm H}$ | $\Delta M^b_{\rm TDU}$ | $\Delta M^b_{\rm CZ}$ | $\Delta M^b_{\rm H}$ | $r$ | $\lambda$ | $\Delta t^c_{ip}$ | $T^d_{MAX}$ | $\rm Z_{surf}$ | $\rm C/O_{surf}$ | $n_c$ |
|---|---|---|---|---|---|---|---|---|---|---|---|---|
| | | | | | | $M$=**1.5** $M_\odot$ | | | | | | |
| -4 | 1.32 | 0.542 | 0.00E+00 | 3.14E-02 | 2.20E-03 | 9.92E-01 | 0.00E+00 | 11.3 | 2.06 | 2.02E-02 | 0.34 | ··· |
| -3$^{(*)}$ | 1.31 | 0.547 | 0.00E+00 | 3.22E-02 | 4.40E-03 | 9.04E-01 | 0.00E+00 | 15.5 | 2.24 | 2.02E-02 | 0.34 | ··· |
| -2 | 1.30 | 0.552 | 0.00E+00 | 3.11E-02 | 5.60E-03 | 8.54E-01 | 0.00E+00 | 17.1 | 2.34 | 2.02E-02 | 0.34 | ··· |
| -1 | 1.28 | 0.559 | 0.00E+00 | 3.04E-02 | 6.80E-03 | 8.02E-01 | 0.00E+00 | 17.6 | 2.45 | 2.02E-02 | 0.34 | ··· |
| 1 | 1.26 | 0.566 | 6.00E-04 | 2.89E-02 | 7.10E-03 | 7.65E-01 | 8.45E-02 | 17.1 | 2.52 | 2.03E-02 | 0.36 | 5 |
| 2 | 1.23 | 0.574 | 1.30E-03 | 2.75E-02 | 8.20E-03 | 7.11E-01 | 1.59E-01 | 16.2 | 2.58 | 2.07E-02 | 0.42 | 27 |
| 3 | 1.20 | 0.581 | 2.00E-03 | 2.62E-02 | 8.80E-03 | 6.75E-01 | 2.27E-01 | 15.2 | 2.64 | 2.14E-02 | 0.53 | 34 |
| 4 | 1.16 | 0.588 | 2.30E-03 | 2.49E-02 | 9.20E-03 | 6.42E-01 | 2.50E-01 | 14.1 | 2.68 | 2.20E-02 | 0.67 | 36 |
| 5 | 1.10 | 0.595 | 7.00E-04 | 2.36E-02 | 9.20E-03 | 6.20E-01 | 7.61E-02 | 13.0 | 2.72 | 2.28E-02 | 0.71 | 28 |
| | $M^{\rm Tot}_{\rm TDU}$ = **6.90E-03** $M_\odot$ | | | | | | | $\tau_C$ = **0 yr** | | | | |

Table 3—Continued

| $n^a_{\rm TP}$ | $M^b_{\rm Tot}$ | $M^b_{\rm H}$ | $\Delta M^b_{\rm TDU}$ | $\Delta M^b_{\rm CZ}$ | $\Delta M^b_{\rm H}$ | $r$ | $\lambda$ | $\Delta t^c_{ip}$ | $T^d_{MAX}$ | $\rm Z_{surf}$ | $\rm C/O_{surf}$ | $n_c$ |
|---|---|---|---|---|---|---|---|---|---|---|---|---|
| | | | | | $M$=**2.0** $M_\odot$ | | | | | | | |
| -3 | 1.89 | 0.543 | 0.00E+00 | 3.18E-02 | 3.10E-03 | 9.31E-01 | 0.00E+00 | 12.5 | 2.12 | 2.02E-02 | 0.31 | ··· |
| -2$^{(*)}$ | 1.89 | 0.549 | 0.00E+00 | 3.18E-02 | 5.40E-03 | 8.66E-01 | 0.00E+00 | 16.1 | 2.26 | 2.02E-02 | 0.31 | ··· |
| -1 | 1.88 | 0.555 | 0.00E+00 | 3.12E-02 | 6.20E-03 | 8.30E-01 | 0.00E+00 | 18.0 | 2.39 | 2.02E-02 | 0.31 | ··· |
| 1 | 1.86 | 0.562 | 8.00E-04 | 3.00E-02 | 6.80E-03 | 7.85E-01 | 1.18E-01 | 18.1 | 2.48 | 2.03E-02 | 0.32 | 17 |
| 2 | 1.85 | 0.569 | 1.70E-03 | 2.87E-02 | 8.30E-03 | 7.21E-01 | 2.05E-01 | 17.5 | 2.56 | 2.06E-02 | 0.37 | 33 |
| 3 | 1.83 | 0.577 | 3.10E-03 | 2.75E-02 | 9.10E-03 | 6.82E-01 | 3.41E-01 | 16.8 | 2.63 | 2.12E-02 | 0.45 | 36 |
| 4 | 1.80 | 0.583 | 4.00E-03 | 2.65E-02 | 1.00E-02 | 6.32E-01 | 4.00E-01 | 16.1 | 2.70 | 2.20E-02 | 0.57 | 31 |
| 5 | 1.76 | 0.590 | 4.60E-03 | 2.55E-02 | 1.05E-02 | 5.94E-01 | 4.38E-01 | 15.4 | 2.75 | 2.30E-02 | 0.70 | 29 |
| 6 | 1.70 | 0.596 | 4.90E-03 | 2.44E-02 | 1.08E-02 | 5.69E-01 | 4.54E-01 | 14.5 | 2.79 | 2.41E-02 | 0.84 | 29 |
| 7 | 1.61 | 0.602 | 4.90E-03 | 2.33E-02 | 1.08E-02 | 5.44E-01 | 4.54E-01 | 13.5 | 2.83 | 2.51E-02 | 0.99 | 28 |
| 8 | 1.49 | 0.608 | 4.70E-03 | 2.22E-02 | 1.07E-02 | 5.25E-01 | 4.39E-01 | 12.4 | 2.85 | 2.63E-02 | 1.15 | 26 |
| 9 | 1.34 | 0.614 | 4.50E-03 | 2.11E-02 | 1.04E-02 | 5.17E-01 | 4.33E-01 | 11.4 | 2.87 | 2.76E-02 | 1.33 | 20 |
| 10 | 1.17 | 0.619 | 1.15E-03 | 2.00E-02 | 9.60E-03 | 5.14E-01 | 1.20E-01 | 10.2 | 2.88 | 2.76E-02 | 1.33 | 19 |

Table 3—Continued

| $n^a_{\rm TP}$ | $M^b_{\rm Tot}$ | $M^b_{\rm H}$ | $\Delta M^b_{\rm TDU}$ | $\Delta M^b_{\rm CZ}$ | $\Delta M^b_{\rm H}$ | $r$ | $\lambda$ | $\Delta t^c_{ip}$ | $T^d_{MAX}$ | $Z_{surf}$ | $C/O_{\rm surf}$ | $n_c$ |
|---|---|---|---|---|---|---|---|---|---|---|---|---|
| | $M^{\rm Tot}_{\rm TDU}$ = **3.44E-02** $M_\odot$ | | | | | | $\tau_C$ = **3.39E+05 yr** | | | | | |
| | | | | | $M$=**2.5** $M_\odot$ | | | | | | | |
| -1$^{(*)}$ | 2.47 | 0.523 | 0.00E+00 | 3.76E-02 | 6.70E-03 | 8.52E-01 | 0.00E+00 | 23.0 | 2.25 | 2.02E-02 | 0.31 | ··· |
| 1 | 2.46 | 0.531 | 8.00E-04 | 3.70E-02 | 7.30E-03 | 7.50E-01 | 8.16E-02 | 36.1 | 2.42 | 2.04E-02 | 0.34 | 5 |
| 2 | 2.45 | 0.540 | 1.50E-03 | 3.39E-02 | 9.00E-03 | 7.48E-01 | 2.05E-01 | 25.8 | 2.44 | 2.05E-02 | 0.36 | 16 |
| 3 | 2.44 | 0.548 | 2.80E-03 | 3.27E-02 | 9.30E-03 | 7.29E-01 | 3.01E-01 | 23.4 | 2.52 | 2.08E-02 | 0.40 | 30 |
| 4 | 2.43 | 0.555 | 4.00E-03 | 3.15E-02 | 1.01E-02 | 6.91E-01 | 3.96E-01 | 21.9 | 2.59 | 2.13E-02 | 0.48 | 35 |
| 5 | 2.41 | 0.562 | 5.20E-03 | 3.04E-02 | 1.09E-02 | 6.53E-01 | 4.77E-01 | 20.7 | 2.65 | 2.20E-02 | 0.57 | 30 |
| 6 | 2.39 | 0.568 | 6.00E-03 | 2.94E-02 | 1.16E-02 | 6.15E-01 | 5.17E-01 | 19.7 | 2.70 | 2.28E-02 | 0.68 | 27 |
| 7 | 2.37 | 0.574 | 6.60E-03 | 2.84E-02 | 1.21E-02 | 5.86E-01 | 5.45E-01 | 18.6 | 2.75 | 2.37E-02 | 0.80 | 26 |
| 8 | 2.34 | 0.580 | 6.70E-03 | 2.73E-02 | 1.23E-02 | 5.61E-01 | 5.45E-01 | 17.5 | 2.78 | 2.45E-02 | 0.91 | 24 |
| 9 | 2.30 | 0.585 | 6.50E-03 | 2.61E-02 | 1.22E-02 | 5.43E-01 | 5.33E-01 | 16.3 | 2.81 | 2.53E-02 | 1.02 | 23 |

Table 3—Continued

| $n^a_{\rm TP}$ | $M^b_{\rm Tot}$ | $M^b_{\rm H}$ | $\Delta M^b_{\rm TDU}$ | $\Delta M^b_{\rm CZ}$ | $\Delta M^b_{\rm H}$ | $r$ | $\lambda$ | $\Delta t^c_{ip}$ | $T^d_{MAX}$ | $Z_{surf}$ | C/O$_{\rm surf}$ | $n_c$ |
|---|---|---|---|---|---|---|---|---|---|---|---|---|
| 10 | 2.24 | 0.591 | 6.30E-03 | 2.50E-02 | 1.20E-02 | 5.30E-01 | 5.25E-01 | 15.1 | 2.84 | 2.61E-02 | 1.13 | 22 |
| 11 | 2.16 | 0.596 | 6.10E-03 | 2.38E-02 | 1.18E-02 | 5.16E-01 | 5.17E-01 | 14.0 | 2.85 | 2.69E-02 | 1.24 | 22 |
| 12 | 2.06 | 0.602 | 5.90E-03 | 2.28E-02 | 1.15E-02 | 5.07E-01 | 5.13E-01 | 13.0 | 2.87 | 2.77E-02 | 1.36 | 22 |
| 13 | 1.92 | 0.607 | 5.70E-03 | 2.19E-02 | 1.12E-02 | 4.99E-01 | 4.09E-01 | 12.0 | 2.89 | 2.85E-02 | 1.48 | 21 |
| 14 | 1.76 | 0.612 | 5.30E-03 | 2.09E-02 | 1.09E-02 | 4.90E-01 | 4.86E-01 | 11.2 | 2.91 | 2.95E-02 | 1.60 | 21 |
| 15 | 1.57 | 0.617 | 4.90E-03 | 2.00E-02 | 1.04E-02 | 4.89E-01 | 4.71E-01 | 10.3 | 2.92 | 3.05E-02 | 1.75 | 21 |
| 16 | 1.35 | 0.623 | 3.90E-03 | 1.91E-02 | 1.00E-02 | 4.86E-01 | 3.90E-01 | 9.5 | 2.92 | 3.15E-02 | 1.89 | 21 |
| | $M^{\rm Tot}_{\rm TDU}$ = **7.82E-02** $M_\odot$ | | | | | | $\tau_C$ = **9.27E+05 yr** | | | | | |
| | | | | | | $M$=**3.0** $M_\odot$ | | | | | | |
| -3 | 2.98 | 0.550 | 0.00E+00 | 2.96E-02 | 2.50E-03 | 9.54E-01 | 0.00E+00 | 9.7 | 2.06 | 2.02E-02 | 0.31 | ··· |
| -2$^{(*)}$ | 2.97 | 0.555 | 0.00E+00 | 3.04E-02 | 4.40E-03 | 8.81E-01 | 0.00E+00 | 13.4 | 2.24 | 2.02E-02 | 0.31 | ··· |
| -1 | 2.97 | 0.560 | 0.00E+00 | 2.96E-02 | 5.50E-03 | 8.33E-01 | 0.00E+00 | 15.3 | 2.35 | 2.02E-02 | 0.31 | ··· |

Table 3—Continued

| $n^a_{\rm TP}$ | $M^b_{\rm Tot}$ | $M^b_{\rm H}$ | $\Delta M^b_{\rm TDU}$ | $\Delta M^b_{\rm CZ}$ | $\Delta M^b_{\rm H}$ | $r$ | $\lambda$ | $\Delta t^c_{ip}$ | $T^d_{MAX}$ | $Z_{surf}$ | $C/O_{\rm surf}$ | $n_c$ |
|---|---|---|---|---|---|---|---|---|---|---|---|---|
| 1 | 2.96 | 0.567 | 8.00E-04 | 2.89E-02 | 6.80E-03 | 7.81E-01 | 1.18E-01 | 16.0 | 2.46 | 2.02E-02 | 0.32 | 2 |
| 2 | 2.96 | 0.574 | 2.30E-03 | 2.77E-02 | 7.80E-03 | 7.34E-01 | 2.95E-01 | 15.9 | 2.55 | 2.04E-02 | 0.35 | 16 |
| 3 | 2.94 | 0.581 | 3.60E-03 | 2.69E-02 | 9.10E-03 | 6.74E-01 | 3.96E-01 | 15.7 | 2.63 | 2.08E-02 | 0.41 | 35 |
| 4 | 2.93 | 0.587 | 4.90E-03 | 2.60E-02 | 9.90E-03 | 6.31E-01 | 4.95E-01 | 15.4 | 2.71 | 2.14E-02 | 0.48 | 33 |
| 5 | 2.91 | 0.593 | 5.90E-03 | 2.53E-02 | 1.08E-02 | 5.81E-01 | 5.46E-01 | 15.0 | 2.77 | 2.20E-02 | 0.57 | 31 |
| 6 | 2.87 | 0.598 | 6.70E-03 | 2.45E-02 | 1.14E-02 | 5.45E-01 | 5.88E-01 | 14.5 | 2.82 | 2.26E-02 | 0.66 | 27 |
| 7 | 2.81 | 0.603 | 7.00E-03 | 2.37E-02 | 1.18E-02 | 5.11E-01 | 5.93E-01 | 13.9 | 2.87 | 2.33E-02 | 0.76 | 26 |
| 8 | 2.74 | 0.608 | 7.00E-03 | 2.30E-02 | 1.18E-02 | 4.91E-01 | 5.93E-01 | 13.3 | 2.91 | 2.40E-02 | 0.86 | 25 |
| 9 | 2.63 | 0.613 | 7.10E-03 | 2.21E-02 | 1.17E-02 | 4.78E-01 | 6.07E-01 | 12.5 | 2.93 | 2.47E-02 | 0.96 | 25 |
| 10 | 2.49 | 0.617 | 6.80E-03 | 2.13E-02 | 1.16E-02 | 4.61E-01 | 5.86E-01 | 11.7 | 2.95 | 2.54E-02 | 1.07 | 25 |
| 11 | 2.32 | 0.622 | 6.50E-03 | 2.05E-02 | 1.13E-02 | 4.55E-01 | 5.75E-01 | 11.0 | 2.97 | 2.62E-02 | 1.18 | 24 |
| 12 | 2.10 | 0.626 | 6.20E-03 | 1.97E-02 | 1.09E-02 | 4.52E-01 | 5.74E-01 | 10.3 | 2.99 | 2.71E-02 | 1.30 | 22 |
| 13 | 1.84 | 0.631 | 5.70E-03 | 1.89E-02 | 1.07E-02 | 4.41E-01 | 5.33E-01 | 9.6 | 2.99 | 2.80E-02 | 1.43 | 22 |
| 14 | 1.55 | 0.635 | 4.90E-03 | 1.80E-02 | 1.01E-02 | 4.44E-01 | 4.85E-01 | 8.8 | 3.00 | 2.91E-02 | 1.59 | 21 |

$M^{\rm Tot}_{\rm TDU}$ = **7.54E-02** $M_\odot$ $\tau_C$ = **4.62E+05 yr**

Table 3—Continued

| $n^a_{\rm TP}$ | $M^b_{\rm Tot}$ | $M^b_{\rm H}$ | $\Delta M^b_{\rm TDU}$ | $\Delta M^b_{\rm CZ}$ | $\Delta M^b_{\rm H}$ | $r$ | $\lambda$ | $\Delta t^c_{ip}$ | $T^d_{MAX}$ | $Z_{surf}$ | $C/O_{\rm surf}$ | $n_c$ |
|---|---|---|---|---|---|---|---|---|---|---|---|---|

[a]Pulse number (negative values correspond to TP not followed by TDU)

[b]$M_\odot$

[c]$10^4$ yr

[d]$10^8$ K

[(*)]$M_{\rm H}$ of this TP corresponds to $M^3_{\rm He}$ of Table 2

Table 4. Evolution of selected physical parameters of the models at $Z = 6 \times 10^{-3}$.

| $n^a_{\rm TP}$ | $M^b_{\rm Tot}$ | $M^b_{\rm H}$ | $\Delta M^b_{\rm TDU}$ | $\Delta M^b_{\rm CZ}$ | $\Delta M^b_{\rm H}$ | $r$ | $\lambda$ | $\Delta t^c_{ip}$ | $T^d_{MAX}$ | $\rm Z_{surf}$ | $\rm C/O_{surf}$ | $n_c$ |
|---|---|---|---|---|---|---|---|---|---|---|---|---|
| | | | | | | $M$=**1.5** $M_\odot$ | | | | | | |
| -3 | 1.36 | 0.552 | 0.00E+00 | 3.13E-02 | 2.50E-03 | 9.59E-01 | 0.00E+00 | 10.2 | 2.07 | 6.06E-03 | 0.32 | ··· |
| -2$^{(*)}$ | 1.35 | 0.556 | 0.00E+00 | 3.18E-02 | 4.50E-03 | 8.81E-01 | 0.00E+00 | 15.6 | 2.26 | 6.06E-03 | 0.32 | ··· |
| -1 | 1.34 | 0.563 | 0.00E+00 | 3.11E-02 | 6.80E-03 | 8.17E-01 | 0.00E+00 | 17.9 | 2.40 | 6.06E-03 | 0.32 | ··· |
| 1 | 1.33 | 0.570 | 2.00E-04 | 2.97E-02 | 6.90E-03 | 7.87E-01 | 2.90E-02 | 18.1 | 2.51 | 6.06E-03 | 0.32 | 42 |
| 2 | 1.31 | 0.578 | 1.10E-03 | 2.78E-02 | 8.30E-03 | 7.29E-01 | 1.33E-01 | 17.2 | 2.57 | 6.25E-03 | 0.42 | 120 |
| 3 | 1.29 | 0.585 | 1.60E-03 | 2.64E-02 | 8.70E-03 | 6.81E-01 | 1.84E-01 | 16.1 | 2.65 | 6.78E-03 | 0.66 | 130 |
| 4 | 1.26 | 0.593 | 2.20E-03 | 2.50E-02 | 9.20E-03 | 6.39E-01 | 2.39E-01 | 14.9 | 2.71 | 7.62E-03 | 1.05 | 120 |
| 5 | 1.24 | 0.600 | 2.70E-03 | 2.37E-02 | 9.60E-03 | 6.04E-01 | 2.81E-01 | 13.7 | 2.75 | 8.67E-03 | 1.53 | 110 |
| 6 | 1.20 | 0.607 | 2.80E-03 | 2.24E-02 | 9.60E-03 | 5.78E-01 | 2.92E-01 | 12.5 | 2.79 | 9.84E-03 | 2.05 | 97 |
| 7 | 1.16 | 0.614 | 2.80E-03 | 2.12E-02 | 9.50E-03 | 5.59E-01 | 2.95E-01 | 11.4 | 2.82 | 1.11E-02 | 2.59 | 91 |
| 8 | 1.09 | 0.620 | 2.40E-03 | 2.01E-02 | 9.20E-03 | 5.44E-01 | 2.62E-01 | 10.4 | 2.84 | 1.23E-02 | 3.16 | 87 |

$M^{\rm Tot}_{\rm TDU}$ = **1.58E-02** $M_\odot$ $\tau_C$ = **7.86E+05 yr**

Table 4—Continued

| $n^a_{\rm TP}$ | $M^b_{\rm Tot}$ | $M^b_{\rm H}$ | $\Delta M^b_{\rm TDU}$ | $\Delta M^b_{\rm CZ}$ | $\Delta M^b_{\rm H}$ | $r$ | $\lambda$ | $\Delta t^c_{ip}$ | $T^d_{MAX}$ | $Z_{surf}$ | $C/O_{\rm surf}$ | $n_c$ |
|---|---|---|---|---|---|---|---|---|---|---|---|---|
| | | | | | | $M$=**2.0** $M_\odot$ | | | | | | |
| -2$^{(*)}$ | 1.97 | 0.555 | 0.00E+00 | 3.32E-02 | 4.70E-03 | 8.82E-01 | 0.00E+00 | 1 5.9 | 2.27 | 6.07E-03 | 0.29 | ··· |
| -1 | 1.97 | 0.561 | 0.00E+00 | 3.20E-02 | 6.30E-03 | 8.21E-01 | 0.00E+00 | 2 0.3 | 2.42 | 6.07E-03 | 0.29 | ··· |
| 1 | 1.96 | 0.569 | 1.60E-03 | 3.06E-02 | 7.90E-03 | 7.58E-01 | 2.03E-01 | 2 0.9 | 2.55 | 6.29E-03 | 0.40 | 110 |
| 2 | 1.95 | 0.577 | 3.40E-03 | 2.91E-02 | 9.50E-03 | 6.87E-01 | 3.58E-01 | 2 0.4 | 2.65 | 6.91E-03 | 0.69 | 140 |
| 3 | 1.93 | 0.585 | 5.30E-03 | 2.80E-02 | 1.09E-02 | 6.25E-01 | 4.86E-01 | 1 9.6 | 2.74 | 7.91E-03 | 1.15 | 110 |
| 4 | 1.91 | 0.591 | 6.70E-03 | 2.70E-02 | 1.20E-02 | 5.68E-01 | 5.58E-01 | 1 8.8 | 2.82 | 9.13E-03 | 1.70 | 110 |
| 5 | 1.89 | 0.597 | 7.30E-03 | 2.60E-02 | 1.28E-02 | 5.19E-01 | 5.70E-01 | 17.7 | 2.87 | 1.04E-02 | 2.27 | 94 |
| 6 | 1.86 | 0.603 | 7.60E-03 | 2.50E-02 | 1.29E-02 | 4.93E-01 | 5.89E-01 | 16.5 | 2.90 | 1.18E-02 | 2.85 | 91 |
| 7 | 1.81 | 0.608 | 7.60E-03 | 2.40E-02 | 1.29E-02 | 4.71E-01 | 5.89E-01 | 15.3 | 2.93 | 1.31E-02 | 3.42 | 87 |
| 8 | 1.75 | 0.613 | 7.40E-03 | 2.30E-02 | 1.27E-02 | 4.59E-01 | 5.83E-01 | 14.1 | 2.96 | 1.45E-02 | 3.99 | 85 |
| 9 | 1.66 | 0.618 | 7.10E-03 | 2.20E-02 | 1.22E-02 | 4.58E-01 | 5.82E-01 | 12.9 | 2.99 | 1.58E-02 | 4.56 | 84 |

Table 4—Continued

| $n^a_{\rm TP}$ | $M^b_{\rm Tot}$ | $M^b_{\rm H}$ | $\Delta M^b_{\rm TDU}$ | $\Delta M^b_{\rm CZ}$ | $\Delta M^b_{\rm H}$ | $r$ | $\lambda$ | $\Delta t^c_{ip}$ | $T^d_{MAX}$ | $Z_{surf}$ | C/O$_{\rm surf}$ | $n_c$ |
|---|---|---|---|---|---|---|---|---|---|---|---|---|
| 10 | 1.55 | 0.623 | 6.50E-03 | 2.10E-02 | 1.18E-02 | 4.45E-01 | 5.51E-01 | 11.9 | 3.00 | 1.72E-02 | 5.13 | 82 |
| 11 | 1.40 | 0.628 | 5.50E-03 | 1.98E-02 | 1.14E-02 | 4.34E-01 | 4.82E-01 | 10.8 | 3.00 | 1.87E-02 | 5.71 | 80 |
| 12 | 1.21 | 0.633 | 4.50E-03 | 1.87E-02 | 1.06E-02 | 4.45E-01 | 4.25E-01 | 9.68 | 3.00 | 2.02E-02 | 6.35 | 79 |
| 13 | 1.00 | 0.638 | 1.50E-03 | 1.75E-02 | 9.60E-03 | 4.60E-01 | 1.56E-01 | 8.47 | 2.99 | 2.11E-02 | 6.67 | 65 |
| 14 | 0.83 | 0.644 | 7.00E-04 | 1.54E-02 | 7.80E-03 | 5.04E-01 | 9.00E-02 | 6.91 | 2.92 | 2.17E-02 | 6.91 | 63 |
| | $M^{\rm Tot}_{\rm TDU}$ = **7.27E-02** $M_\odot$ | | | | | | $\tau_C$ = **1.38E+06 yr** | | | | | |
| | | | | | | $M$=**2.5** $M_\odot$ | | | | | | |
| -1$^{(*)}$ | 2.47 | 0.549 | 0.00E+00 | 3.44E-02 | 4.90E-03 | 8.78E-01 | 0.00E+00 | 18.1 | 2.28 | 6.06E-03 | 0.29 | ··· |
| 1 | 2.47 | 0.555 | 3.00E-04 | 3.30E-02 | 6.70E-03 | 8.16E-01 | 4.48E-02 | 22.1 | 2.42 | 6.06E-03 | 0.29 | 31 |
| 2 | 2.46 | 0.563 | 2.20E-03 | 3.16E-02 | 8.30E-03 | 7.52E-01 | 2.65E-01 | 22.4 | 2.54 | 6.32E-03 | 0.42 | 140 |
| 3 | 2.45 | 0.571 | 4.50E-03 | 3.04E-02 | 9.90E-03 | 6.85E-01 | 4.55E-01 | 21.9 | 2.65 | 6.94E-03 | 0.72 | 140 |
| 4 | 2.44 | 0.578 | 6.30E-03 | 2.93E-02 | 1.16E-02 | 6.17E-01 | 5.43E-01 | 21.3 | 2.74 | 7.81E-03 | 1.13 | 110 |

Table 4—Continued

| $n^a_{\rm TP}$ | $M^b_{\rm Tot}$ | $M^b_{\rm H}$ | $\Delta M^b_{\rm TDU}$ | $\Delta M^b_{\rm CZ}$ | $\Delta M^b_{\rm H}$ | $r$ | $\lambda$ | $\Delta t^c_{ip}$ | $T^d_{MAX}$ | $Z_{surf}$ | $C/O_{\rm surf}$ | $n_c$ |
|---|---|---|---|---|---|---|---|---|---|---|---|---|
| 5 | 2.42 | 0.585 | 7.60E-03 | 2.84E-02 | 1.27E-02 | 5.63E-01 | 5.98E-01 | 20.5 | 2.81 | 8.82E-03 | 1.60 | 95 |
| 6 | 2.40 | 0.591 | 8.50E-03 | 2.75E-02 | 1.35E-02 | 5.20E-01 | 6.30E-01 | 19.4 | 2.87 | 9.88E-03 | 2.08 | 87 |
| 7 | 2.38 | 0.596 | 8.80E-03 | 2.66E-02 | 1.39E-02 | 4.86E-01 | 6.33E-01 | 18.3 | 2.91 | 1.10E-02 | 2.56 | 75 |
| 8 | 2.36 | 0.601 | 9.00E-03 | 2.56E-02 | 1.39E-02 | 4.67E-01 | 6.47E-01 | 17.1 | 2.95 | 1.20E-02 | 3.03 | 73 |
| 9 | 2.33 | 0.606 | 9.10E-03 | 2.47E-02 | 1.38E-02 | 4.49E-01 | 6.59E-01 | 15.9 | 2.98 | 1.31E-02 | 3.50 | 73 |
| 10 | 2.29 | 0.610 | 8.90E-03 | 2.38E-02 | 1.37E-02 | 4.32E-01 | 6.50E-01 | 14.8 | 2.99 | 1.41E-02 | 3.97 | 72 |
| 11 | 2.23 | 0.615 | 8.70E-03 | 2.29E-02 | 1.34E-02 | 4.25E-01 | 6.49E-01 | 13.8 | 3.02 | 1.52E-02 | 4.43 | 71 |
| 12 | 2.16 | 0.619 | 8.50E-03 | 2.20E-02 | 1.30E-02 | 4.20E-01 | 6.54E-01 | 12.8 | 3.04 | 1.63E-02 | 4.88 | 69 |
| 13 | 2.07 | 0.623 | 8.10E-03 | 2.12E-02 | 1.27E-02 | 4.11E-01 | 6.38E-01 | 11.9 | 3.05 | 1.73E-02 | 5.34 | 66 |
| 14 | 1.95 | 0.628 | 7.70E-03 | 2.03E-02 | 1.22E-02 | 4.09E-01 | 6.31E-01 | 11.1 | 3.06 | 1.85E-02 | 5.81 | 79 |
| 15 | 1.80 | 0.632 | 7.10E-03 | 1.95E-02 | 1.18E-02 | 4.05E-01 | 6.02E-01 | 10.3 | 3.06 | 1.96E-02 | 6.29 | 75 |
| 16 | 1.62 | 0.636 | 6.30E-03 | 1.87E-02 | 1.12E-02 | 4.10E-01 | 5.63E-01 | 9.5 | 3.07 | 2.09E-02 | 6.80 | 72 |
| 17 | 1.39 | 0.640 | 5.10E-03 | 1.77E-02 | 1.05E-02 | 4.17E-01 | 4.86E-01 | 8.7 | 3.06 | 2.22E-02 | 7.35 | 83 |
| 18 | 1.13 | 0.644 | 3.40E-03 | 1.66E-02 | 9.60E-03 | 4.31E-01 | 3.54E-01 | 7.8 | 3.04 | 2.36E-02 | 7.90 | 70 |
| 19 | 0.89 | 0.649 | 1.10E-03 | 1.51E-02 | 8.30E-03 | 4.58E-01 | 1.33E-01 | 6.5 | 3.00 | 2.45E-02 | 8.25 | 70 |

Table 4—Continued

| $n^a_{\rm TP}$ | $M^b_{\rm Tot}$ | $M^b_{\rm H}$ | $\Delta M^b_{\rm TDU}$ | $\Delta M^b_{\rm CZ}$ | $\Delta M^b_{\rm H}$ | $r$ | $\lambda$ | $\Delta t^c_{ip}$ | $T^d_{MAX}$ | $Z_{surf}$ | $C/O_{\rm surf}$ | $n_c$ |
|---|---|---|---|---|---|---|---|---|---|---|---|---|
| | $M^{\rm Tot}_{\rm TDU}$ = **1.21E-01** $M_\odot$ | | | | | | $\tau_C$ = **1.99E+06 yr** | | | | | |
| | | | | | $M$=**3.0** $M_\odot$ | | | | | | | |
| -2 | 2.96 | 0.653 | 0.00E+00 | 1.67E-02 | ··· | ··· | ··· | ··· | 2.23 | 6.06E-03 | 0.29 | ··· |
| -1$^{(*)}$ | 2.96 | 0.656 | 0.00E+00 | 1.66E-02 | 3.40E-03 | 8.24E-01 | 0.00E+00 | 5.2 | 2.41 | 6.06E-03 | 0.29 | ··· |
| 1 | 2.95 | 0.661 | 8.00E-04 | 1.63E-02 | 4.40E-03 | 7.47E-01 | 1.82E-01 | 5.9 | 2.57 | 6.11E-03 | 0.31 | 82 |
| 2 | 2.94 | 0.665 | 2.20E-03 | 1.57E-02 | 5.40E-03 | 6.74E-01 | 4.07E-01 | 6.1 | 2.69 | 6.31E-03 | 0.42 | 100 |
| 3 | 2.93 | 0.670 | 3.20E-03 | 1.54E-02 | 6.40E-03 | 5.96E-01 | 5.00E-01 | 6.2 | 2.79 | 6.66E-03 | 0.59 | 100 |
| 4 | 2.89 | 0.673 | 4.10E-03 | 1.51E-02 | 7.00E-03 | 5.44E-01 | 5.86E-01 | 6.3 | 2.89 | 7.13E-03 | 0.83 | 100 |
| 5 | 2.84 | 0.677 | 4.90E-03 | 1.49E-02 | 7.60E-03 | 4.94E-01 | 6.45E-01 | 6.4 | 2.97 | 7.69E-03 | 1.10 | 100 |
| 6 | 2.77 | 0.680 | 5.60E-03 | 1.46E-02 | 8.20E-03 | 4.50E-01 | 6.83E-01 | 6.4 | 3.03 | 8.32E-03 | 1.41 | 99 |
| 7 | 2.66 | 0.683 | 5.90E-03 | 1.44E-02 | 8.50E-03 | 4.14E-01 | 6.94E-01 | 6.3 | 3.09 | 9.01E-03 | 1.75 | 97 |
| 8 | 2.52 | 0.686 | 6.20E-03 | 1.42E-02 | 8.70E-03 | 3.92E-01 | 7.13E-01 | 6.2 | 3.14 | 9.77E-03 | 2.11 | 94 |

Table 4—Continued

| $n^a_{\rm TP}$ | $M^b_{\rm Tot}$ | $M^b_{\rm H}$ | $\Delta M^b_{\rm TDU}$ | $\Delta M^b_{\rm CZ}$ | $\Delta M^b_{\rm H}$ | $r$ | $\lambda$ | $\Delta t^c_{ip}$ | $T^d_{MAX}$ | $\rm Z_{surf}$ | $\rm C/O_{surf}$ | $n_c$ |
|---|---|---|---|---|---|---|---|---|---|---|---|---|
| 9 | 2.34 | 0.689 | 6.30E-03 | 1.39E-02 | 8.90E-03 | 3.70E-01 | 7.08E-01 | 6.0 | 3.16 | 1.06E-02 | 2.51 | 82 |
| 10 | 2.11 | 0.691 | 6.10E-03 | 1.36E-02 | 8.80E-03 | 3.59E-01 | 6.93E-01 | 5.8 | 3.20 | 1.16E-02 | 2.97 | 100 |
| 11 | 1.82 | 0.694 | 5.60E-03 | 1.33E-02 | 8.70E-03 | 3.53E-01 | 6.44E-01 | 5.6 | 3.21 | 1.27E-02 | 3.49 | 110 |
| 12 | 1.45 | 0.696 | 4.10E-03 | 1.28E-02 | 8.30E-03 | 3.58E-01 | 4.94E-01 | 5.3 | 3.22 | 1.39E-02 | 4.05 | 110 |
| 13 | 1.08 | 0.700 | 1.70E-03 | 1.18E-02 | 7.40E-03 | 3.79E-01 | 2.30E-01 | 4.7 | 3.20 | 1.47E-02 | 4.54 | 100 |
| | $M^{\rm Tot}_{\rm TDU}$ = **5.67E-02** $M_\odot$ | | | | | | | $\tau_C$ = **4.93E+05 yr** | | | | |

[a] Pulse number (negative values correspond to TP not followed by TDU)

[b] $M_\odot$

[c] $10^4$ yr

[d] $10^8$ K

[(*)] $M_{\rm H}$ of this TP corresponds to $M^3_{\rm He}$ of Table 2

Table 5. Evolution of selected physical parameters of the models at $Z = 1 \times 10^{-3}$.

| $n^a_{\rm TP}$ | $M^b_{\rm Tot}$ | $M^b_{\rm H}$ | $\Delta M^b_{\rm TDU}$ | $\Delta M^b_{\rm CZ}$ | $\Delta M^b_{\rm H}$ | $r$ | $\lambda$ | $\Delta t^c_{ip}$ | $T^d_{MAX}$ | $Z_{surf}$ | C/O$_{\rm surf}$ | $n_c$ |
|---|---|---|---|---|---|---|---|---|---|---|---|---|
| | | | | | | | | | | | | |
| | | | | | | $M$=**1.5** $M_\odot$ | | | | | | |
| -2 | 1.40 | 0.566 | 0.00E+00 | 2.81E-02 | 1.70E-03 | 1.08E+00 | 0.00E+00 | 7.8 | 2.00 | 1.01E-03 | 0.29 | ··· |
| -1$^{(*)}$ | 1.39 | 0.572 | 0.00E+00 | 3.16E-02 | 5.50E-03 | 8.47E-01 | 0.00E+00 | 17.6 | 2.40 | 1.01E-03 | 0.29 | ··· |
| 1 | 1.39 | 0.579 | 2.30E-03 | 3.01E-02 | 7.50E-03 | 7.68E-01 | 3.07E-01 | 22.2 | 2.58 | 1.58E-03 | 1.95 | 740 |
| 2 | 1.38 | 0.587 | 4.50E-03 | 2.84E-02 | 9.70E-03 | 6.73E-01 | 4.64E-01 | 21.1 | 2.70 | 3.01E-03 | 5.51 | 830 |
| 3 | 1.36 | 0.593 | 5.90E-03 | 2.71E-02 | 1.12E-02 | 5.99E-01 | 5.27E-01 | 19.3 | 2.79 | 4.96E-03 | 9.34 | 710 |
| 4 | 1.34 | 0.599 | 6.80E-03 | 2.59E-02 | 1.21E-02 | 5.44E-01 | 5.62E-01 | 17.7 | 2.85 | 7.19E-03 | 12.8 | 680 |
| 5 | 1.31 | 0.605 | 7.00E-03 | 2.48E-02 | 1.26E-02 | 5.03E-01 | 5.63E-01 | 16.2 | 2.90 | 9.33E-03 | 15.5 | 620 |
| 6 | 1.29 | 0.611 | 7.10E-03 | 2.36E-02 | 1.25E-02 | 4.86E-01 | 5.60E-01 | 14.6 | 2.93 | 1.19E-02 | 18.3 | 610 |
| 7 | 1.25 | 0.616 | 6.50E-03 | 2.24E-02 | 1.21E-02 | 4.68E-01 | 5.37E-01 | 13.2 | 2.96 | 1.41E-02 | 20.6 | 590 |
| 8 | 1.22 | 0.621 | 6.10E-03 | 2.13E-02 | 1.16E-02 | 4.64E-01 | 5.26E-01 | 11.9 | 2.97 | 1.63E-02 | 22.5 | 560 |
| 9 | 1.19 | 0.626 | 5.30E-03 | 2.01E-02 | 1.11E-02 | 4.56E-01 | 4.77E-01 | 10.7 | 2.98 | 1.84E-02 | 24.2 | 510 |
| 10 | 1.15 | 0.631 | 4.50E-03 | 1.90E-02 | 1.04E-02 | 4.61E-01 | 4.33E-01 | 9.6 | 2.98 | 2.03E-02 | 25.7 | 530 |

Table 5—Continued

| $n^a_{\rm TP}$ | $M^b_{\rm Tot}$ | $M^b_{\rm H}$ | $\Delta M^b_{\rm TDU}$ | $\Delta M^b_{\rm CZ}$ | $\Delta M^b_{\rm H}$ | $r$ | $\lambda$ | $\Delta t^c_{ip}$ | $T^d_{MAX}$ | $Z_{surf}$ | $C/O_{\rm surf}$ | $n_c$ |
|---|---|---|---|---|---|---|---|---|---|---|---|---|
| 11 | 1.11 | 0.636 | 3.60E-03 | 1.78E-02 | 9.80E-03 | 4.62E-01 | 3.67E-01 | 8.6 | 2.97 | 2.20E-02 | 26.9 | 560 |
| 12 | 1.06 | 0.642 | 2.70E-03 | 1.68E-02 | 9.00E-03 | 4.73E-01 | 3.00E-01 | 7.7 | 2.96 | 2.35E-02 | 28.0 | 520 |
| 13 | 1.00 | 0.647 | 1.80E-03 | 1.57E-02 | 8.30E-03 | 4.79E-01 | 2.17E-01 | 6.9 | 2.95 | 2.47E-02 | 28.8 | 540 |
| 14 | 0.94 | 0.653 | 2.00E-04 | 1.47E-02 | 7.60E-03 | 4.92E-01 | 2.63E-02 | 6.1 | 2.93 | 2.50E-02 | 29.0 | 480 |
| | $M^{\rm Tot}_{\rm TDU}$ = **6.43E-02** $M_\odot$ | | | | | | $\tau_C$ = **1.50E+06 yr** | | | | | |
| | | | | | | $M$=**2.0** $M_\odot$ | | | | | | |
| -1$^{(*)}$ | 1.94 | 0.600 | 0.00E+00 | 2.36E-02 | 2.20E-03 | 9.55E-01 | 0.00E+00 | 6.48 | 2.13 | 1.01E-03 | 0.25 | $\cdots$ |
| 1 | 1.93 | 0.604 | 2.00E-04 | 2.53E-02 | 4.70E-03 | 8.23E-01 | 4.30E-02 | 12.6 | 2.47 | 1.03E-03 | 0.31 | 370 |
| 2 | 1.92 | 0.611 | 3.00E-03 | 2.41E-02 | 6.70E-03 | 7.31E-01 | 4.48E-01 | 15.1 | 2.64 | 1.56E-03 | 1.85 | 1000 |
| 3 | 1.91 | 0.617 | 5.40E-03 | 2.33E-02 | 8.80E-03 | 6.27E-01 | 6.14E-01 | 15.0 | 2.79 | 2.63E-03 | 4.56 | 730 |
| 4 | 1.89 | 0.622 | 7.20E-03 | 2.28E-02 | 1.06E-02 | 5.36E-01 | 6.79E-01 | 14.7 | 2.90 | 4.05E-03 | 7.64 | 670 |
| 5 | 1.88 | 0.627 | 8.50E-03 | 2.23E-02 | 1.19E-02 | 4.72E-01 | 7.14E-01 | 14.2 | 2.98 | 5.64E-03 | 10.6 | 650 |

Table 5—Continued

| $n^a_{\rm TP}$ | $M^b_{\rm Tot}$ | $M^b_{\rm H}$ | $\Delta M^b_{\rm TDU}$ | $\Delta M^b_{\rm CZ}$ | $\Delta M^b_{\rm H}$ | $r$ | $\lambda$ | $\Delta t^c_{ip}$ | $T^d_{MAX}$ | $\rm Z_{\it surf}$ | $\rm C/O_{surf}$ | $n_c$ |
|---|---|---|---|---|---|---|---|---|---|---|---|---|
| 6 | 1.85 | 0.631 | 9.30E-03 | 2.19E-02 | 1.26E-02 | 4.27E-01 | 7.38E-01 | 13.6 | 3.03 | 7.31E-03 | 13.3 | 670 |
| 7 | 1.83 | 0.635 | 9.70E-03 | 2.14E-02 | 1.31E-02 | 3.94E-01 | 7.40E-01 | 13.0 | 3.08 | 9.01E-03 | 15.9 | 650 |
| 8 | 1.81 | 0.638 | 9.70E-03 | 2.09E-02 | 1.31E-02 | 3.78E-01 | 7.40E-01 | 12.2 | 3.11 | 1.07E-02 | 18.3 | 630 |
| 9 | 1.78 | 0.641 | 9.70E-03 | 2.03E-02 | 1.29E-02 | 3.70E-01 | 7.52E-01 | 11.5 | 3.15 | 1.24E-02 | 20.5 | 630 |
| 10 | 1.75 | 0.644 | 9.50E-03 | 1.97E-02 | 1.27E-02 | 3.58E-01 | 7.48E-01 | 10.8 | 3.16 | 1.41E-02 | 22.5 | 670 |
| 11 | 1.71 | 0.647 | 9.20E-03 | 1.91E-02 | 1.25E-02 | 3.51E-01 | 7.36E-01 | 10.1 | 3.18 | 1.58E-02 | 24.4 | 640 |
| 12 | 1.66 | 0.650 | 8.80E-03 | 1.85E-02 | 1.20E-02 | 3.51E-01 | 7.33E-01 | 9.46 | 3.18 | 1.74E-02 | 26.2 | 660 |
| 13 | 1.61 | 0.653 | 8.40E-03 | 1.79E-02 | 1.17E-02 | 3.48E-01 | 7.18E-01 | 8.83 | 3.18 | 1.91E-02 | 27.8 | 650 |
| 14 | 1.53 | 0.656 | 8.00E-03 | 1.72E-02 | 1.13E-02 | 3.50E-01 | 7.08E-01 | 8.24 | 3.19 | 2.08E-02 | 29.4 | 620 |
| 15 | 1.45 | 0.659 | 7.30E-03 | 1.66E-02 | 1.08E-02 | 3.50E-01 | 6.76E-01 | 7.65 | 3.18 | 2.26E-02 | 30.9 | 640 |
| 16 | 1.34 | 0.661 | 6.40E-03 | 1.58E-02 | 1.02E-02 | 3.56E-01 | 6.27E-01 | 7.06 | 3.17 | 2.44E-02 | 32.3 | 610 |
| 17 | 1.22 | 0.665 | 5.30E-03 | 1.50E-02 | 9.50E-03 | 3.68E-01 | 5.58E-01 | 6.46 | 3.17 | 2.62E-02 | 33.7 | 600 |
| 18 | 1.09 | 0.668 | 3.70E-03 | 1.41E-02 | 8.70E-03 | 3.82E-01 | 4.25E-01 | 5.83 | 3.13 | 2.80E-02 | 34.9 | 600 |
| 19 | 0.96 | 0.672 | 2.00E-03 | 1.31E-02 | 7.50E-03 | 4.11E-01 | 2.67E-01 | 5.14 | 3.10 | 2.96E-02 | 36.0 | 610 |

$M^{\rm Tot}_{\rm TDU}$ = **1.31E-01** $M_\odot$ $\tau_C$ = **1.85E+06 yr**

Table 5—Continued

| $n^a_{\rm TP}$ | $M^b_{\rm Tot}$ | $M^b_{\rm H}$ | $\Delta M^b_{\rm TDU}$ | $\Delta M^b_{\rm CZ}$ | $\Delta M^b_{\rm H}$ | $r$ | $\lambda$ | $\Delta t^c_{ip}$ | $T^d_{MAX}$ | $Z_{surf}$ | $C/O_{\rm surf}$ | $n_c$ |
|---|---|---|---|---|---|---|---|---|---|---|---|---|
| | | | | | | $M$=**2.5** $M_\odot$ | | | | | | |
| 1 | 2.45 | 0.672 | 5.00E-04 | 1.56E-02 | 3.10E-03 | 8.30E-01 | 1.61E-01 | 4.8 | 2.45 | 1.02E-03 | 0.26 | 340 |
| 2 | 2.45 | 0.676 | 2.30E-03 | 1.51E-02 | 4.40E-03 | 7.27E-01 | 5.23E-01 | 6.5 | 2.65 | 1.25E-03 | 0.96 | 440 |
| 3 | 2.44 | 0.680 | 4.20E-03 | 1.49E-02 | 6.00E-03 | 6.14E-01 | 7.00E-01 | 7.0 | 2.82 | 1.81E-03 | 2.52 | 480 |
| 4 | 2.43 | 0.683 | 5.70E-03 | 1.49E-02 | 7.40E-03 | 5.18E-01 | 7.70E-01 | 7.4 | 2.96 | 2.61E-03 | 4.58 | 600 |
| 5 | 2.42 | 0.686 | 6.80E-03 | 1.49E-02 | 8.50E-03 | 4.44E-01 | 8.00E-01 | 7.7 | 3.07 | 3.56E-03 | 6.78 | 780 |
| 6 | 2.41 | 0.688 | 7.70E-03 | 1.50E-02 | 9.30E-03 | 3.90E-01 | 8.28E-01 | 7.8 | 3.16 | 4.59E-03 | 8.98 | 820 |
| 7 | 2.38 | 0.690 | 8.20E-03 | 1.50E-02 | 9.90E-03 | 3.44E-01 | 8.28E-01 | 7.8 | 3.24 | 5.67E-03 | 11.1 | 900 |
| 8 | 2.35 | 0.693 | 8.60E-03 | 1.49E-02 | 1.03E-02 | 3.16E-01 | 8.35E-01 | 7.7 | 3.30 | 6.80E-03 | 13.3 | 910 |
| 9 | 2.30 | 0.695 | 9.00E-03 | 1.49E-02 | 1.06E-02 | 2.96E-01 | 8.49E-01 | 7.6 | 3.33 | 7.97E-03 | 15.3 | 940 |
| 10 | 2.24 | 0.696 | 9.10E-03 | 1.48E-02 | 1.08E-02 | 2.76E-01 | 8.43E-01 | 7.4 | 3.37 | 9.19E-03 | 17.4 | 1000 |
| 11 | 2.16 | 0.698 | 9.00E-03 | 1.46E-02 | 1.08E-02 | 2.67E-01 | 8.33E-01 | 7.2 | 3.40 | 1.05E-02 | 19.3 | 1100 |

Table 5—Continued

| $n^a_{\rm TP}$ | $M^b_{\rm Tot}$ | $M^b_{\rm H}$ | $\Delta M^b_{\rm TDU}$ | $\Delta M^b_{\rm CZ}$ | $\Delta M^b_{\rm H}$ | $r$ | $\lambda$ | $\Delta t^c_{ip}$ | $T^d_{MAX}$ | $Z_{surf}$ | C/O$_{\rm surf}$ | $n_c$ |
|---|---|---|---|---|---|---|---|---|---|---|---|---|
| 12 | 2.07 | 0.700 | 9.10E-03 | 1.45E-02 | 1.07E-02 | 2.67E-01 | 8.50E-01 | 7.0 | 3.41 | 1.18E-02 | 21.3 | 1100 |
| 13 | 1.95 | 0.701 | 8.90E-03 | 1.42E-02 | 1.07E-02 | 2.55E-01 | 8.32E-01 | 6.7 | 3.43 | 1.32E-02 | 23.2 | 1100 |
| 14 | 1.81 | 0.703 | 8.60E-03 | 1.40E-02 | 1.05E-02 | 2.55E-01 | 8.19E-01 | 6.5 | 3.45 | 1.47E-02 | 25.1 | 1100 |
| 15 | 1.64 | 0.705 | 8.30E-03 | 1.37E-02 | 1.02E-02 | 2.59E-01 | 8.14E-01 | 6.2 | 3.45 | 1.64E-02 | 27.2 | 1100 |
| 16 | 1.43 | 0.706 | 7.50E-03 | 1.33E-02 | 9.90E-03 | 2.56E-01 | 7.58E-01 | 5.8 | 3.44 | 1.83E-02 | 29.3 | 1100 |
| 17 | 1.18 | 0.708 | 5.80E-03 | 1.26E-02 | 9.30E-03 | 2.70E-01 | 6.24E-01 | 5.3 | 3.42 | 2.07E-02 | 31.8 | 1100 |
| 18 | 0.94 | 0.710 | 2.40E-03 | 1.14E-02 | 7.90E-03 | 3.10E-01 | 3.04E-01 | 4.5 | 3.36 | 2.29E-02 | 33.8 | 970 |
| | $M^{\rm Tot}_{\rm TDU}$ = **1.22E-01** $M_\odot$ | | | | | | $\tau_C$ = **1.05E+06 yr** | | | | | |
| | | | | | | $M$=**3.0** $M_\odot$ | | | | | | |
| -1$^{(*)}$ | 2.95 | 0.777 | 0.00E+00 | 7.35E-03 | ··· | ··· | ··· | ··· | 2.35 | 1.01E-03 | 0.27 | ··· |
| 1 | 2.95 | 0.779 | 9.00E-04 | 7.49E-03 | 1.90E-03 | 7.85E-01 | 4.74E-01 | 1.8 | 2.55 | 1.06E-03 | 0.43 | 460 |
| 2 | 2.94 | 0.780 | 1.90E-03 | 7.25E-03 | 2.50E-03 | 6.77E-01 | 7.60E-01 | 1.9 | 2.71 | 1.25E-03 | 0.97 | 740 |

Table 5—Continued

| $n^a_{\rm TP}$ | $M^b_{\rm Tot}$ | $M^b_{\rm H}$ | $\Delta M^b_{\rm TDU}$ | $\Delta M^b_{\rm CZ}$ | $\Delta M^b_{\rm H}$ | $r$ | $\lambda$ | $\Delta t^c_{ip}$ | $T^d_{MAX}$ | $\rm Z_{surf}$ | $\rm C/O_{surf}$ | $n_c$ |
|---|---|---|---|---|---|---|---|---|---|---|---|---|
| 3 | 2.94 | 0.782 | 2.70E-03 | 7.14E-03 | 3.10E-03 | 5.66E-01 | 8.71E-01 | 2.1 | 2.85 | 1.60E-03 | 1.86 | 720 |
| 4 | 2.92 | 0.783 | 3.30E-03 | 7.18E-03 | 3.80E-03 | 4.87E-01 | 8.46E-01 | 2.3 | 2.99 | 2.00E-03 | 2.86 | 840 |
| 5 | 2.89 | 0.784 | 3.60E-03 | 7.17E-03 | 4.30E-03 | 4.18E-01 | 8.37E-01 | 2.4 | 3.10 | 2.43E-03 | 3.90 | 920 |
| 6 | 2.85 | 0.785 | 3.80E-03 | 7.18E-03 | 4.60E-03 | 3.73E-01 | 8.26E-01 | 2.5 | 3.18 | 2.89E-03 | 4.99 | 1000 |
| 7 | 2.79 | 0.786 | 3.90E-03 | 7.24E-03 | 4.80E-03 | 3.39E-01 | 8.13E-01 | 2.5 | 3.26 | 3.39E-03 | 6.13 | 1200 |
| 8 | 2.72 | 0.787 | 4.00E-03 | 7.29E-03 | 5.00E-03 | 3.19E-01 | 8.00E-01 | 2.6 | 3.32 | 3.94E-03 | 7.32 | 1300 |
| 9 | 2.62 | 0.788 | 4.30E-03 | 7.35E-03 | 5.10E-03 | 3.17E-01 | 8.43E-01 | 2.6 | 3.38 | 4.53E-03 | 8.57 | 1600 |
| 10 | 2.51 | 0.789 | 4.40E-03 | 7.37E-03 | 5.30E-03 | 2.88E-01 | 8.30E-01 | 2.6 | 3.43 | 5.18E-03 | 9.88 | 1900 |
| 11 | 2.38 | 0.790 | 4.50E-03 | 7.38E-03 | 5.40E-03 | 2.73E-01 | 8.33E-01 | 2.6 | 3.46 | 5.90E-03 | 11.3 | 2300 |
| 12 | 2.23 | 0.791 | 4.70E-03 | 7.39E-03 | 5.50E-03 | 2.61E-01 | 8.55E-01 | 2.6 | 3.49 | 6.73E-03 | 12.7 | 2900 |
| 13 | 2.03 | 0.792 | 4.80E-03 | 7.40E-03 | 5.70E-03 | 2.37E-01 | 8.42E-01 | 2.6 | 3.52 | 7.70E-03 | 14.3 | 3600 |
| 14 | 1.79 | 0.793 | 4.70E-03 | 7.41E-03 | 5.70E-03 | 2.32E-01 | 8.25E-01 | 2.5 | 3.56 | 8.90E-03 | 16.1 | 5000 |
| 15 | 1.51 | 0.794 | 3.90E-03 | 7.34E-03 | 5.60E-03 | 2.36E-01 | 6.96E-01 | 2.5 | 3.58 | 1.04E-02 | 18.1 | 5500 |
| 16 | 1.21 | 0.795 | 1.90E-03 | 6.95E-03 | 5.10E-03 | 2.78E-01 | 3.73E-01 | 2.3 | 3.54 | 1.13E-02 | 19.7 | 4700 |

$M^{\rm Tot}_{\rm TDU}$ = **5.73E-02** $M_\odot$ $\tau_C$ = **1.44E+05 yr**

Table 5—Continued

| $n^a_{\rm TP}$ | $M^b_{\rm Tot}$ | $M^b_{\rm H}$ | $\Delta M^b_{\rm TDU}$ | $\Delta M^b_{\rm CZ}$ | $\Delta M^b_{\rm H}$ | $r$ | $\lambda$ | $\Delta t^c_{ip}$ | $T^d_{MAX}$ | $Z_{surf}$ | $C/O_{\rm surf}$ | $n_c$ |
|---|---|---|---|---|---|---|---|---|---|---|---|---|

[a]Pulse number (negative values correspond to TP not followed by TDU)

[b]$M_\odot$

[c]$10^4$ yr

[d]$10^8$ K

[(*)]$M_{\rm H}$ of this TP corresponds to $M^3_{\rm He}$ of Table 2

Table 6. Final enrichments of the three *s*-process peaks ([ls/Fe], [hs/Fe] and [Pb/Fe]) and *s*-process indexes ([hs/ls] and [Pb/hs]) for different masses at selected metallicities. The final surface composition of some key light elements, such as the final surface C/O, C/N and $^{12}C/^{13}C$ ratios are given.

| | $Z = 2.0 \times 10^{-2}$ | | | | $Z = 6.0 \times 10^{-3}$ | | | | $Z = 10^{-3}$ | | | |
|---|---|---|---|---|---|---|---|---|---|---|---|---|
| $M/M_\odot$ | 1.5 | 2.0 | 2.5 | 3.0 | 1.5 | 2.0 | 2.5 | 3.0 | 1.5 | 2.0 | 2.5 | 3.0 |
| [ls/Fe] | 0.40 | 0.93 | 1.12 | 1.02 | 0.89 | 1.36 | 1.44 | 1.03 | 1.26 | 1.35 | 1.21 | 1.03 |
| [hs/Fe] | 0.10 | 0.45 | 0.58 | 0.51 | 1.40 | 1.75 | 1.79 | 1.56 | 1.91 | 1.98 | 1.72 | 1.37 |
| [Pb/Fe] | 0.02 | 0.19 | 0.27 | 0.24 | 1.30 | 1.59 | 1.61 | 1.46 | 2.86 | 2.87 | 2.75 | 2.62 |
| [hs/ls] | -0.30 | -0.48 | -0.54 | -0.51 | 0.50 | 0.39 | 0.34 | 0.53 | 0.65 | 0.63 | 0.52 | 0.35 |
| [Pb/hs] | -0.09 | -0.26 | -0.31 | -0.27 | -0.10 | -0.16 | -0.18 | -0.10 | 0.95 | 0.89 | 1.03 | 1.25 |
| [C/Fe] | 0.16 | 0.42 | 0.56 | 0.48 | 0.82 | 1.17 | 1.23 | 0.94 | 2.11 | 2.18 | 2.08 | 1.78 |
| [N/Fe] | 0.32 | 0.35 | 0.39 | 0.42 | 0.36 | 0.40 | 0.44 | 0.47 | 0.63 | 0.56 | 0.50 | 0.49 |
| [O/Fe] | 0.00 | 0.00 | -0.02 | -0.03 | 0.02 | 0.03 | 0.01 | -0.01 | 0.35 | 0.32 | 0.25 | 0.18 |
| [F/Fe] | 0.12 | 0.40 | 0.59 | 0.50 | 0.55 | 1.06 | 1.18 | 0.81 | 2.08 | 2.22 | 1.99 | 1.51 |
| [Ne/Fe] | 0.05 | 0.17 | 0.27 | 0.22 | 0.20 | 0.56 | 0.67 | 0.32 | 1.42 | 1.60 | 1.38 | 0.80 |
| [Na/Fe] | 0.05 | 0.16 | 0.28 | 0.21 | 0.11 | 0.36 | 0.46 | 0.23 | 1.13 | 1.28 | 1.01 | 0.61 |
| [Mg/Fe] | 0.00 | 0.00 | 0.01 | 0.01 | 0.01 | 0.07 | 0.11 | 0.05 | 0.43 | 0.72 | 0.73 | 0.42 |
| $(C/O)_{surf}$ | 0.71 | 1.33 | 1.89 | 1.59 | 3.15 | 6.92 | 8.25 | 4.55 | 29.0 | 35.9 | 33.9 | 19.7 |
| $(C/N)_{surf}$ | 2.48 | 4.22 | 5.34 | 4.08 | 10.5 | 21.3 | 22.1 | 10.9 | 111 | 151 | 157 | 70.7 |

Table 6—Continued

| | $Z = 2.0 \times 10^{-2}$ | | | | $Z = 6.0 \times 10^{-3}$ | | | | $Z = 10^{-3}$ | | | |
|---|---|---|---|---|---|---|---|---|---|---|---|---|
| $(^{12}C/^{13}C)_{surf}$ | 50 | 98 | 141 | 115 | 239 | 575 | 693 | 349 | 3600 | 5193 | 4302 | 196 |

Table 7. Yields (in $M_\odot$) of selected isotopes for $Z = 2.0 \times 10^{-2}$.

| Isotope | $M$=1.5 $M_\odot$ | $M$=2.0 $M_\odot$ | $M$=2.5 $M_\odot$ | $M$=3.0 $M_\odot$ |
|---|---|---|---|---|
| $^{1}$H | -2.25E-02 | -6.08E-02 | -7.76E-02 | -9.01E-02 |
| $^{4}$He | 2.04E-02 | 4.79E-02 | 6.06E-02 | 7.36E-02 |
| $^{12}$C | 4.61E-04 | 8.22E-03 | 1.20E-02 | 1.10E-02 |
| $^{13}$C | 5.38E-05 | 1.12E-04 | 9.81E-05 | 1.27E-04 |
| $^{14}$N | 9.86E-04 | 2.66E-03 | 2.91E-03 | 4.16E-03 |
| $^{15}$N | -1.40E-06 | -4.19E-06 | -4.18E-06 | -5.53E-06 |
| $^{16}$O | -1.88E-05 | -1.51E-04 | -6.59E-04 | -1.21E-03 |
| $^{17}$O | 4.97E-06 | 5.17E-05 | 7.03E-05 | 7.12E-05 |
| $^{18}$O | -3.64E-06 | -1.14E-05 | -1.17E-05 | -1.54E-05 |
| $^{19}$F | 1.03E-07 | 1.45E-06 | 2.40E-06 | 2.25E-06 |
| $^{20}$Ne | -8.64E-07 | -4.24E-06 | -1.70E-06 | -2.85E-06 |
| $^{21}$Ne | 2.58E-09 | 8.55E-08 | 3.61E-07 | 7.49E-07 |
| $^{22}$Ne | 1.21E-04 | 1.34E-03 | 2.21E-03 | 2.03E-03 |
| $^{23}$Na | 4.58E-06 | 3.95E-05 | 6.94E-05 | 6.67E-05 |
| $^{24}$Mg | 9.25E-07 | 1.43E-05 | 2.96E-05 | 3.03E-05 |
| $^{25}$Mg | -4.76E-07 | -3.63E-07 | 5.18E-07 | 3.56E-06 |
| $^{26}$Mg | 4.66E-07 | 5.91E-06 | 1.05E-05 | 1.40E-05 |
| $^{26}$Al | 1.76E-07 | 7.92E-07 | 7.87E-07 | 7.27E-07 |
| $^{36}$Cl | 2.96E-10 | 3.07E-09 | 3.28E-09 | 4.78E-09 |
| $^{41}$Ca | 5.57E-10 | 9.09E-09 | 9.70E-09 | 1.39E-08 |
| $^{60}$Fe | 6.74E-09 | 5.26E-08 | 8.23E-08 | 4.33E-08 |

Table 7—Continued

| Isotope | $M$=1.5 $M_\odot$ | $M$=2.0 $M_\odot$ | $M$=2.5 $M_\odot$ | $M$=3.0 $M_\odot$ |
|---|---|---|---|---|
| $^{89}$Y | 1.29E-08 | 1.90E-07 | 2.84E-07 | 2.81E-07 |
| $^{107}$Pd | 1.17E-10 | 1.84E-09 | 2.39E-09 | 2.46E-09 |
| $^{139}$La | 4.67E-10 | 1.01E-08 | 1.46E-08 | 1.45E-08 |
| $^{205}$Pb | 3.75E-12 | 9.44E-11 | 1.39E-10 | 1.40E-10 |
| $^{208}$Pb | 1.42E-10 | 7.23E-09 | 1.07E-08 | 1.21E-08 |

Table 8. Yields (in $M_\odot$) of selected isotopes for $Z = 6.0 \times 10^{-3}$.

| Isotope | $M$=1.5 $M_\odot$ | $M$=2.0 $M_\odot$ | $M$=2.5 $M_\odot$ | $M$=3.0 $M_\odot$ |
|---|---|---|---|---|
| $^{1}$H | -2.79E-02 | -6.59E-02 | -1.10E-01 | -7.06E-02 |
| $^{4}$He | 2.41E-02 | 5.09E-02 | 8.50E-02 | 5.77E-02 |
| $^{12}$C | 2.85E-03 | 1.26E-02 | 2.09E-02 | 1.07E-02 |
| $^{13}$C | 1.49E-05 | 2.01E-05 | 2.64E-05 | 3.46E-05 |
| $^{14}$N | 3.34E-04 | 5.98E-04 | 1.03E-03 | 1.41E-03 |
| $^{15}$N | -4.55E-07 | -9.14E-07 | -1.37E-06 | -1.71E-06 |
| $^{16}$O | 6.01E-05 | 1.69E-04 | 6.84E-05 | -2.35E-04 |
| $^{17}$O | 3.61E-06 | 2.31E-05 | 2.58E-05 | 2.62E-05 |
| $^{18}$O | -1.32E-06 | -2.75E-06 | -4.21E-06 | -5.05E-06 |
| $^{19}$F | 2.39E-07 | 1.59E-06 | 3.05E-06 | 1.43E-06 |
| $^{20}$Ne | -1.16E-06 | 1.28E-06 | 8.31E-06 | -3.67E-06 |
| $^{21}$Ne | 2.96E-08 | 2.54E-07 | 7.32E-07 | 5.70E-07 |
| $^{22}$Ne | 1.67E-04 | 1.20E-03 | 2.33E-03 | 7.65E-04 |
| $^{23}$Na | 3.06E-06 | 1.75E-05 | 3.60E-05 | 2.02E-05 |
| $^{24}$Mg | 2.99E-06 | 2.37E-05 | 5.32E-05 | 9.17E-06 |
| $^{25}$Mg | 1.85E-07 | 6.12E-06 | 1.58E-05 | 1.28E-05 |
| $^{26}$Mg | 5.28E-07 | 7.02E-06 | 1.75E-05 | 1.79E-05 |
| $^{26}$Al | 8.57E-08 | 1.23E-07 | 1.35E-07 | 2.31E-07 |
| $^{36}$Cl | 2.59E-10 | 1.41E-09 | 2.17E-09 | 2.59E-09 |
| $^{41}$Ca | 6.65E-10 | 3.36E-09 | 4.96E-09 | 6.24E-09 |
| $^{60}$Fe | 1.69E-08 | 5.00E-08 | 2.28E-07 | 4.31E-08 |

Table 8—Continued

| Isotope | $M$=1.5 $M_\odot$ | $M$=2.0 $M_\odot$ | $M$=2.5 $M_\odot$ | $M$=3.0 $M_\odot$ |
|---|---|---|---|---|
| $^{89}$Y | 1.67E-08 | 1.00E-07 | 1.74E-07 | 7.13E-08 |
| $^{107}$Pd | 3.16E-10 | 1.68E-09 | 2.88E-09 | 1.26E-09 |
| $^{139}$La | 1.17E-08 | 5.38E-08 | 8.62E-08 | 5.11E-08 |
| $^{205}$Pb | 2.96E-10 | 1.04E-09 | 1.45E-09 | 7.54E-10 |
| $^{208}$Pb | 3.37E-08 | 1.50E-07 | 2.33E-07 | 1.69E-07 |

Table 9. Yields (in $M_\odot$) of selected isotopes for $Z = 10^{-3}$.

| Isotope | $M$=1.5 $M_\odot$ | $M$=2.0 $M_\odot$ | $M$=2.5 $M_\odot$ | $M$=3.0 $M_\odot$ |
|---|---|---|---|---|
| $^{1}$H | -6.11E-02 | -1.15E-01 | -1.05E-01 | -6.03E-02 |
| $^{4}$He | 4.82E-02 | 8.85E-02 | 8.00E-02 | 4.57E-02 |
| $^{12}$C | 1.11E-02 | 2.23E-02 | 2.20E-02 | 1.30E-02 |
| $^{13}$C | 2.86E-06 | 3.63E-06 | 4.75E-06 | 9.73E-05 |
| $^{14}$N | 9.81E-05 | 1.52E-04 | 1.83E-04 | 2.31E-04 |
| $^{15}$N | -7.51E-08 | -1.65E-07 | -2.44E-07 | -2.84E-07 |
| $^{16}$O | 2.91E-04 | 4.47E-04 | 3.89E-04 | 3.05E-04 |
| $^{17}$O | 1.71E-06 | 7.09E-06 | 1.07E-05 | 5.29E-06 |
| $^{18}$O | -2.67E-07 | -5.07E-07 | -7.67E-07 | -8.26E-07 |
| $^{19}$F | 1.71E-06 | 3.97E-06 | 2.97E-06 | 1.60E-06 |
| $^{20}$Ne | 6.35E-06 | 2.80E-05 | 1.57E-05 | 3.05E-06 |
| $^{21}$Ne | 2.45E-07 | 1.00E-06 | 1.22E-06 | 4.36E-07 |
| $^{22}$Ne | 1.05E-03 | 2.69E-03 | 1.87E-03 | 5.91E-04 |
| $^{23}$Na | 1.33E-05 | 3.25E-05 | 2.24E-05 | 1.03E-05 |
| $^{24}$Mg | 2.19E-05 | 7.33E-05 | 2.73E-05 | 3.35E-06 |
| $^{25}$Mg | 6.95E-06 | 4.36E-05 | 6.29E-05 | 3.21E-05 |
| $^{26}$Mg | 6.62E-06 | 3.14E-05 | 9.37E-05 | 4.81E-05 |
| $^{26}$Al | 2.57E-08 | 5.40E-08 | 6.74E-08 | 2.86E-08 |
| $^{36}$Cl | 1.91E-10 | 4.34E-10 | 5.05E-10 | 4.54E-10 |
| $^{41}$Ca | 3.77E-10 | 8.58E-10 | 9.62E-10 | 6.83E-10 |
| $^{60}$Fe | 2.33E-08 | 1.27E-07 | 5.40E-07 | 5.93E-07 |

Table 9—Continued

| Isotope | $M$=1.5 $M_\odot$ | $M$=2.0 $M_\odot$ | $M$=2.5 $M_\odot$ | $M$=3.0 $M_\odot$ |
|---|---|---|---|---|
| $^{89}$Y | 7.08E-09 | 1.55E-08 | 1.48E-08 | 1.00E-08 |
| $^{107}$Pd | 1.11E-10 | 1.99E-10 | 1.66E-10 | 1.25E-10 |
| $^{139}$La | 5.50E-09 | 1.08E-08 | 7.89E-09 | 4.39E-09 |
| $^{205}$Pb | 2.36E-10 | 3.95E-10 | 1.98E-10 | 1.42E-10 |
| $^{208}$Pb | 4.49E-07 | 8.48E-07 | 8.66E-07 | 7.95E-07 |

Table 10. Surface *s*-process branched number isotopic ratios for different initial masses at selected metallicities. The tabulated ratios relate to the branchings occurring at $^{85}$Kr, $^{86}$Rb, $^{95}$Zr, $^{133}$Xe and $^{141}$Ce, respectively. Solar ratios are also reported.

| Isot. Ratio | $\odot$ | $Z = 2.0 \times 10^{-2}$ | | | | $Z = 6.0 \times 10^{-3}$ | | | | $Z = 10^{-3}$ | | | |
|---|---|---|---|---|---|---|---|---|---|---|---|---|---|
| $M/M_{\odot}$ | — | 1.5 | 2.0 | 2.5 | 3.0 | 1.5 | 2.0 | 2.5 | 3.0 | 1.5 | 2.0 | 2.5 | 3.0 |
| $^{86}$Kr/$^{84}$Kr | 0.30 | 0.27 | 0.21 | 0.18 | 0.20 | 0.37 | 0.36 | 0.43 | 0.54 | 0.46 | 0.66 | 0.91 | 1.09 |
| $^{87}$Rb/$^{85}$Rb | 0.38 | 0.38 | 0.30 | 0.27 | 0.30 | 0.53 | 0.57 | 0.85 | 0.89 | 0.81 | 1.29 | 1.61 | 1.79 |
| $^{96}$Zr/$^{94}$Zr | 0.16 | 0.08 | 0.03 | 0.02 | 0.03 | 0.10 | 0.07 | 0.13 | 0.17 | 0.19 | 0.43 | 0.84 | 1.18 |
| $^{134}$Xe/$^{132}$Xe | 0.36 | 0.29 | 0.14 | 0.11 | 0.13 | 0.08 | 0.06 | 0.09 | 0.18 | 0.15 | 0.46 | 0.90 | 0.79 |
| $^{142}$Ce/$^{140}$Ce | 0.13 | 0.10 | 0.04 | 0.03 | 0.03 | 0.01 | 0.01 | 0.02 | 0.05 | 0.04 | 0.14 | 0.28 | 0.30 |

Table 11. Selected physical and chemical quantities for a model with $M$=2 $M_{\odot}$ and $Z = 6 \times 10^{-3}$ (FRANEC Standard Model, FSM). Normalized percentage variations as a function of different input parameters are reported. Percentage values are defined as the difference between Test cases and Standard Case, normalized to the Standard one: (Test-FSM)/SM*100.

| Case | $M_{\rm H}^{a}$ | $\overline{\rm M}_{\rm bol}^{C}$ | $\tau_C$ | Yield$^a$($^{12}$C) | Yield$^a$($^{89}$Y) | Yield$^a$($^{139}$La) | Yield$^a$($^{208}$Pb) | [hs/ls] |
|---|---|---|---|---|---|---|---|---|
| FSM | 0.644 | -4.98 | 1.38E+06 | 1.26E-02 | 1.00E-07 | 5.38E-08 | 1.50E-07 | 0.39 |
| $\alpha_1$ | +0.5% | -13% | +18% | +39 % | +54% | +38% | +31% | -15% |
| $\alpha_2$ | -1.6% | +17% | -22% | -36% | -47% | -40% | -42% | +13% |
| $\dot{M}_1^{\rm AGB}$ | -3.1% | +20% | -28% | -30% | -29% | -24% | -21% | 7% |
| $\dot{M}_2^{\rm AGB}$ | +2.1% | -17% | +21% | 32% | 30% | 24% | 17% | -5% |
| $\beta_1$ | -1.2% | +2% | 6% | 16% | -66% | -79% | -93% | -53% |
| $\beta_2$ | +1.0% | -9% | -16% | -19% | -84% | -87% | -93% | -36% |

$^a$ In $M_{\odot}$ units

Table 12. Initial abundances and net stellar yields relative to a 3 $M_{\odot}$ model with Z=0.02 taken from our database (FRUITY) and from Karakas 2010 (K10). Percentage differences are also shown.

| Isotope | Yields[a] (FRUITY) | Yields[a] (K10) | [(FRUITY/K10)-1]*100 |
|---|---|---|---|
| $^{1}$H | -9.01E-02 | -6.95E-02 | -29 |
| $^{4}$He | 7.36E-02 | 5.13E-02 | +43 |
| $^{12}$C | 1.10E-02 | 1.20E-02 | -9 |
| $^{13}$C | 1.27E-04 | 1.10E-04 | +16 |
| $^{14}$N | 4.16E-03 | 3.09E-03 | +35 |
| $^{15}$N | -5.53E-06 | -5.03E-06 | -10 |
| $^{16}$O | -1.21E-03 | -9.02E-04 | -34 |
| $^{17}$O | 7.12E-05 | 4.68E-05 | +52 |
| $^{18}$O | -1.54E-05 | -1.37E-05 | -12 |
| $^{19}$F | 2.25E-06 | 4.13E-06 | -46 |
| $^{20}$Ne | -2.85E-06 | 1.01E-05 | -128 |
| $^{21}$Ne | 7.49E-07 | 1.05E-06 | -29 |
| $^{22}$Ne | 2.03E-03 | 3.45E-03 | -41 |
| $^{23}$Na | 6.67E-05 | 9.28E-05 | -28 |
| $^{24}$Mg | 3.03E-05 | 1.36E-05 | +123 |
| $^{25}$Mg | 3.56E-06 | 2.17E-05 | -84 |
| $^{26}$Mg | 1.40E-05 | 2.58E-05 | -46 |
| $^{27}$Al | 2.58E-06 | 2.58E-06 | -19 |
| $^{28}$Si | -2.78E-07 | -2.78E-07 | -212 |
| $^{29}$Si | 2.96E-07 | 2.96E-07 | -19 |
| $^{30}$Si | 1.28E-06 | 1.28E-06 | +10 |

Table 12—Continued

| Isotope | Yields[a] (FRUITY) | Yields[a] (K10) | [(FRUITY/K10)-1]*100 |
|---|---|---|---|
| $^{31}$P | 8.06E-07 | 8.06E-07 | -50 |

[a] In $M_{\odot}$ units